University of Leeds

School of Mechanical Engineering

Institute of Medical and Biological Engineering

Doctorate Training Centre

Experimental and Computational simulation of strain in medium sized arteries at macro- and micro-level.

Eirini Tsagkaraki

June 2017

Submitted in accordance with the requirements for the degree of Doctor of Philosophy

Supervisors:

Prof J Fisher

Prof E Ingham

Dr S P Wilshaw

Prof Z Jin

The candidate confirms that the work submitted is his/her own and that appropriate credit has been given where reference has been made to the work of others.

Table of Contents

Acknowledgements

I would like first of all to thank my supervisors Prof. J. Fisher, Prof. E. Ingham, Prof. Z. Jing and Dr S.P. Wilshaw for their guidance, support and understanding.

This work would have never been carried out without the support of my family. First and foremost I would like to thank my husband Sotiris for the inspiration, guidance, patience, as well as for the encouragement and funding support. I love you always and this work is dedicated to you.

Additionally, I would like to thank my parents, my in-laws, and my aunt Katerina for taking the massive load of baby sitting and housekeeping for me. And of course, their own families for the support and understanding.

Furthermore, I would like to thank my friends Isabella, Margarita and Kostantina for the support and for keeping my back no matter what. You are the greatest friends ever!! Also my friend Menios for all these long chats and depression dealing.

I would also like to thank all the technicians in the lab, Amisha, Phil, Irvin for everything. As well as all my friends in the lab, Iraklis, Vassilis, Lucrezia and Jake for their time, help, patience and great coffee times.

Many thanks to my DTC mates Niki, Andy, Will, Jihad and Rob for being my brave boys during the first year. I'm very proud of all of you guys! Thanks to my friend Salah for sharing a massive empty room and for the company and chats during long afternoons and coffee breaks.

Moreover I would like to thank my friends in Germany, Zoi and Alexis for all the positive energy and kids activities. Also Eirini for making the impossible possible in this country!

After so many years I have met so many people that contributed on this thesis and I would like to thank them all for everything.

I would also like to express my apologies to my son, Anastasis, for every time he was missing me. Thank you for being in my life!

This project was funded by Doctorate Training Centre in Tissue Engineering and Regenerative Medicine between Leeds, Sheffied and York Universities.

Abbreviations

AF – Annulus Fibrosus

AFM – Atomic Force Mircroscopy

ALE – Arbitrary Lagrangian Eulerian

CFD – Computational Fluid Dynamics

CMU – Cell-matrix Units

CT – Computerised Tomography

EC – Endothelial cell

ECM – Extracellular Matrix

ePTFE – Expanded Polytetrafluoroethylene

FEA – Finite Element Analysis

FEM – Finite Element Method

FG – Fibrin Glue

FGF – Fibroblast Growth Factor

FN – Fibronectin

FSI – Fluid Structure Interaction

IVD – Intervertebral Disc

MRI – Magnetic Resonance Imaging

MSC – Mesenchymal Stem cell

PBS – Phosphate Buffer Saline

PCM – Pericellular Matrix

PTFE – Polytetrafluoroethylene

RBC – Red Blood cell

SMC – Smooth Muscle cell

TE – Tissue Engineering

TEBV – Tissue Engineered Blood Vessel

WBC – White Blood cell

WSS – Wall Shear Stress

Glossary of Terms

A	Cross sectional area
D,d	Diameter
E	Young's modulus
F	Force
P	Pressure
t	Time
u	Velocity
ε	Strain
μ	Viscosity
ν	Poisson's ratio
ρ	Fluid Density
σ	Stress

List of Figures

List of Tables

Abstract

Cardiovascular disease remains the leading cause of mortality in Western world. Current treatments for vascular disease include vascular grafting and stenting. Owing to the limitations of current treatments, over the past few years a significant research effort has been directed towards the development of tissue engineered blood vessels (TEBV). However, a TEBV that matches the biological and biomechanical functionality of natural blood vessels has yet to be developed. One of the strategies employed in the development of TEBVs involves the use of decellularised or synthetic scaffolds, which are seeded with the patient's own cells and physically conditioned in bioreactors, with a view to developing blood-vessel-equivalent functionality prior to implantation. Along this line, the physical conditioning in bioreactors needs to replicate the *in vivo* haemodynamic stimulation, in order to guide normal cellular function and appropriate graft remodelling and regeneration. However, the *in vitro* set up, with the cells seeded on to a decellularised or synthetic scaffold and subjected to pulsatile flow in a bioreactor, does not represent a physiological scenario. Even if the bioreactor is able to simulate physiological haemodynamic conditions at the macroscale, the stimulus that would be transferred to the microscale and sensed by the cells to regulate their function is likely to be different from the micro-stimulus sensed by the cells *in vivo* in a native blood vessel. Therefore, in order to appropriately guide cellular function *in vitro* it would be necessary to assess the level of micro-stimulus sensed by the native cells in the native blood vessel *in vivo*, with a view to simulating this micro-stimulus in artificial bioreactor environments for conditioning the cells that are seeded onto scaffolds with non-native histoarhitectures. However, this micro-stimulus that vascular cells are exposed to *in vivo* cannot be assessed experimentally. The advances in computing and software resources have enabled the use of computational modelling for conducting such assessments. The aim of this project was to develop computational models for assessing the stress and strain fields on the vascular tissue and cells at the macro- and micro-scales, which will assist the bioreactor conditioning towards the development of tissue engineered vascular grafts. The 3D macro-scale simulations involved fluid-structure interaction (FSI) analysis with main focus on the strain on the vascular wall, while the 2D micro-scale simulation involved finite

element analysis (FEA), focused on the local strain variation. All simulations were based on relatively physiological structures after experimental assessment. The simulations were also compared against experimental findings for strain. Macro strain resulted in approximately 11% for FSI against 19% for experimental pressure test. However, the limitations of the experimental procedure overestimated the performed dilation. Moreover, the 2D FEA simulations performed under different material properties, as an attempt to approach more physiological conditions, and under uniaxial strain only. The variation in material properties indicated inhomogeneicity, as expected, and also seemed to replicate the local strain spread when compared to experimental findings. However, further investigation is needed, which will involve the development of 3D FEA models, more physiological material properties and biaxial stretching. Under these circumstances, more information may be extracted and eventually applied to the bioreactor conditioning. Nevertheless, the novel methodology developed in this project for the study of the strain at the micro-level allows the further investigation on the tissue micro-environment.

Chapter 1. Introduction

In spite of remarkable advances in medical science, the human body is still subject to malfunction. Organ or tissue dysfunction due to aging, accident, or congenital conditions is the principal cause of death worldwide. In the western societies, cardiovascular disease is the leading cause of mortality and one of the most prominent in terms of healthcare spending. Vascular disease, such as atherosclerosis, aneurysms, diabetes, and high blood pressure, affect the normal function of the body by interrupting the delivery of oxygen and other nutrients to the rest of organs and tissues, leading to strokes, heart attacks and other organ failure [Ratcliffe, 2000]. Additionally, chronic venous dysfunction, as well as lower extremity chronic deep venous insufficiency affects an estimated 3% of the general population in the Western World, while it remains a major health problem worldwide [Teebken *et al.* 2003, Bergan *et al*, 2006].

Current surgical interventions for the treatment of vascular disease include vascular grafting and stenting. Grafting involves the use of the patient's own (autologous) tissue to replace the defected vessels. However, in 10-40% of patients, there is no suitable autologous tissue available, mainly due to the frequent reoperations in these vascular conditions, as well as due to other trauma or underlying disease. Under such circumstances, surgeons employ alternative conduits for the replacement of diseased vessels, such as prosthetic (synthetic) grafts. Synthetic grafts such as polyethylene terephthalate (Dacron®) and expanded polytetrafluoroethylene (ePTFE) perform well in large diameter vessels (>6mm), where the flow is high, while in smaller arteries (diameter <6mm) have been proved unsuccessful. The failure of small sized grafts has been associated to intimal hyperplasia and thrombosis[Pappas et al 1998], as well as to the increased turbulence and subsequent damage to the blood constituents and reconstituted endothelium on the graft wall, leading to poor patency rates *in vivo* [Tiwari *et al,* 2002]. Moreover, the use of vascular homografts and chemically-treated xenografts, as alternatives to autologous conduits for grafting, has resulted to aneurismal degeneration, calcification and rupture [Dale&Lewis 1976, Umpleby et al. 1984, Dardik et al. 1988, 2002].

Owning to the limitations of the conventional treatments and therapies, workers in relative fields have sought alternative solutions, in order to improve and extend the lives of patients. One of these alternative approaches is tissue engineering (TE). Tissue engineering offers an attractive alternative for tissue reconstructions, involving the development of biological or hybrid substitutes for implantation into the body with a view to fostering remodelling and regeneration of diseased tissue. First generation of vascular tissue-engineered constructs involved the use of synthetic or natural-decellularised tissue scaffolds, which would allow the migration of the endogenous cells, and subsequently regenerate in the patient. However, this approach has been associated with inappropriate implant properties *in vivo*, as well as with variability of the patient response in terms of recellularisation and [Serruys et al. 2006, Stone et al. 2009].

Second generation tissue-engineered grafts employ scaffolds (decellularised tissue or synthetic), which are seeded *in vitro* with the patient's own cells and physically conditioned in bioreactors, in order to produce functional grafts, prior to implantation [Niklason et al. 1999]. The main advantage of this approach is that it can improve the localisation of cell delivery and promote graft fixation and survival. Therefore, there is a great interest in comprehending the mechanisms under which the *in vitro* recellularisation would generate desirable results in terms of scaffold remodelling and graft survival *in vivo*. To this view, it is necessary to understand the process by which the cells transduce mechanical forces into biochemical signals. This process is called mechanotransduction and, together with biochemical cues, is responsible for the regulation of cell function.

Previous studies [Chien 2007] have demonstrated that mechanical forces applied to endothelial cells (ECs) due to blood flow, play a significant role in the interaction of cells with their environment, and they are responsible for several cellular pathways that regulate cell and tissue function. Nevertheless, the most abundant cells in vascular tissue, and especially in vessels with a diameter <6mm, are smooth muscle cells (SMCs). The ECs form the inner layer of the vessel and are predominantly exposed to blood-flow-induced cyclic shear stresses, whereas the SMCs reside in the middle vascular wall layer and are predominantly subjected to cyclic circumferential and axial strain, as a result of the vessel dilation/elongation under the pulsatile blood pressure. Previous reports [Kim *et al.*, 1999] have

demonstrated that when SMCs were subjected to mechanical loading, the production of collagen and elastin increased, compared to the case that no loading was applied, demonstrating the direct link between mechanical loading and extracellular matrix (ECM) protein synthesis. However, the amount of mechanical loading experienced by SMCs *in situ* is largely unknown. This is also true for the amount of mechanical loading that is necessary to be applied to a tissue-engineered vascular construct in order to elicit appropriate cell function and physiologically-relevant tissue remodelling and regeneration.

In order for tissue-engineered substitutes to provide effective restoration of function, they need to match closely the biological and biomechanical properties of the tissue/organ they replace. The development of such substitutes demands a multidisciplinary approach, incorporating biology, engineering, materials science and medicine, as well as the consideration of a wide range of relevant issues, including the specific function of the organ/tissue repaired or replaced and the degree of restoration of function required. To date, traditional *in vitro* or *in vivo* experimental methods do not allow the accurate assessment of the blood stresses and their effect on tissues and cells. Therefore, there is a considerable drive to develop alternative methods for providing further quantitative and qualitative information on the mechanical environment of cells and tissues that can be used to guide cell function and tissue regeneration in tissue-engineered vascular conduits.

Recent advances in high performance computing has made possible the development of complex numerical simulations that have the potential to revolutionise tissue-engineered construct development by providing relatively inexpensive testing platforms able to assess the mechanical environment of tissues and cells and predict the development of these constructs in bioreactors. Vascular computational modelling covers a wide area of research, from the macro- to the micro-scale. At the macro-scale, the progress of the medical imaging has provided more realistic geometries as input data for the computational models. Additionally, the advances in mathematics and computing have allowed the investigation of the interaction between the blood and the tissue using the Fluid-Structure Interaction method (FSI). By coupling the fluid (blood) and the elastic structure (vascular wall), this method enables the prediction of the wall deformation due to pulse variation, in response to change in pressure [Morris et al. 2015]. Such information can then be

transferred from the macro- to the micro-scale, to investigate its effect at the cellular level.

The aim of this research project was to develop computational models with a view to investigating the effect of the macroscale stress/strain, generated by the pulsatile blood flow, to the microscale stress/strain experienced by the cells and the ECM in the wall of porcine femoral arteries. The ultimate purpose of the present research is to use the results, in order to optimise the conditioning of tissue-engineered arteries in the specially designed bioreactor to achieve a more physiological regeneration. Additionally, the computational models may be further used for the study of different scaffolds architecture, which will provide information on the strain translation in different scales. This thesis comprises 7 chapters that describe the work conducted during this PhD project. Chapter 2 is focused on the literature review and the state of the art in the computational modelling and tissue engineering of blood vessels. Chapter 2 also describes experimental and computational approaches for investigating cellular mechanotransduction. Chapter 3 describes the experimental work that was carried out, in order to obtain the geometrical and the mechanical properties of the femoral arteries that were subsequently used to develop the 3D computational FSI models. The development of the macroscale FSI computational model is described in Chapter 4, alongside the validation of the macroscale FSI computational results against experimental findings and mathematical verification. Chapter 5 is focused on the development of the 2D microscale computational modelling of the arterial wall. Chapter 6 describes the experimental process that was carried out to provide data for validating the microscale computational models. Finally, Chapter 7 discusses the findings of the study, together with its conclusions and future work.

Chapter 2. Literature Review

2.1 Physiology of the blood vessels

While the heart's pumping action is responsible for keeping blood in motion, it is the blood vessels that carry the blood around the body. Blood vessels of the circulatory system are divided into two main categories: the *arteries*, which carry the blood from the heart to the organs and tissues, and the *veins*, which carry the deoxygenated blood back to the heart (Figure 2.14). This section is focused on the structure and mechanical properties of the arteries.

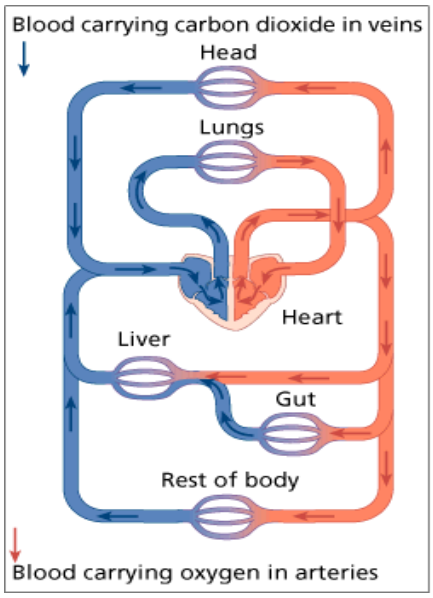

Figure 2.14: Schematic of blood circulation [Cancer research UK, 2008]. Schematic illustrates the direction of blood through the vascular system.

2.1.1 Structure of arteries

As arteries distance from the heart, they branch repeatedly, and these branches decrease in size as they approach the tissues (Figure 2.15.2). The branched system of arteries, as well as that of the veins, vary in size, mechanical properties, biochemical and cellular content, as well as in ultra-structural organisation, depending on their location. Large and medium-sized vessel walls are formed by three different layers. The inner (*tunica interna*, or *tunica intima*), the middle (*tunica media*) and the outer (*tunica externa*, or *tunica adventitia*) (Figure

2.16). As the vessels decrease in size, the external layers disappear, leaving the smallest, the capillaries, with a single layer, the endothelium.

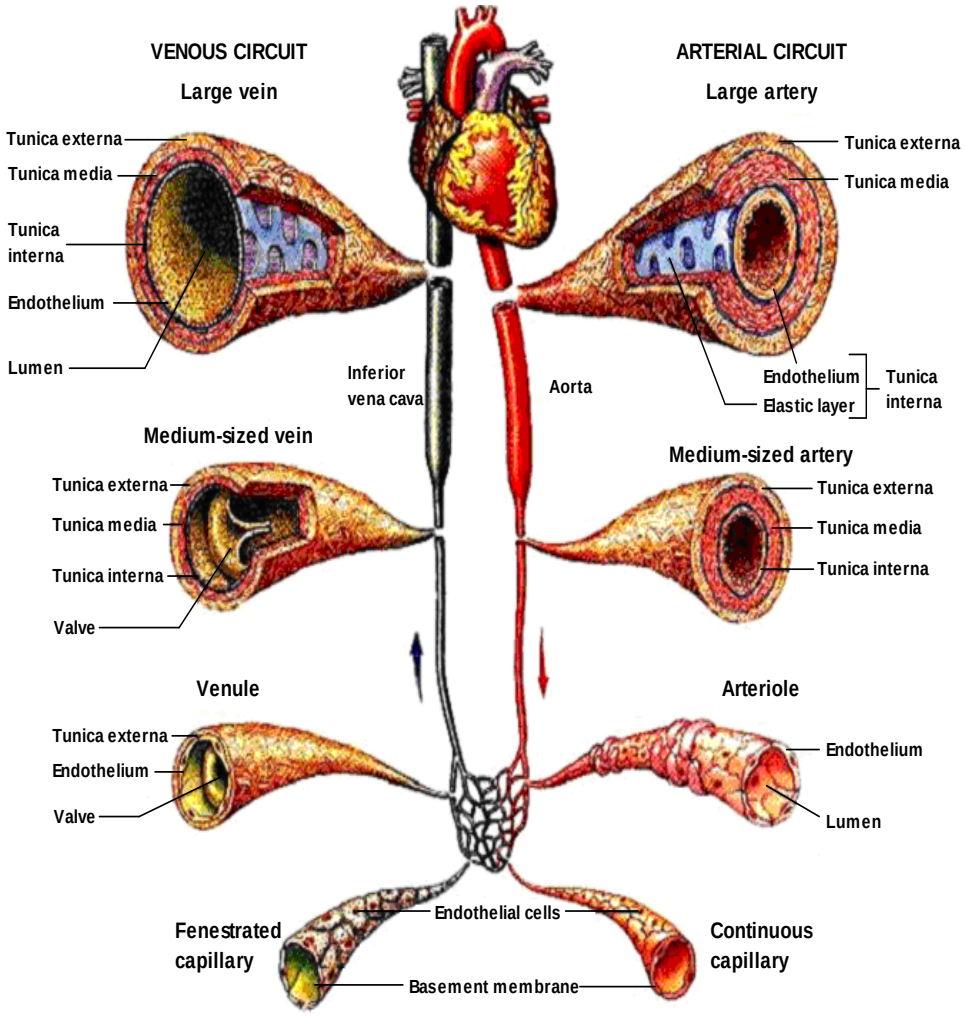

Figure 2.15: Histological structure of the vascular system [Bozkurt, 2008]. The schematic describes the meso-structure of the blood vessels. Vessel size is inversely proportional to their distance from the heart.

The tunica interna (endothelium) is the internal layer of any blood vessel. This layer contains the endothelial cell lining and an underlying layer of connective tissue with abundant elastic fibres (the *basal lamina* or *elastica interna*). However, in the large elastic arteries, such as the aorta, there is an additional *sub-endothelial* layer. The structure of this layer varies according to the age of the individual, since it develops gradually. In young ages it is very thin and composed of connective tissue fibres. As the individual grows older, this layer becomes gradually thicker, cellular and denser. Several cell types have been identified within the sub-endothelial layer,

with SMCs being the dominant type, followed by fibroblasts, macrophages, and a small numbers of mesenchymal stem cells (MSCs) [Rhoden 1980].

The endothelial lining is a single-cell layer, which is formed by endothelial cells (EC) and constitutes the inner lining of the entire vasculature. Endothelial cells seem to arrive from a hematopoietic precursor, the haemangioblast [Sumpio *et al.* 2002]. They are polygonal, flattened (0.2-0.5 μm thick) and elongated parallel to the blood vessel axis (along the direction of blood flow) [Rhoden 1980, Levick 2003]. Junctional complexes are found between the ECs. These junctions serve for communication and transport between the ECs and between the ECs and the other vascular layers. Since the endothelial layer acts as a barrier, the ECs' properties allow their interaction with the underlying smooth muscle layer, as well as with the blood constituents. The ECs prevent thrombogeneicity at the blood-tissue interface, by regulating several processes, such as thrombolysis and vasodilatation. Several vasoactive substances and mediators (such as nitric oxide), which are released by ECs in response to chemical stimuli from the surrounding environment, are responsible for these processes [Sumpio *et al.* 2002]. The ECs have also been reported to play a significant role in angiogenesis and vasculogenesis during embryogenesis. It seems that endothelial growth factors and cell-specific receptors are necessary during morphogenesis for the differentiation of the capillary network [Sumpio *et al.* 2002, Martini 1989]. Regulation of immune and inflammatory responses is also a function of the endothelial cells, owing to their ability to control the interactions between monocytes and lymphocytes with the vessel walls. These properties of the endothelium assist homeostasis and maintain the normal function of the circulatory system. Therefore, any malfunction of the endothelium, caused by injury or any other abnormality, may contribute to the development of vascular and heart disease, such as hypertension, atherosclerosis, and congestive heart failure. Unfortunately, many of the ECs' pathways remain unknown, and their dysfunction cannot always be prevented.

The middle layer of the vascular wall is the *tunica media*. This layer comprises of bundles of collagenous fibrils, elastic fibrils and sheets, and the only type of cell present is smooth muscle cell (SMC) (Figure 2.3). The extracellular matrix (ECM) proteins of the tunica media supply the necessary mechanical strength to the vessels, which varies according to their position. The spindle-shaped SMCs have a

single nucleus, which is located in the thickest part of the cell. The size of SMCs varies between 20-50 μm, and their thickness between 5-10 μm [Bader 1963]. The SMCs form two types of smooth muscles (SM): the tension muscles and the ring muscles. The tension muscles are connected to elastic fibres, and by contracting, they raise the tension on the elastic tissue to control the blood pressure. These are only found in elastic arteries and in large muscular arteries, in addition to ring muscles. There are only ring muscles in all other arteries, which are connected to each other. These muscles form helical layers along the axial direction [Levick 2010]. The number of the layers formed by the ring muscles ranges between 25-35 in large and medium-sized vessels, 3-6 in smaller arteries, and only up to 2 in the arterioles [Rhoden 1980]. In large elastic arteries fenestrated elastic laminae are found between the SMCs, but they decrease in size, and eventually disappear as they approach the smaller arteries. These elastic laminae are concentrically arranged, spaced equidistantly, and interconnected by networks of elastic fibrils. The elastic components and the SMs of the middle layer are held together by a network of collagen fibrils, and are all embedded in a viscous mucopolysaccharide ground substance [Rhoden 1980].

The *tunica adventitia* (connective tissue) forms the outer layer of the vascular wall. The tunica adventitia comprises of an elastic membrane, the *elastica externa*, and a connective tissue (Figure 3). The elastica externa serves to separate the media layer from the connective tissue, while the connective tissue serves to connect the vessels to the surrounding tissues [Rhoden 1980]. Sympathetic fibre terminals are found in the adventitial layer, which serve to regulate local resistance and blood flow by releasing a vasoconstrictor agent, the noradrenalin [Levick 2010]. Additionally, tiny vessels (*vasa vasorum*) are usually present in the adventitia of large and medium-sized arteries, which are responsible for the nutrition of the middle layer. The cells found in tunica adventitia are predominantly fibroblasts, with occasional macrophages and Schwann cells. The thickness and structure of the adventitia vary according to the type and position of the vessel. In large arteries, the adventitia layer constitutes 10% of the vascular wall, increasing to 50% in muscular arteries, while it is indistinct in arterioles and venules.

In large elastic arteries, the external elastic lamina is not distinct, however, there is a fibrous tissue sleeve around the media layer, formed by thick bundles of

collagenous fibrils accompanied by a loose network of elastic fibres. Nevertheless, as the elastic arteries decrease in size an external elastic lamina appears, which becomes clearly distinct in the muscular arteries. The adventitia in muscular arteries is composed of longitudinal bundles of collagenous fibrils in the inner part, while in the outer part the collagenous fibrils are arranged circumferentially. Longitudinally arranged elastic fibres are also found in this layer in muscular arteries. As the muscular arteries approach the arterioles, the adventitial layer decreases significantly, the external elastic membrane becomes hardly distinct, while the bundles of the collagenous fibrils become denser, and are only arranged longitudinally.

As one could conclude, it is the individual arterial components and their organisation that give the arterial wall its mechanical properties, which are essential for the normal function of the entire cardiovascular system.

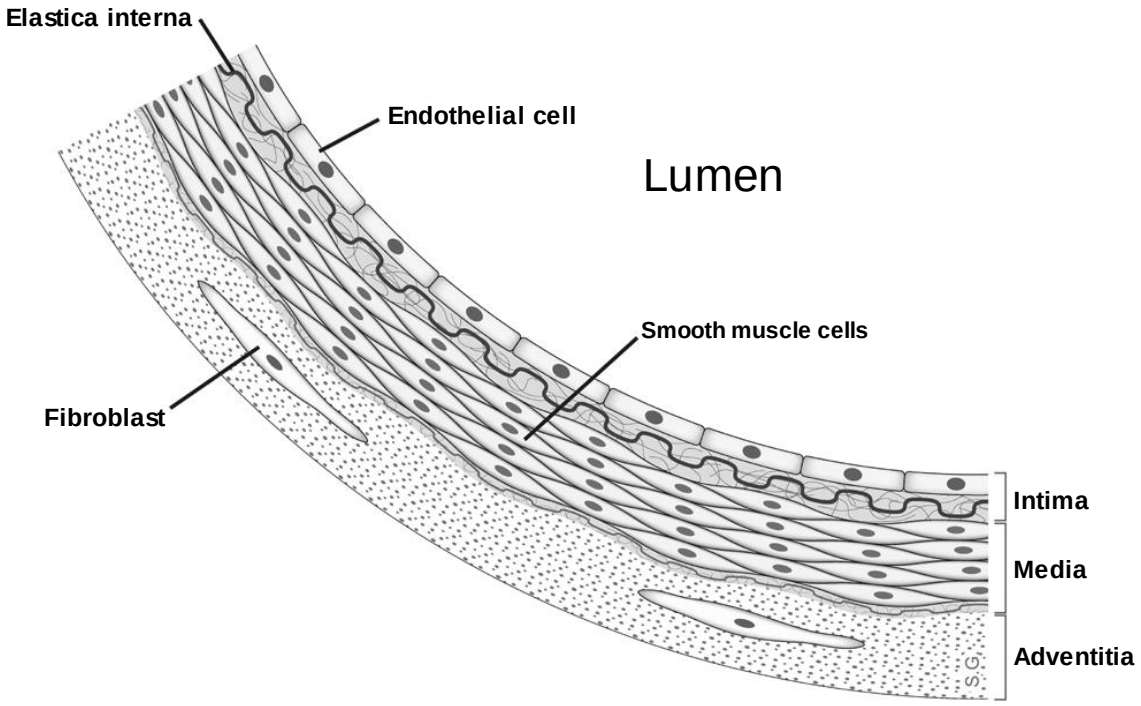

Figure 2.16: Schematic of a medium-sized artery [Aging Research 2010]. The schematic illustrates the components and the organisation of the arterial wall.

2.1.2 Mechanical properties of the arteries

The size of the blood vessels is inversely proportional to their distance from the heart. In addition, all the vessels are composed of different amounts of collagen, elastin, and smooth muscle layers. These components may have different structures

and carry different properties. As with most soft tissues, blood vessels can be characterized as viscoelastic [Fung, 1993]. An example of a typical viscoelastic behaviour of soft tissues is shown in Figure 2.17. For relatively small strains, this behaviour remains linear, and thus for small deformations, these materials obey Hooke's law. Additionally, investigations suggest that Poisson's ratio is approximately 0.5 [Nichols and O'Rourke 1998].

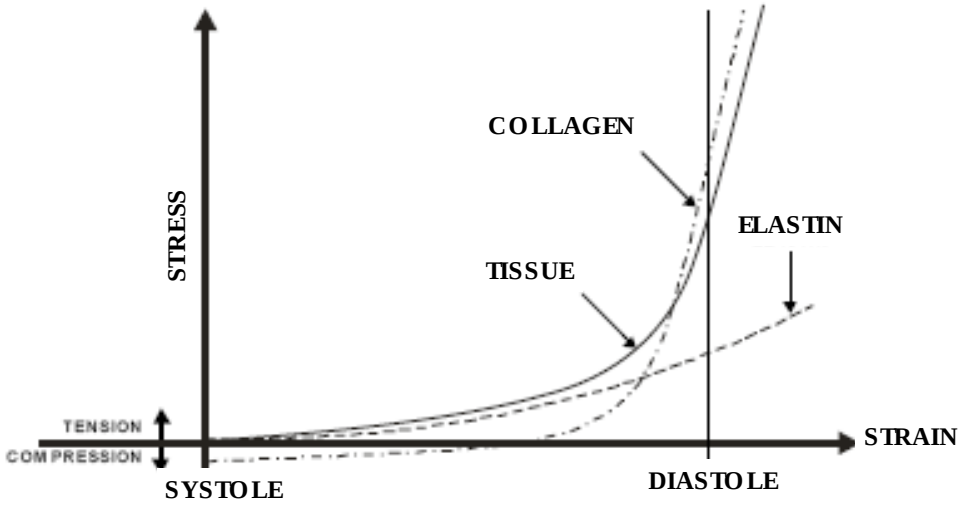

Figure 2.17: Typical stress-strain relationship of collagen and elastin in soft tissues. [Korossis 2002].

Blood vessel	**Internal** ∅ (mm)	**Thickness** (mm)	**E** (MPa)	**Reference**
Aorta (anterior wall)	n/a	2.35	0.824	Tseders & Purinya, 1975
Aorta (posterior)	n/a	2.26	1.000	
Descending thoracic aorta	19.30	n/a	0.076	Pearson *et al.,* 1994
	16.40	n/a	0.068	
Abdominal aorta				
	11.61	n/a	0.052	Sonesson *et al.,* 1993
Carotid				
Common carotid	n/a	1.66	0.765	Tseders & Purinya, 1975
Internal carotid	n/a	1.60	0.800	
Femoral	n/a	1.90	1.000	Tseders & Purinya, 1975
Common iliac	n/a	1.63	0.950	

Table 2.1: Summary of the Young's modulus (*E*) and physical properties of arteries. The significant difference in these values derives from the fact that the mechanical properties vary according to the histoarchitecture of the arteries, which in turn depend on the position of the artery inside the body.

The elastic modulus of different human blood vessels, evaluated experimentally and reported in the literature are summarised in Table 2.1. The assessment of the blood vessels' mechanical properties involved the methods of echocardiography [Pearson *et al.* 1994], phase-locked [Sonesson *et al.* 1993, Kawasaki *et al.* 1987], ultrasound [Lanne *et al.* 1992], and tensile testing [Tseders & Purinya 1975]. The experimental evaluation of elastic modulus of an artery depends on several factors, such as tissue preparation and testing conditions, the technique used to measure arterial diameter, and the age of the subject. Other parameters include the specific histoarchitecture of the particular blood vessel and its content in collagen, elastin and cells.

2.1.3 Mechanical properties of vascular cells

The cells' mechanical properties have a significant effect on the behaviour of the tissue they compose. Within the body, the cells experience relatively severe forces. Their mechanical properties allow them to withstand such loads and also to perform their physiological function at the same time. In an artery, the most abundant cells are the ECs and the SMCs. Because of their position in the artery, the ECs are exposed to shear stresses due to the blood flowing within the lumen of the vessel [Sato *et al.* 1996], while the SMCs deform due to the vascular dilation [Liao *et al.* 2006].

The main methods that have been used to date to assess the mechanical properties of cells include micropipette aspiration [Sato *et al.* 1996, Liao *et al.* 2006, Lim *et al.* 2006] and atomic force microscopy (AFM) [Sato *et al.* 2006]. The micropipette aspiration technique has been used to assess the constants of homogeneous standard linear solid models that have used to describe the viscoelastic behaviour of cells [Lim *et al.* 2006]. Some of these constants are listed in Table 2.2, with k and μ representing the spring and dashpot constants of the mathematical analogues of the cell behaviour. The values obtained from those investigations depend on several factors, including cell species, the technique used for cell isolation and the state of the cell [Hochmuth 2000]. Additionally, the cells, as living organisms, may change their structure during vital processes, which also affects their properties. The mechanical properties of the cells depend on their phase

cycle, the cell activity level, the neighbouring cells, as well as the surrounding environment [Starodubtseva 2009].

Another important parameter that affects the cellular mechanical properties is the exposure of the cells to mechanical loading. Sato *et al.* (2000), using the AFM technique, illustrated that the exposure of the ECs to different amounts of loading affected their properties, by increasing their stiffness. Similar conclusions were drawn in the study by Kim *et al.* (1999) after subjecting SMCs to cyclic mechanical strain. The variation of the cellular mechanical properties implies variation on the mechanical properties of the vascular wall. The structure and position of each artery inside the body, also affects the properties of the tissue as a whole. Nevertheless, possible defects may have a crucial impact on the structural organisation of the arteries, and consequently the physical and mechanical properties of the tissue.

Cell Type	$\mathbf{k_1}$ (Pa)	$\mathbf{k_2}$(Pa)	μ(Pa s)	**Reference**
Porcine ECs[a]	92±20	190±150	$7.2\pm2.7 \times 10^3$	Lim *et al.* 2006
Porcine ECs[b]	11±3	44±40	$1.3\pm1.1 \times 10^3$	
Porcine ECs[c]	28±5	65±44	$2.3\pm0.6 \times 10^3$	
Porcine ECs[d]	76±23	210±140	$8.3\pm4 \times 10^3$	
	~45	~75	$\sim3.4 \times 10^3$	Sato *et al.* 1996
Rat SMCs	19.99±2.86	7.19±1.21	25.36±6.14	Liao *et al.* 2006

Table 2.2: Summary of experimentally-derived viscoelastic constants of the arterial cells. [a] mechanically detached cells; [b] cytochalasin B treated cells; [c] colchicine; [d] trypsin-detached cells.

2.1.4 Main pathologies of the arteries

Small- and medium-sized vessel pathologies are the primary cause of death in Western societies [Yucel 2008]. Usually, such pathologies affect the inner wall of the vessels and lead to disturbance of the blood flow. This disturbance will restrain the normal distribution of oxygen and nutrients to the rest of the organs and tissues and may result in fatal diseases. During the aging process, the physical body undergoes dramatic changes. Blood vessels do not remain unaffected, as changes due to aging in the structure of the interior vessel wall may lead to a loss of its function. These changes involve the gradual loss of elastin and an increase in collagen density. This imbalance causes stiffening at the middle and the outer layers of the arterial wall, affecting the propagation of velocity and pressure waveforms to the distal vessels [Greenwald 2007, O'Rourke and Hashimoto 2007]. Other important

pathologies of the vessel wall include hypertension and thrombosis. Hypertension, or high blood pressure, is responsible for an increase in smooth muscle mass and extracellular matrix [Laurent *et al.* 2006, Humphrey 2008]. Thrombosis is mainly associated with blood clotting [Wooton and Ku 1999]. Both pathologies may lead to atherosclerosis or aneurysm.

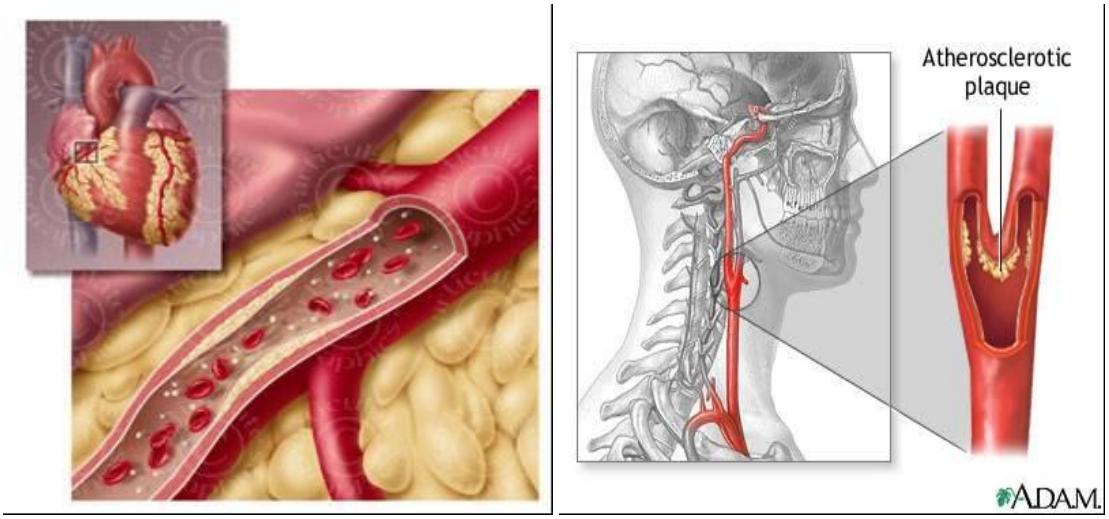

(a) (b)

Figure 2.18: Forms of atherosclerosis. The gradual development of the atherosclerotic plaque, caused by the deposition of plasma lipids to the lumen of the artery. (a) coronary artery disease (CAD) [Health Plan of New York, 2008]; (b) atherosclerosis in the carotid bifurcation [Coosa Valley Technical College, 2008].

Atherosclerosis is the most common and major arterial disease affecting the tunica media and the tunica intima, causing thickening and toughening on the arterial wall and leading to dramatic morphological changes in the interior of the vessels. Atherosclerosis tends to develop in individuals with high levels of lipids in the blood, such as cholesterol and fat. When these lipids are in high concentrations, they are likely to attach to the inner vascular wall. The gradual attachment of those lipids will develop a plaque; the atherosclerotic plaque. The development of the atherosclerotic plaque eventually results to the regional narrowing of the vessel, which causes restriction of the blood flow and mass transport to the tissues. In addition, the plaque may rupture leading to the release of plaque fragments to the blood stream, which could lead to the blockage of narrower vessels such as in the case of myocardial infractions in the heart (Figure 2.18a) and strokes in the brain (Figure 2.18b) [Humphrey 2002, Zarins *et al.* 1983]. Blood starvation can ultimately lead to tissue necrosis, due to insufficient delivery of nutrients and oxygen. The necrosis of tissues

is life-threatening, especially when this occurs in vital organs, like the heart and the brain.

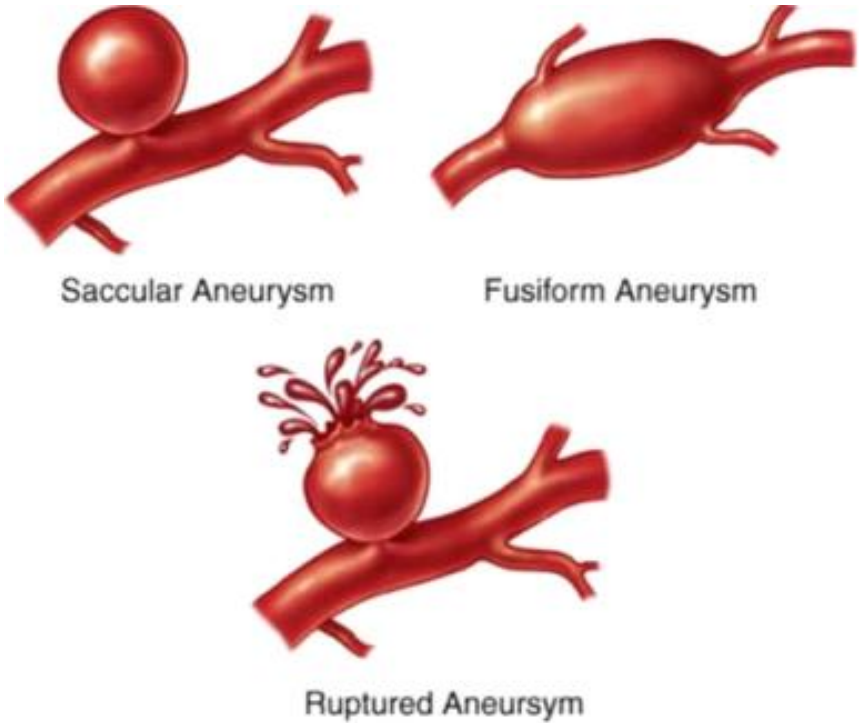

Figure 2.19: Forms of aneurysm [MedImaginery, 2008].

Another pathology that may be possibly caused by atherosclerosis is *aneurysm* formation (Figure 2.19). Overtime, atherosclerosis causes vessel walls to become less elastic, and a weak spot may develop. Aneurysms usually develop in weak parts of the arterial wall, where the vascular layers become stiff, due to atherosclerosis development. Aneurysm is a bulge in the weakened wall of an artery, which resembles a bubble in the wall of the vessel that consequently may suffer a catastrophic blow out [Martini 1989]. Several forms of aneurysm may develop, such as the *saccular* or the *fusiform* aneurysm. The ruptured aneurysm will lead to an internal bleeding, which is usually fatal. The most dangerous aneurysms are those involving arteries of the brain where they cause strokes, and of the aorta, where a ruptured aneurysm may cause fatal bleeding in a matter of seconds. The prevention and treatment of the arterial pathologies have preoccupied workers in the field and need particular attention, since they lack of symptoms and thus, are hard to detect. However, these pathologies occur due to the interaction of the arterial wall with the blood. It is of high necessity, therefore, to examine the blood composition and its

function, in order to obtain a better understanding of the development of the vascular pathologies.

2.2 The Blood

The heart starts beating at the end of the third week following fertilization of an egg in the developing embryo. The reason for this is that other organs have started their development, and consequently the oxygen and nutrients' consumption is of greater demand. At this point, simple oxygen and nutrient diffusion is not enough [Martini 1989]. The circulation of the blood is to serve several purposes not only for the development of the individual, but also to maintain balance in the organism via its components.

2.2.1 Blood composition and function

In contrast to other ECMs that contain networks of insoluble fibres, *plasma* is the blood ECM that contains dissolved proteins. Blood cells and cell fragments are the formed elements suspended in the plasma (Figure 2.20). The most abundant blood cells are the *red blood cells* (RBC), also known as *erythrocytes*, which are essential components for oxygen transport. The *white blood cells* (WBC), or *leukocytes*, are less numerous than the RBCs, however, they are necessary for the body's defence mechanism, since they are associated with the immune system. *Platelets* are small packets of cytoplasm that contain enzymes, and other factors that are involved in the process of blood clotting, which in case of an injury, acts as a temporary patch for the prevention of further blood loss. These elements, combined with plasma, form the blood. The multi-constituent nature of the blood allows different functions, necessary to maintain life. Blood is responsible not only for the transportation of dissolved gases, such as oxygen and carbon dioxide, but also for the transportation of nutrients, hormones, and metabolic wastes [Martini 1989]. In addition, blood regulates the pH and the electrolyte composition of interstitial fluids throughout the body, is responsible for the restriction of fluid losses through damaged vessels, the defence against toxins and pathogens, and for the stabilization of body temperature [Martini 1989].

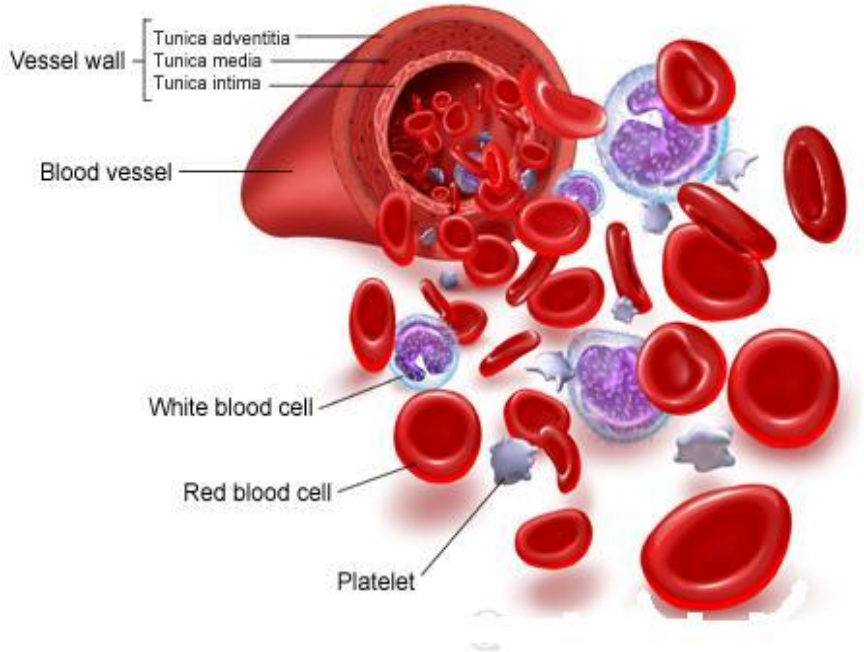

Figure 2.20: The elements that form the blood [Capillary Circulation 2010].

2.2.2 Physical properties of blood

Despite its multi-constituency, when treated as a fluid, blood has been modelled as homogeneous and incompressible [Nichols and O'Rourke 1998]. Moreover, its Reynold's number rarely exceeds the value of 2000, therefore, it can be treated as laminar [Nichols and O'Rourke 1998]. Blood is a non-Newtonian fluid, where its viscosity (~0.00345 kg/ms) is dependent on the haematocrit of the individual [Martini 1989].

2.3 Vascular Tissue Engineering

Malfunction of the human body has been the cause for the development of medical science. Congenital defects, disease processes or even an accident or trauma, may affect, damage or destroy an organ or tissue. Current treatments for these defects involve the repair of the defective body parts or their replacement with either prosthetic devices such as artificial joints and heart valves, autologous tissue (from another site of the patient's body) such as saphenous vein for coronary artery bypass and pulmonary valve for aortic valve replacement, or homogeneic tissue (donor tissues) such as heart valves, vascular grafts, liver, kidney, heart, and lung.

The progress in medical science has saved and improved the quality of life of many individuals, however all these approaches are subject to limitation.

Artificial replacements may cause inflammation and thrombosis, affecting more organs and tissues, and patients with prosthetic devices usually have to follow life-long anticoagulation therapy. In vascular surgery, autologous veins, and sometimes arteries, have been used to replace diseased arteries [Ratcliffe 2000]. However, in 10-40% of cases, autologous conduits are not available as a result of trauma, disease, or previous surgery, since the chronicity of these disease states results in inevitable re-operations [Yow *et al.* 2006]. Moreover, the need for organ and tissue transplantation from another individual vastly outweighs the supply [UK Transplant 2008]. In addition, even if a patient manages to receive a transplant, they will need to take immunosuppressive drugs for the rest of their life. Immunosuppressive drugs leave the patient susceptible to infection, which may raise other health issues. Last but not least, the cost of organ transplantation and the drugs required to sustain the transplant is very high.

Due to these limitations, scientists seek alternative approaches to treatments and therapies of defected organs and tissues. Recently, researchers in the field have focused in the relatively new field of tissue engineering or regenerative medicine. Tissue engineering can be defined as the development of biological substitutes for implantation into the body and/or the fostering of tissue regeneration and remodelling, with the purpose being to replace, repair, maintain or enhance function. This purpose can be achieved by developing non-immunogenic, functional tissue and organ replacements, characterised by physiologically-appropriate mechanical and biological properties, off-the-shelf availability, short cultured periods *in vitro*, and predictable clinical efficacy [Bozkurt 2008, Yucel 2008, Edelma *et al.* 1999].

Tissue engineering aims at tissue regeneration using either direct injection of appropriate cells to the diseased site, or scaffolds seeded with cells *in vitro* (with or without physical conditioning) prior to implantation to the diseased site [Yucel 2008]. The use of cell-scaffold constructs involves the *in vitro* culture of isolated cells, which are then seeded onto a natural or a synthetic scaffold. After appropriate cultivation time, the cell-scaffold construct is implanted into the host. The scaffold not only provides structural support, but also functions to guide the development of the new

tissue [Julie *et al.* 2001]. Vascular tissue engineering scaffolds are tubular conduits or materials capable of being fashioned into blood vessel configurations that are neither cytotoxic nor thrombogenic [Yow *et al.* 2006]. The role of the scaffold is to bring the cells (ECs, SMCs, fibroblasts) close to each other in order to facilitate intracellular communication, which leads to cell adhesion, migration and differentiation. Moreover, the scaffold should meet the physical and mechanical properties of the natural ECM, in order to withstand the *in vivo* forces [Yow *et al.* 2006]. However, the challenges to the success of such a scaffold are numerous. The physical parameters of a natural blood vessel need to be translated, in terms of mechanical, biological and chemical properties and function. Despite the great investigation that has been carried out – especially with regards to the physical and mechanical properties – our understanding on the interaction between the cells and the ECM is still limited. The aim of the following text is to describe the attempts of the researchers to construct a tissue engineered blood vessel, and to focus on the issues and challenges that were raised during this process.

Biological scaffolds, non-biodegradable and biodegradable polymer scaffolds seeded with cells have been used in vascular tissue engineering [Bozkurt 2008; Yucel 2008; Yow *et al.* 2006]. The different strategies used to develop tissue engineering blood vessels (TEBV) are presented in Figure 21.

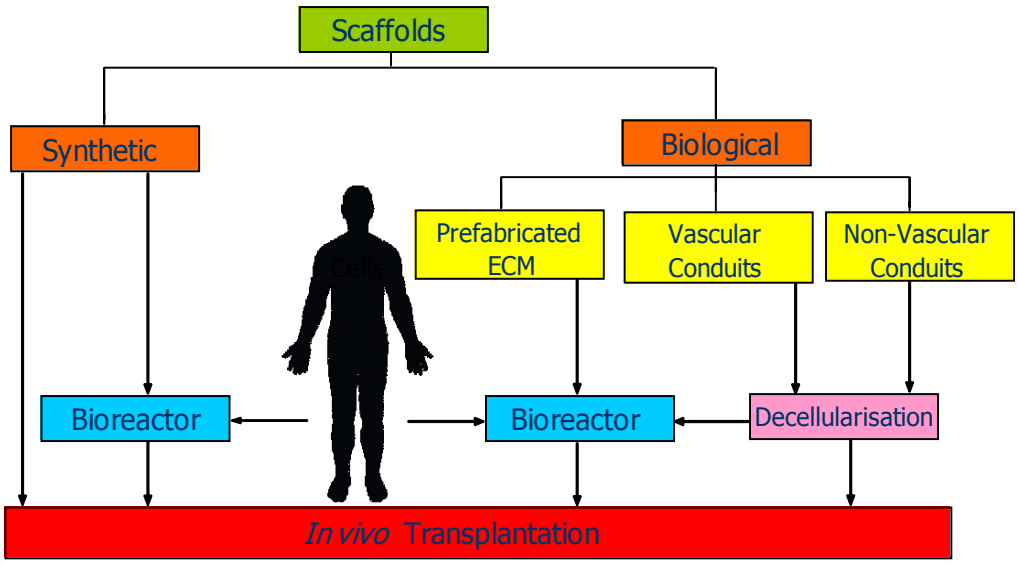

Figure 21: Schematic of vascular tissue engineering approaches. The schematic illustrates the reported methods used in the development of TEBV. These involve the use of (a) synthetic scaffolds and (b) biological scaffolds. Scaffolds have either been directly implanted in the human body, or have been imposed to cell-seeding prior implantation, with the aid of specially designed bioreactors.

2.3.1 Vascular tissue engineering using synthetic scaffolds

Synthetic scaffolds have the advantages of industrial scale production, and biochemical and mechanical qualities determined at the point of manufacture. These include degradation products, degradation time, compliance, tensile strength, conduit size and configuration [Campbell *et al.* 1999, Berglund, 2003]. Biodegradable polymer ECMs are usually made from polyglycolic acid (PGA), poly-L-lactic acid, poly-D, L-lactic-co-glycolic acid and polyurethanes [Kim and Mooney 1998, Tiwari *et al.* 2002, Niklason, 1999 and 2001], while non-biodegradable scaffolds include polytetrafluoroethylene (PTFE, ePTFE) [Herring *et al.*1994, Gosselin *et al.* 1996] and Dacron [Schmidt *et al.* 1984]. However, such materials do not meet the properties of a natural scaffold and usually do not allow cell attachment. Furthermore, synthetic scaffold degradation products may cause intimal hyperplasia or inflammation [Yow *et al.* 2006, Tiwari *et al.* 2002, Tai *et al.* 2000].

Polytetrafluoroethylene (PTFE) and expanded polytetrafluoroethylene (ePTFE) implants are made of a carbon and fluorine based synthetic polymer that is biologically inert and non-biodegradable in the body, while Dacron is a condensation polymer obtained from ethylene glycol and terephthalic acid [Ratcliffe 2000]. The use of these materials has proved successful for treatments of pathologies of large vessels, however they have been associated with finite durability, thromboembolism, and poor intermediate and long-term patency rates, in vessels with a calibre of less than 6mm, mainly because of biological reactions at the blood-synthetic material interface [Ratcliffe 2000, Yow *et al.* 2006]. In 1994, Herring *et al.* (1994) compared ePTFE and autologous vein grafts in order to determine whether endothelial seeding could improve the patency of ePTFE femoral popliteal bypass grafts and to determine whether endothelial seeding could be performed consistently in multiple institutions. They concluded that autologous vein graft patency was better than ePTFE seeded grafts, and that seeding did not improve patency. Moreover, they demonstrated that failure of seeded grafts was associated with anastomotic hyperplasia but not with the failure of initial endothelial attachment.

Gosselin *et al.* (1996) tested a fibrin glue (FG) containing fibroblast growth factor 1 (FGF-1) heparin coating as a surface for endothelial cell seeding in an effort to evaluate its impact on cell retention after exposure to pulsatile flow *ex vivo*. During this study, five pairs of ePTFE grafts of 4mm internal diameter were coated with

either FG/FGF-1/heparin or fibronectin (FN), which were then seeded with canine jugular vein ECs. The results demonstrated that the retention of canine jugular vein ECs seeded onto ePTFE grafts coated with FG containing FGF-1 and heparin was significantly higher than that of FN-coated grafts after 1 hour perfusion. According to the authors, these results seem promising, however they need to be confirmed for longer periods of perfusion and most importantly *in vivo*. Moreover, the functional characteristics of ECs seeded on those surfaces need to be systematically studied [Gosselin *et al.* 1996].

In 1999, Campbell *et al.* (1999) attempted to develop an artificial blood vessel conduit of any required length and diameter from the cells of the host for potential autologous transplantation. Silastic tubes of several lengths and diameters were inserted into the peritoneal cavity of rats and rabbits. After a period of 2 weeks, the tubes were covered by layers of myofibroblasts, collagen matrix as well as a single layer of mesothelium. These self-assembled tissues were removed from the tubing, everted, and autologously grafted by end-to-end anastomoses into either the carotid arteries or abdominal aortas. Results demonstrated patency for about 4 months, as well as the development of structures resembling elastic lamellae. Although the study had only a short follow-up, did not report on complications such as aneurysm formation or rupture, or attempt any mechanical characterization, it illustrates another feature of tissue engineering, namely that it is the cell environment rather than cell source that determines eventual function [Campbell *et al.* 1999, Berglund 2003, Yow *et al.* 2006].

During this period, Niklason and colleagues [Niklason *et al.* 1999] reported on efforts for the development of techniques to produce small autologous arteries *in vitro* from vascular cells grown on a biodegradable polymer matrix. After a period of culture of SMCs onto a highly porous and degradable poly-glycolic mesh in a tubular form, the scaffold was placed in a biomimetic system composed of specially designed bioreactors, in which the pulsatile perfusion system mimicked the forces that blood vessels are exposed to *in vivo*. After 8 weeks in culture the bioresordable mesh had been replaced by a SMC medial layer. Endothelial cells were then seeded onto the luminal surface to provide a representation of the layers of native arteries. The graft's properties included the ability to withstand more than 2000mmHg, as well as a collagen content of 50%. When autologous versions of these were implanted

into Yucatan pigs, they remained patent for up to 4 weeks. In 2001, the leaders of the same research group [Niklason *et al.* 2001] reported on the examination of the effects of culture time and tissue culture scaffold on engineered vessel morphology and function, since these parameters greatly influence the function of engineered vessels. During this study, engineered vessels were cultured from bovine aortic SMCs and ECs in the same way described above, although this time vessels were subjected to histologic, ultra-structural, immunocytochemical, and mechanical analyses. The results demonstrated improvement in the vessel morphology and mechanical characteristics when culture time was extended. SMCs in the engineered vessels wall were organised into a highly lamellar structure, with cells separated by alternating layers of collagen fibrils. These TEBVs maintained patency for 2 weeks after implantation into miniature swine, but gradual deterioration of the constructs eventually led to pathological responses and decreased blood flow, probably because of the highly acidic localised regions created by the residual PGA degradation causing strong inflammatory responses *in vivo* [Berglund *et al.* 2003, Yow *et al.* 2006].

Later on, the group of Wu *et al*. [Wu *et al.* 2012, Allen *et al.* 2014] introduced the cell-free approach and was the first reported group to demonstrate the long-term performance of microporous tubes, which were made by utilising elastic polymer, as vascular grafts in rat abdominal arteries [Benrashid et al 2016]. These tubes were developed by utilising heparin coated polyglycerol sebacate (PGS), reinforced with polycaprolactone (PCL) fibres as potential small arterial grafts. Characterisation of one year post-implantation revealed the remodelling to neoarteries, with the formation of all three layers and similar dynamic compliance to the native arteries. The group also reported no significant stenosis, dilation or calcification. This innovative cell-free approach, coupled with the use of a fast-degrading material, suggests that the remodelling process does not necessarily need to be slow, in order to prevent damage to the graft.

In 2016, another study [Hu *et al*. 2016] investigated the mechanical properties of knitted tubes with different knitting methods (warp and weft) using polyester (PET) yarns and spandex fibres. After performing tensile and compliance tests to the tubular grafts, the results suggest that the knitting method provide the grafts with different mechanical properties. Additionally, the study demonstrated that the use of

spandex fibres reinforces the elongation of the wrapped yarns and allows a greater compliance, compared to other commercially available grafts, such as PTFE and even to the natural blood vessels.

2.3.2 Vascular tissue engineering using biological scaffolds

Biological scaffolds may be categorised into three groups: prefabricated ECM [Weinberg and Bell, 1986, L'heureux et al, 1998], decellularised allogenic or xenogenic blood vessels [Teebken et al, 2000, Conklin, 2002], and decellularised non-vascular conduits [Badylak et al, 1989, Lantz et al, 1993, Matsuura et al, 2004, Darby et al, 2006, Schneider et al, 2016]. Contrary to the synthetic conduits, biological scaffolds carry all the physical, mechanical and chemical properties of a natural extracellular matrix, which allow cell signalling and eventually cell adhesion, migration, proliferation and differentiation. However, the direct clinical applications of such conduits [Spark, 2008], have been associated with aneurisms, thrombosis, as well as acute and chronic transmural inflammation.

The first TEBV to be constructed from natural materials was reported by Weinberg and Bell (1986). Their approach involved isolated bovine aortic ECs, vascular SMCs, and adventitial fibroblasts cultured *in vitro* on a collagen gel scaffold that had been prefabricated by culturing fibroblasts on a mandrel. The construct was composed of three layers, corresponding to the intima, media, and adventitia layers of natural arteries. Although the endothelial lining of this model functioned similarly to normal endothelium in several aspects (von Willbrand factor, permeability barrier for large molecules, existence of anti-thrombotic factors), the model did not meet the corresponding mechanical and structural properties of the natural artery [Yucel 2008, Yow *et al.* 2006, Edelma 1999].

L'heureux and colleagues [L'heureux *et al.* 1998] reported on improvements with regards to the mechanical strength of the prefabricated collagen gel scaffold-based graft by the addition of ascorbic acid to the culture medium. This approach resulted in a graft which illustrated fundamental morphological, histological and functional characteristics similar to natural blood vessels. Implantation into the femoral artery position in a canine model revealed a smooth thrombus-free luminal surface, retention of the graft architecture, and no signs of degradation, tearing or

dilatation (aneurysm). Another novel aspect of this graft was the presence of elastin fibres, which have a crucial role in the ECM. The most important disadvantage of this process, however, was the time needed for the production of this TEBV [Yow *et al.* 2006, L'heureux *et al.* 1998].

Another approach adopted by workers in the field is the use of decellularised xenogenic blood vessel scaffolds. Teebken *et al.* (2000) have reported on the development of a biocompatible and mechanically stable vascular graft combining human cells and a xenogenic acellular scaffold. Utilizing enzymatic cell extraction of porcine aortas they created decellularised scaffold tubes, which were seeded with human endothelial cells and myofibroblasts that had been isolated from saphenous veins. The constructs were subsequently conditioned in a pulsatile flow simulation system (bioreactor), duplicating physiological shear stress fields. Following conditioning in the bioreactor, the seeded endothelial cells generated a normal appearing endothelium in the lumen of the constructs. Although this model had many characteristics common to natural blood vessels and stable biomechanical properties at physiological perfusion pressures, the myofibroblasts failed to penetrate the scaffold. Nevertheless, it was postulated that the absence of cellular antigens, especially foreign endothelial-cell antigens, from decellularised scaffolds, and homology in the remaining ECM proteins (collagen, elastin, proteoglycans, structural glycoproteins) between human and swine, may prevent critical inflammatory or immune reactions to be induced by these decellularised tissue-based grafts.

The decellularised-xenograft tissue approach was also adopted by Conklin and colleagues (2002) who reported on the development of a novel small-calibre vascular xenograft using porcine common carotid arteries. The arteries were decellularised by enzymatic and detergent treatments and were linked with heparin in order to reduce thrombogeneicity. Histological results revealed complete removal of cellular components, and an intact ECM. Following a number of tests, they demonstrated the efficiency and anti-thrombogeneicity of the heparin-treated grafts. Burst testing revealed that the grafts were able to withstand pressures in excess of 10 times the systolic blood pressure. Implantation in a canine model as carotid artery bypass grafts, showed SMCs populating the wall and ECs lining the lumen by two months. According to the authors, this strategy could allow control of graft healing

and remodelling in order to achieve optimal clinical performance and avoid graft degradation.

In addition to vascular conduits, non-vascular tissues have also been employed as scaffolds in vascular tissue engineering. Since 1989, Badylak and colleagues (1989) have been investigating the potential of small intestinal submucosa as a vascular graft. Implantations in normal dogs revealed that this graft, when used as an autograft, allograft, or xenograft, demonstrated biocompatibility and high patency rates in the aorta, carotid and femoral arteries, as well as in vena cava locations. Following 28-90 days post-implantation, the grafts were completely endothelialised and histologically similar to normal arteries and veins. In 1993 the same group reported that there was no evidence of infection, intimal hyperplasia or aneurismal dilation [Lantz *et al.* 1993]. The authors suggested that this material may serve as a structural framework for the application of tissue engineering technologies in the development of a vascular graft.

Another non-vascular conduit that has been used in experimental vascular tissue engineering, as well as in clinical revascularisation surgery, is the Synergraft®. This conduit is a non-fixed, decellularised bovine ureteric graft, which has been reported to be capable of autologous cell repopulation by the recipient [Matsuura *et al.* 2004, Darby *et al.* 2006]. Matsuura *et al.* (2004) implanted 6mm-diameter bovine ureter Synergraft® conduits in dogs, as arteriovenous grafts. Some of these grafts were implanted between the carotid artery and jugular vein and some between the femoral artery and femoral vein. The reported 12-month primary patency rate was 58.6%, whilst after 10 weeks of implantation, histological and immunohistochemical analyses revealed fibroblast cell migration and proliferation, as well as no sign of infection. Darby *et al.* (2006) implanted Synergraft® conduits in patients aged 45-73 with a failed fistula or vascular access grafts. Patency was re-established in 14 out of 18 surgical interventions, and they reported that Synergraft® is a stable vascular access conduit, which provides a suitable graft alternative when autologous vein is not available. Recently, however, Spark *et al.* (2008) implanted Synergraft® conduits in patients aged 25-70 with a failed fistula or access graft in whom native vessels were unsuitable as conduits. They reported that some of the grafts developed aneurismal dilatation and some thrombosis. Moreover, histological assessment of the explanted bovine ureters revealed acute and chronic transmural

inflammation. In their report, they attributed the high failure rate of the bovine ureteric grafts to incomplete decellularisation and the presence of residual xenoantigens such as α-galactose (α-gal).

More recently, Schneider *et al.* [Schneider *et al.* 2016] investigated the potential of human placental chorionic plate as a vascular graft. In contrast with the limited access to other human-derived healthy tissues, the placenta is highly available in hospitals. Additionally, since it is already a human tissue, it presents a natural scaffold, and also, it neglects the risk of possible transmission of animal pathogens, when compared to xenografts. This group initially developed a decellularisation method, which involved a perfusion set-up that allowed shorter perfusion processes using lower concentrations of detergents. The outcome of this method indicated the effective removal of cellular components with no significant structural damage to the ECM. Tensile testing to the decellularised tissue confirmed a reduction of stiffness and ultimate tensile strength, but it still remained within the range of in vivo situations. Following, recellularisation of the tissue was performed using primary endothelial cells, which led to endothelialisation while maintained phenotypical characteristics cell specific expression patterns. Additionally, the high viability of the cells indicated the limited effect of the chemicals that were used during the decellularisation process. However, further research is necessary in order to investigate the in vivo performance of the graft and its potential as an off-the-shelf available product.

2.3.3 Conclusions

Despite remarkable advancements in the field of vascular tissue engineering, a completely biological vascular graft that meets the challenge of adequately replacing a diseased small-diameter (internal lumen <6mm) blood vessel has yet to be developed. The relative success of prefabricated ECMs, in duplicating a degree of the mechanical properties of natural vessels, provides a motive for further investigation. Nevertheless, the time required for such an approach to generate implantable grafts seems disadvantageous. Decellularised vascular or non-vascular xenografts, with or without *in vitro* cell seeding, offer a great advantage by closely duplicating the histoarchitecture and mechanical properties of normal tissue [Booth

et al., 2002, Korossis *et al.*, 2005]. In addition, xenograft availability and the potential of producing non-immunogenic grafts, by effective removal of xenograft antigens, is a much desirable combination, in terms of availability. Nonetheless, further research is needed regarding *in vitro* cell seeding and maturation, and *in vivo* performance including the graft's ability to remodel and develop with the patient.

An important aspect of *in vitro* vascular tissue engineering is the highlighted need for functional simulation systems for the conditioning/culture and the mechanical stimulation of the cell-seeded scaffolds. It is important, however, that these systems are able to expose the developing conduits to physiologically-relevant biomechanical (pulsatile flows and pressures) and biochemical stimuli in order to stimulate appropriate cell function and blood vessel-equivalent regeneration [Niklason *et al.*, 1999, Teebken, 2000]. The issue that arise at this point involves the methods for assessing the type and magnitude of such biomechanical stimuli that is experienced by the seeded cells to regulate their function. To this view, it is crucial to understand the cellular pathways and how these relate to their microenvironment. The text to follow describes the conclusions of the research activity on the interaction between the cells, the ECM and the blood flow.

2.4 Cell-flow and cell-ECM Interaction

The human body comprises of approximately 200 different types of cells. The cells produce the ECM to form the tissues, which in turn form the organs. Nevertheless, tissue formation requires an organised structure of cells and ECM to provide the appropriate stimuli, signalling, properties and function. The pathways that cells undergo towards this organisation have attracted great attention, especially in the area of tissue engineering and regenerative medicine. The conclusions drawn up to date after studies on this field, suggest that this organisation comes in response to ECM surface, chemical signalling and mechanical stimuli [Schwarz & Bischofs 2005, Shamloo *et al.* 2015].

The surface and the consistency of the ECM contribute significantly to the cell binding, migration and proliferation. Related studies have demonstrated that the biochemical composition of the ECM and adhesive environment [Zaman *et al.* 2006], the geometry [Peyton *et al*. 2011] as well as the fibres distribution [Shamloo *et al*. 2015] have a significant effect on the cellular pathways and chemical signalling. The

chemical signalling is of great importance, not only for the interaction between the cells and the ECM, but also for the interaction between the cells themselves. The cell-cell interaction affects the collective cellular responses to the surrounding microenvironment, which assist in the cellular organisation towards the creation of functional tissue [Shamloo *et al*. 2015]. Additionally, mechanical stimuli, such as external loads, are also responsible for the microenvironment conditioning.

In the case of the blood vessels, the translation of the mechanical stresses to chemical signalling (mechanotransduction) is realised via the vascular cells (ECs, SMCs). The mechanical stresses are derived from the blood flow within the vessel walls. It has been previously demonstrated [Langille & Adamson 1981; Nerem *et al.* 1981] that the shape and orientation of the endothelial cells depend on the flow behaviour. Additionally, the endothelial cells are subjected to both shear stress and cyclic strain *in vivo*. Furthermore, reported experiments demonstrated that when mechanical loading was applied to the SMCs, there was an increase in the presence of collagen and elastin within the seeded tissue, compared to the situation when no loading was applied [Kim *et al*. 1999].

The cellular pathways are complicated and not yet fully understood. However, it is assumed that the stresses experienced by the vascular cells activate several cellular events. These events lead to the production of factors, which are necessary for the regulation of homeostasis, prevention of diseases, cell differentiation and wound healing.

It can be concluded that mechanical stresses are vital for the proper function of the vascular cells. The question that remains unanswered is what is the right amount of stresses that leads to the normal function of this tissue. The answer to this question will be of great importance for the development of the functional simulation systems (bioreactors) for the conditioning of functional tissue engineered vascular grafts. Since the understanding of cellular mechanotransduction depends on the understanding of several factors, which is difficult to achieve using traditional experimental methods (such as mechanical stresses), scientists have sought alternative methods for determining the extent of mechanical stimuli, under which cells function properly. These methods involve computational techniques and *in silico* simulations. The progress of the numerical platforms allows the computational modelling of several biological processes at different scales (macro and micro). In

the case of the vascular system, where the blood dynamics affect significantly the microenvironment, the computational simulations at the macro-scale may expand our understanding on the fluid behaviour and may also provide information that can be used to construct simulations at the micro-scale.

2.5 Computational Methods

Computational methods involve the mathematical interpretation of physical systems with the aid of computers. The recent computational evolution, the great progress in technology and the development of sophisticated computational means provide the advantage of solving extremely complicated physical problems. The time and the equipment needed for such solutions to be obtained are also great advantages that this approach offers. In addition, computational simulations are easier to construct, especially when compared to experimental methods. To date, there is a great availability of user-friendly softwares, which are based on numerical analysis and theoretical computer science, and they are used in the broad field of physical science.

However, the numerical methods carry drawbacks. The solutions that are obtained when using such means are approximations, and thus, numerical errors are involved, which may lead to the wrong interpretation of the results and false conclusions. For this reason, experimental or (when possible) analytical validation of results is necessary before considering a numerical trial as reliable or as a foundation for further applications. Moreover, despite the low cost when compared to other approaches, numerical methods still require equipment, such as processors and computer memory (CPU), to be sufficient for running the simulations. Such equipment may carry great cost, and in many cases does not even exist.

Nevertheless, the option of the computational simulations is the most attractive method to describe complex physical systems and to expand our understanding on them. For the purposes of the present investigation, the following text is focused on the computational methods, which have been used to describe the blood flow.

2.5.1 Computational Fluid Dynamics (CFD)

About three hundred years have passed since the Swiss scientist Leonhard Paul Euler (1705-1783) managed the mathematical interpretation of inviscid fluid flows [Li 2004]. Following, Claude-Louis Navier (1785-1836) and Sir George Gabriel Stokes (1819-1903) established the mathematical equations that would describe flows of fluids with more complicated properties and behaviour [Li 2004]. These mathematical advances found applications in numerous areas, such as aerodynamics, thermodynamics, hydrodynamics and meteorology, and are still employed in solving advanced physical problems where fluid dynamics are involved. The broadness of computational fluid dynamics finds applications also in the biomedical field, and more specifically to the numerical modelling of vascular fluid flow.

In the early 1950s, the mathematical approaches in blood flow characterisation involved the assumption of a velocity profile which is greater along the vessel axis and is decreasing as it reaches the walls [Taylor and Humphrey 2009]. Under this assumption, equations of velocity and pressure were averaged over the cross-section of the vessel, producing a system of nonlinear partial differential equations in a single variable of space and time [Hughes 1974]. Based on the mathematical description of mass and momentum, further assumptions followed for the calculations of the pressure and flow rates throughout the vascular tree, including branching points. Womersley (1955, 1957) developed a theory of pulsatile flow in elastic vessels under the assumption of linearity, which was employed to model wave propagation in the human circulatory system under normal [Avolio 1980] and pathological conditions [Balar et al 1989, Hillen et al 1986, Raines et al 1974]. The development of 3D computational modelling of blood flow started in early 1990's, and its improvement is growing with the progress of technology. This approach provided data that was hard to obtain either with 1D or experimental methods, such as wall compliance, mass transport, time and geometric variations [Perktold *et al.* 1991a,b, 1993, 1995, 1997, Steinman *et al.* 1993, 1994, Lei *et al.* 1997].

CFD simulation involves the construction and the solution of the model. The first step is the definition of the components engaged. In the case of vascular modelling, these components are the vascular geometry and the fluid flow. The

simulation of the blood vessel can be identified either as a simple straight tube, or, for more anatomical detail, it can be segmented and reconstructed by medical imaging, such as X-ray angiography [Gibson et al 1993, Tasciyan et al 1993, Leung 2006], ultrasound [Chandran et al 1996, Krams et al 1997, Ilegbusi 1999, Liu 2001], CT [Jin et al, 2004, Nørgaard et al 2014] and MRI [Long et al 1998a,b, 2000a,b, Wang et al 1999, Zhao et al 2000, Ladak et al 2000, 2001]. The defined geometry is then discretised (meshed) into volumetric elements (spatial discretisation). The mesh refinement contributes significantly to the accuracy and the stability of the results, along with the temporal discretisation (i.e. the division of the solution into discrete time steps).

The next step to follow for the construction of the physical model is the conditions imposed at the boundaries. The main surfaces in a vascular computational model involve the inlet boundary of the flow, the outlet boundary and the inner surface boundary of the vessel wall. Usually, a prescribed velocity profile is imposed in the inlet, a combination of velocity, pressure and traction conditions in the outlet, and the no-slip (zero-velocity) condition at the inner wall surface [Taylor and Humphrey, 2009]. The employment of such conditions has been reported to result in good approximations, when compared to experimental data [Scotti et al, 2005, Leung et al, 2006, Oscuii et al, 2007, Jafari et al, 2008]. Nevertheless, these approaches seem sufficient when velocity profiles and shear stresses are under investigation. In cases where pressure profiles or wall compliance are of interest, this form of boundary conditions seems insufficient and raises new challenges, since one needs the consideration of wall mechanics, fluid-structure interaction, as well as transport phenomena, such as oxygen and lipid transport.

The mechanical properties of the vessel wall have already been examined earlier (Section 1.1.3). It was shown that blood vessels exhibit viscoelastic characteristics, such as creep, stress relaxation and hysteresis. The most popular characterisation, however, seem to be the employment of elastic or hyperelastic material [Taylor and Humphrey, 2009; Scotti, 2005; Valencia and Villanueva, 2006; Oscuii, 2007]. Even more simplified properties have been reported in very recent publications, in which blood flow is examined through inelastic or rigid walls [Politis *et al.*, 2007, 2008]. In 2007, Maurits *et al.* (2007) compared flow waveforms through walls with several properties, including elastic and inelastic, and concluded that the

results produced could match the ones obtained *in vivo* by Doppler ultrasound, only when wall elasticity and positive peripheral resistance was taken into account. Nevertheless, according to Taylor and Humphrey (2009), the numerical models should capture the nearly incompressible, nonlinear, anisotropic responses under finite deformations.

Fluid-structure interaction (FSI) is associated with fluid flowing between deformable walls, and such deformation is mathematically given by the arbitrary Lagrangian-Eulerian formulation (ALE). This formulation is described in another chapter (Ch 3).

The computational simulations of the blood require its mechanical properties as a fluid, as well as a flow waveform to be imposed as boundary condition. Both factors seem to vary between the reported numerical models. This is because the flow waveforms are not different only from one individual to another, but also change during circulation. The mechanical properties of the blood also vary between individuals. Such variations may not affect the outcome of the simulation, however, that would depend on the examined parameters. Despite the non-Newtonian nature of blood, there is controversy regarding whether blood can be modelled as Newtonian. Some works suggest that non-Newtonian properties of blood are related to the shear-thinning [Gijsen et al 1999, Chen and Lu 2006, Siauw et al 2000, Tu and Deville 1996], while some others insist that the non-Newtonian effects are minimal and can be neglected [Perktold et al 1991, Cho and Kensey 1991, Valencia et al 2006, Lee and Steinman 2007]. When blood is modelled to flow within large arteries, it is usually assumed Newtonian, with a viscosity μ=0.0345 kg/ms [Soulis et al, 2008]. Johnston et al (2004) compared Newtonian and non-Newtonian blood viscosity models in coronary arteries, and concluded that there was little difference between wall shear stress distributions, and that the non-Newtonian importance factors were only significant during periods where the blood flow was quite slow. They also concluded that when flow is to be studied in more detail, rather than study wall shear stresses, a Newtonian model would not be sufficient [Johnston et al 2006]. Similar conclusions have been drawn by Soulis et al (2008), after investigation of 7 different non-Newtonian and one Newtonian fluid models for blood in coronary bifurcations. This investigation also illustrated that at mid and high strain rates, the Newtonian model results in good approximations. Nevertheless, the

mechanical properties of blood may vary, since the viscosity is closely related to the hematocrit of each individual [O'Callaghan et al 2006]. Moreover, non-Newtonian properties may contribute to the complexity of a numerical model, leading to the need for advanced computational means. Additionally, for patient-specific models, the measurement of each individual's viscosity is not convenient.

The non-Newtonian models that have been employed by researchers towards the determination of blood rheology involve the Carreau model [Giannoglou *et al.* 2002, Valencia and Villanueva 2006], the modified Cross Law model or Carreau-Yasuda model [Liepsch 2002], the Power Law model [Lee and Steinman 2007, Cho and Kensey 1991], the Generalised Power Law model [Ballyk et al 1994], the Casson model [Fung 1993], as well as the Walburn-Schneck Law model [Walburn and Schneck 1976].

Once all the above parameters are defined, the CFD solver will use this information to solve the Navier-Stokes and continuity equations until a final solution is reached (convergence). Then the solver will provide the available results, where the operator can extract during post-processing. The extracted information should then be subject to verification and validation [Oberkampf and Trucano, 2002]. Verification refers to mathematical issues and to the accuracy of the complex logical structures in computer codes. For the verification of the computational simulations, the results should be compared to analytical solutions. Of course, analytical solutions are not always available in very complex situations, therefore, validation is needed. Validation refers to the comparison between computational and experimental results (or other physical observations) to assess the accurate representation of the physical phenomena. Such a comparison will determine the accuracy and the reliability of the numerical simulation. When the simulation is proved accurate enough, the operator may extract further information, which is difficult to be determined experimentally, such as shear stress.

The recent advances in computational modelling have contributed significantly in our understanding of the blood circulation. These achievements have also extended our knowledge on how the blood flow has been related to the development of the vascular pathologies, such as atherosclerosis. Nevertheless, the effect of the haemodynamics on the vascular wall at a macro-level is not sufficient to identify the interaction at the cellular level, both with regards to disease initiation and

development, and also to the successful development of TEBV. Therefore, further investigation is necessary in order to determine the levels of stimuli imposed by the flow to the vascular cells, and how these stimuli regulate cell function. Those parameters are of high importance, since they have significant effect on the interaction between the cells themselves, and also between the cells and the ECM. Further investigation should involve the translation from the macro to the cellular level. The following text is focused on the research activity on the field and the reported attempts to interpret mechanotransduction pathways with the aid of experimental and/or computational means.

2.6 Simulation of the microenvironment

The simulation of the cellular environment is a great challenge. Researchers are called to mimic the complicated system of the physical body and to find ways to extract significant information about its function. The scale at the cellular level makes this process even more challenging for several reasons. Initially, the sensitivity at this scale is greater and thus the handling becomes more demanding. Furthermore, the equipment for such studies should be more sophisticated. For example, a microscope is necessary to enable the visualisation of a single cell, or the microstructure of a tissue. Consequently, the greater the resolution of the microscope, the more accurate the visualisation that will provide. Despite these challenges, several simulations have been reported, which have been carried out either experimentally or computationally, with regards to mechanotransduction.

The group of Screen et al [Screen et al, 2003, 2004, and 2005] initially developed a technique to determine the strains in tendons. With the aid of a specially designed rig, they achieved an immediate visualisation of strain effects on tendon fascicles. The rig was designed to fit under an inverted confocal microscope, to accommodate the secured mounting of the tissue specimen, and, with the aid of a stepper motor, to allow the controlled uniaxial stretching of the tissue. A schematic of the rig is shown in Figure 2.22. The researchers isolated tendon fascicles from rat tails and bovine extensor tendons, which were stained for cell nuclei, prior to the analysis. The cell nuclei were then used as markers, in order to determine the strain on the tissue fibres locally. Using the stepper motor, the samples were gradually stretched up to 4-5% of initial length in the axial direction, by 0.5% increments.

Despite the limitations of this procedure (such as the limited clarity of the cell nuclei images), this innovative technique was applied to investigate several hypotheses [Screen et al 2003, 2004, 2005] and the provided data may contribute to the development of more physiologically relevant *in vitro* simulations, to enable the further study of tenocyte mechanotransduction processes.

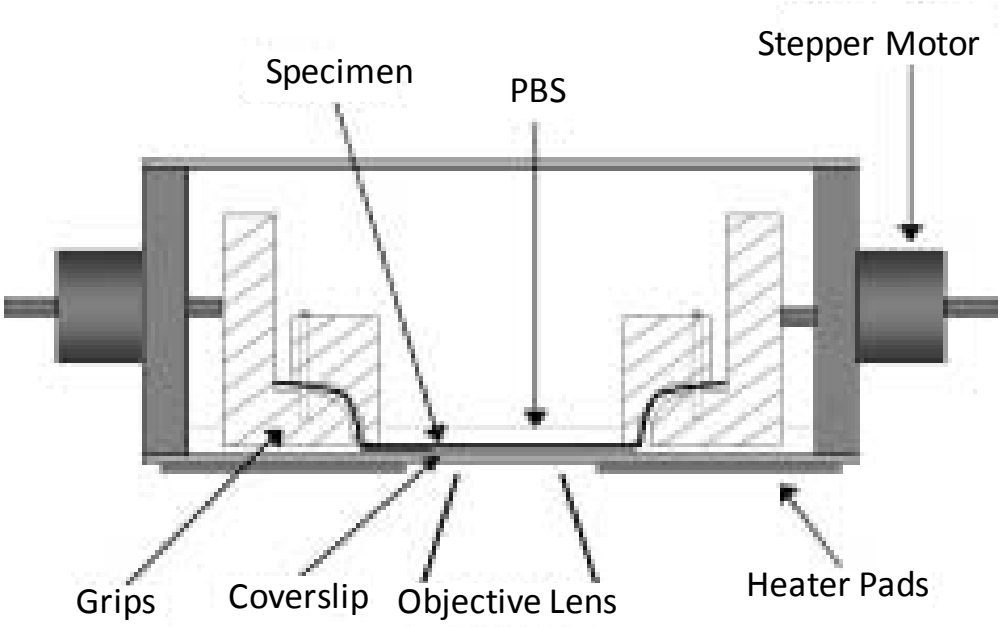

Figure 2.22: Schematic of the specially designed rig that was developed by Screen *et al* (2003) and was used for the micro-analysis of tendon fascicles.

Another attempt to understand the cellular mechanotransduction was reported by Chien [Chien 2007]. This procedure employed flow and stretch chambers, in which the cultured endothelial cells were exposed to shear stress and cyclic stretch. In the flow chambers, a monolayer of endothelial cells was placed in the bottom and was exposed to the flow, generated by a pressure difference between the inlet and the outlet of the chamber (Figure 2.23). The employment of an oscillatory pump allowed different pressure waveforms to be applied, either steady or pulsatile. A step flow chamber was also developed, using silicone gaskets to cause flow disturbance in certain regions, in order to study the effects of the disturbed shear (Figure 2.23). The cyclic stretch chambers allowed the deformation of the endothelial cells uniaxially and biaxially. As demonstrated in (Figure 2.24), a Teflon intender was pushed up against a silicone rubber membrane, while the endothelial cells were being cultured on it with a displacement ΔL.

The findings of this study included the effects of shear stress on mechanosensing, signalling, cell survival, cell proliferation and cell lipid metabolism. These findings were then compared to *in vivo* studies, where it was concluded that in

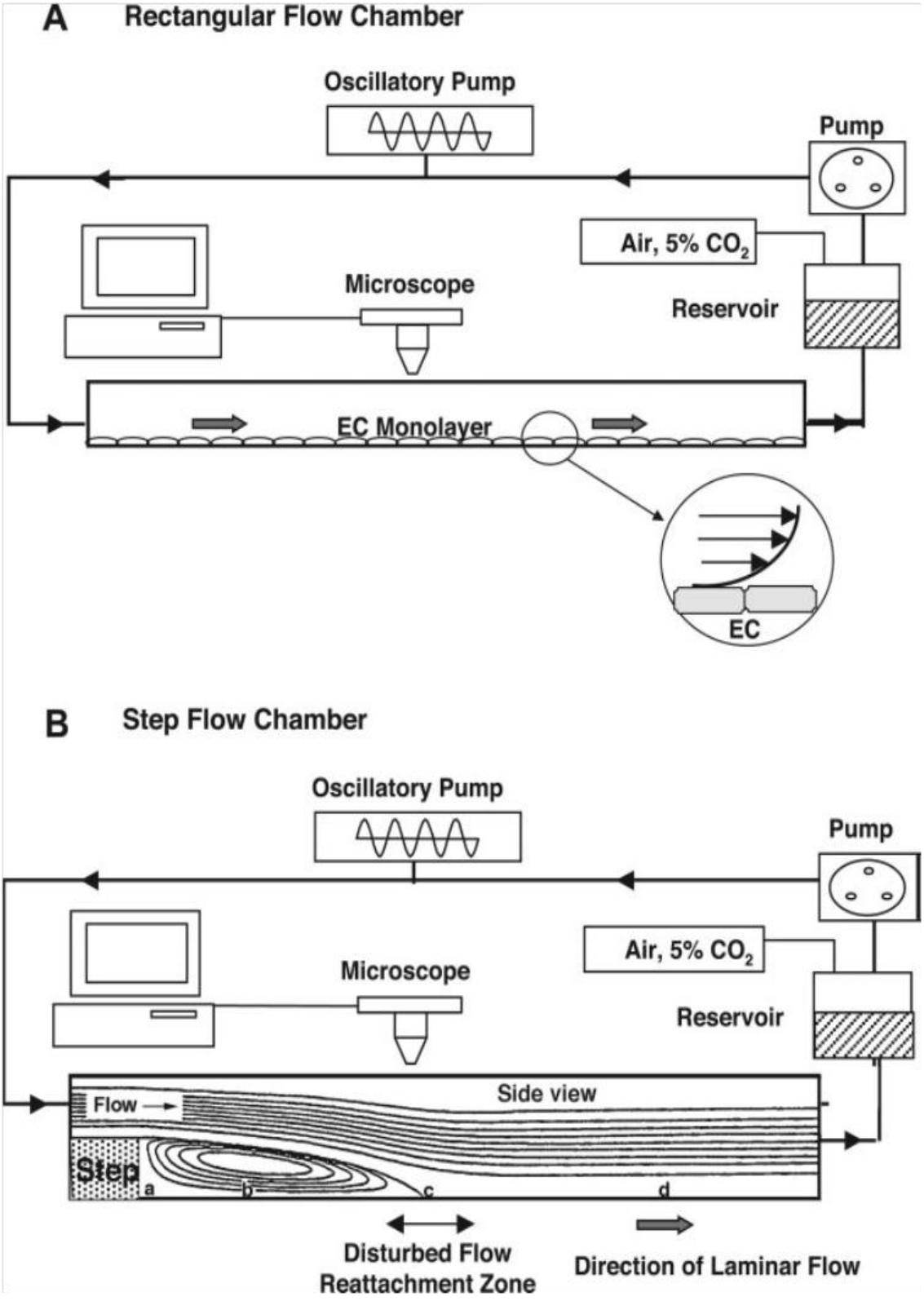

Figure 2.23: Schematic of (A) flow chamber and (B) step-flow chamber developed by Chien (2007).

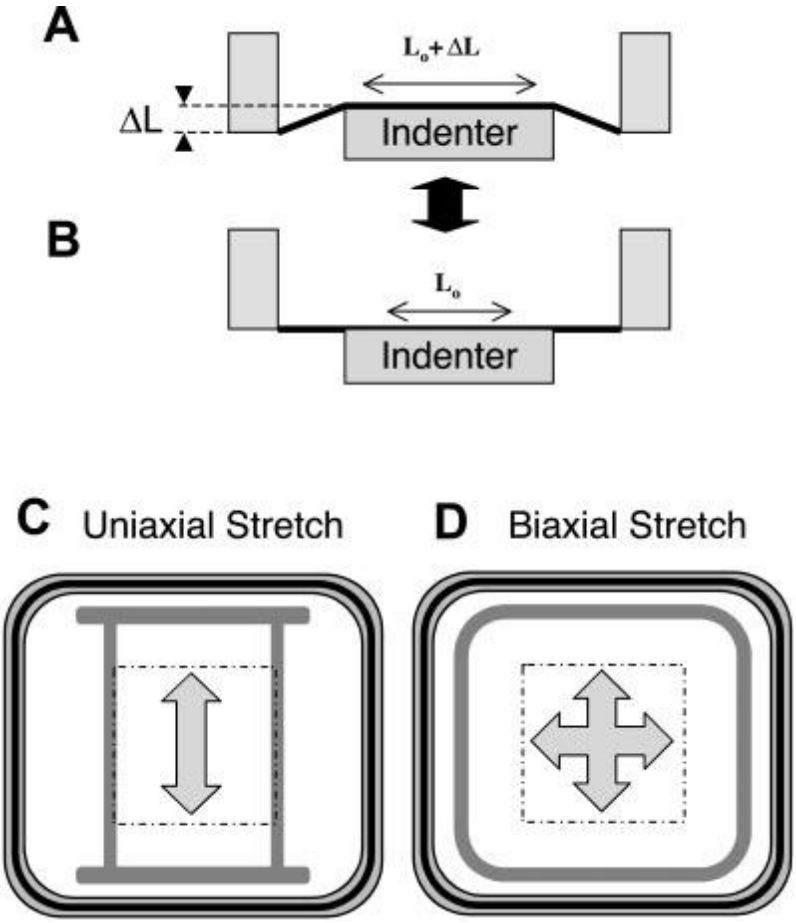

Figure 2.24: Cyclic stretching apparatus developed by Chien (2007). In A and B is the side view schematic of a stretch chamber and the indenter, where the indenter is pushing up the cell seeded membrane to result in a displacement of ΔL (A) and then back to its initial position (B). In C and D is the top view of the stretch chambers, for unilateral (C) and bilateral (D) stretches [Chien 2007].

the areas where the flow is steady (usually in straight parts of the blood vessels), shear stress is important for cell homeostasis and function, while in the areas that the flow is disturbed, there is a higher vulnerability to atherogenesis. Additionally, the effects of cyclic stretches on fibre remodelling, suggested that the direction of the stretching has a significant implication in cellular function. Again, at the straight areas of the blood vessels, where the blood flows uniaxially along the circumferential direction, cellular homeostasis is maintained, reducing proliferation and apoptosis, while, in branching areas, where the direction of the flow is disturbed, there is a great change in the cellular response, suggesting the high risk of pathogeneicity.

All the above studies have contributed significantly in our understanding on the cellular mechanotransduction. Additionally, the developed methodologies may

also be employed to study further the responses of the specific cells, or the responses of other kind of cells, *in vitro*. Further, such experimental simulations are also important, since the experimental findings may be used to compare numerical studies. As mentioned earlier, numerical simulations are developed in order to, either reduce the cost of an experimental procedure, or to extract information that are hard, or even impossible, to study *in vitro*. However, at least some of the parameters, obtained numerically, need to be validated with other findings, in order to reassure the accuracy of the numerical platforms.

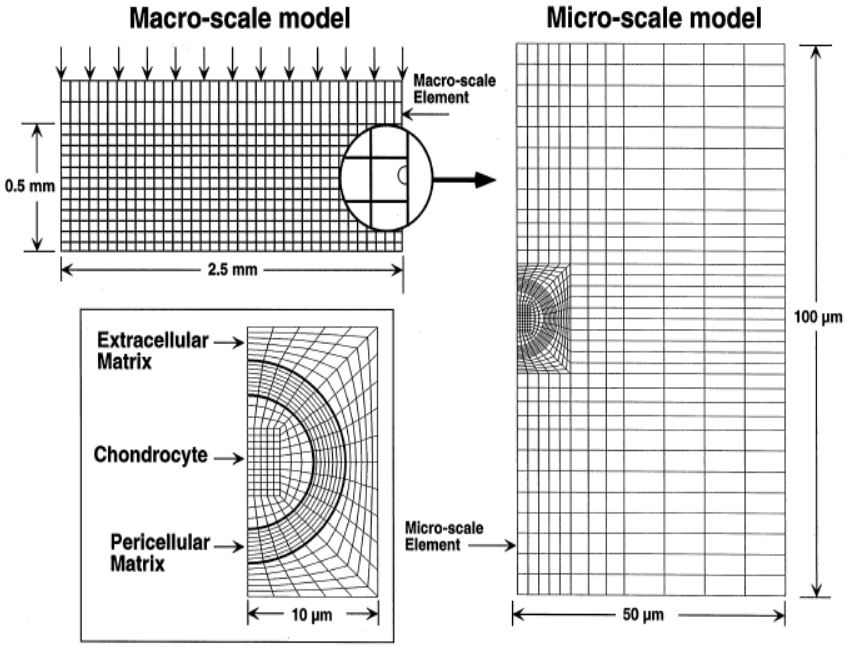

Figure 2,25: Description of the finite element models developed by Guilak & Mow (2000).

Several computational techniques have been developed in order to simulate the environment at the cellular scale. These include the simulation of intracellular processes [Klipp and Liebermeister, 2006], tissue formation [Johnson *et al,* 2004], as well as cellular microenvironments [Borau *et al* 2011, Chen *et al* 2012]. However, for the purposes of the present work, only relevant studies will be reviewed in the following text, such as the work of Guilak and colleagues [Guilak & Mow 2000, Alexopoulos *et al.* 2005]. This group has extensively studied the interaction between chondrocytes and ECM, using computational models. They developed a multiscale biphasic 2-dimensional finite element model, to investigate the effect of mechanical stimuli on chondrocytes (Figure 2,12). They first developed a macroscale model to

simulate the response of the ECM under compression. The results for the fluid velocity and the matrix displacement were then applied as boundary conditions for the microscale model. The microscale model involved a single chondrocyte embedded in the ECM. The cell was modelled as a spherical-shaped continuum homogeneous mixture of a solid and fluid. Although the validation of the obtained results was only based on analytical methods, the findings indicated that the magnitudes of the stresses and strains were much higher at the micro-level when compared to the ones found from the ECM simulation. Additionally, the presented results suggested that several factors affect the biomechanical influence of the cell, including the cell and matrix morphology, and the mechanical properties of both.

2.7 Conclusions

Tissue engineering and regenerative medicine have the potential to generate attractive alternatives to current approaches for vascular surgery. Despite the efforts of the researchers, a tissue engineered blood vessel to comply with the standards of the native tissue, has yet to be developed. In order to overcome this and progress towards a tissue-engineered blood vessel construct that would be suitable for vascular reconstructions, in the past few year studies have focused on investigating the microenvironment of native blood vessels, in order to extract information that could be potentially translated and applied in the conditioning and maturation of tissue-engineered vascular grafts *in vitro*.

Previous studies have shown that blood-flow-induced forces experienced by cells play an important role in regulating cellular function, and consequently, the maintenance of a healthy tissue. Therefore, there is a necessity in studying the effects of blood flow and defining the appropriate amounts of stress and strain under which vascular cells perform physiologically. These parameters, and especially the stress, are difficult to be obtained *in vivo* or *in vitro* without disturbing the blood flow. Computational modelling has emerged as the best alternative for this type of studies. Recent advances in numerical simulations and computer power, have allowed the accurate mathematical interpretation of complex physical phenomena. However, it is essential that these numerical simulations are validated against experimental *in vivo* or *in vitro* results, in order to determine their accuracy.

This validation usually involves at least one parameter, and when an adequate agreement between the computational and experimental results has been obtained, the computational simulation may be further used to extract information about additional parameters, which are difficult to be accurately measured experimentally. In spite of the paramount importance of the validation of computational models, there have only been a limited number of studies comparing computational simulation results to experimental ones [Shamloo *et al*, 2015]. This was most probably due to the lack of expertise and/or limited availability of equipment. Computational simulations offer several advantages, including easier setting up and less resources consuming compared to experimental simulations.

In spite of the challenges in studying the microenvironment of tissues *in vitro*, previous studies have reported on several methodologies aimed towards this objective. These methodologies have the potential to be further employed to investigate different type of tissues at the microscale, and they can also provide important information for developing numerical simulations. Previous studies have successfully investigated the mechanotransduction of the endothelial cells *in vitro* [Chien 2007]. However, the major cellular component of the vascular wall, especially in small-sized vessels, comprises smooth muscle cells. In addition to the aforementioned challenges in studying the cellular environment, the study of the microenvironment of smooth muscle cells in situ is even more challenging, since they are located in the vascular wall. Such investigation requires sophisticated equipment that would allow penetration and visualisation at a depth in the vascular wall.

Given the difficulties associated with the experimental investigation of the microenvironment that smooth muscle cells are exposed in situ, the development of physiologically-relevant computational simulations would allow the determination of the micro-stresses and -strains experienced by smooth muscle cells to regulate their function. Along these lines, the work conducted during this project was focused on investigating the interaction between macroscale strain, applied on femoral arteries, and the microscale strain experienced by smooth muscle cells in the arterial wall, with a view to optimising the conditioning of tissue-engineered arteries in a pulsatile flow bioreactor in order to achieve physiological vascular tissue remodelling and regeneration.

2.8 Rationale, Aims and Objectives

This project was based on the hypothesis that it is possible to quantify the strain experienced by the ECM at the microscale in response to the strain applied in the macroscale using numerical modelling. Towards this, the aim of the project was to develop multiscale computational models of small diameter (<6mm) vascular grafts, based on experimental data and natural histoarchitecture, in order to quantify the amount of strain experienced by the ECM and the vascular cells at the microscale under physiologically-relevant physical stimuli. This project was aimed at enhancing our understanding in the way that the strain acting on the vascular wall at the macroscale is translated to the cellular level, with a view to optimising the conditioning of TE vascular grafts in bioreactors and guiding appropriate cell function and graft regeneration.

Initially, a macroscale 3D model of the femoral artery was developed, which was based on the realistic geometrical and mechanical properties of fresh porcine femoral arteries that were obtained experimentally. Porcine tissue was chosen in this study due to its similarity to the human tissue, and its availability in local abattoirs. The macroscale computational model simulated the interaction between the pulsatile blood flow and the vascular tube (fluid-structure interaction; FSI) in order to investigate the effect of the blood flow and pressure on the deformation of the vascular wall. This model was validated against experimental data obtained by the dilation testing of fresh femoral arteries in vitro.

Following the development and validation of the macroscale model, a microscale 2D model of the porcine femoral artery was developed that was based on a realistic histoarchitecture, which was obtained from histological staining of the vascular wall. The microscale model used regional strain values that were calculated by the macroscale model as boundary conditions, in order to assess its effect on the strain experienced by the collagen and elastin fibres of the ECM of the tissue. The microscale model was validated experimentally by stretching a sample of cell-nuclei-stained fresh porcine artery and visualising it under confocal microscopy.

More specifically, during the course of the project the work focused on the delivery of the following specific objectives:

1. Development of macroscale FSI models using the LS-DYNA software platform to simulate the deformation of porcine femoral arteries under physiological pulsatile blood flow:

- Geometrical and material model:

Fresh porcine femoral arteries were assessed experimentally for their geometrical and biomechanical properties (stress-strain) with a view to capturing their macroscale geometry and devising a material model.

- Computational model:

The macroscale geometry of the femoral artery was reconstructed computationally and prescribed the material model. FSI computational simulations were conducted LS-DYNA in order to predict the strain variation in the vascular wall under pulsatile flow.

- Experimental validation

The strain results of the macroscale model were validated against experimentally-derived dilation data of fresh porcine femoral arteries obtained under dilation testing.

2. Development of microscale models to investigate the translation of the macroscale strain to the microscale strain experienced by cells:

- Geometrical and material model:

Fresh porcine femoral arteries were examined histologically to define the histoarchitecture of the collagen and elastin fibres of their ECM. Histological images were acquired under bright field microscopy and imported to Simpleware® ScanIP, where the individual components of the ECM were segmented.

- Computational model:

The segmented ECM histoarchitecture was imported to the ABAQUS finite element (FE) software platform and the material models were assigned to the different ECM components. Subsequently, FE simulations were conducted using regional strain values, calculated by the macroscale model, as boundary conditions.

- Experimental validation

The results of the microscale model were validated against experimental data obtained by stretching a sample of cell-nuclei-stained fresh porcine artery, using a controllable axial stretching rig, and visualising it under confocal microscopy. The confocal microscope enabled the visualisation and tracking of the stained cell nuclei

during stretching and, subsequently, the calculation of the ECM microstrain by the distance between cells before and after stretching.

Chapter 3. Investigation of the dilation of the arterial wall, using porcine femoral artery: Experimental approach

3.1 Introduction

The purpose of this investigation was to determine the strain in the wall (dilation) of porcine femoral arteries, as a function of the internal pressure on a macroscopic level. Additionally, the geometrical and the mechanical properties of the same arteries were assessed experimentally. The properties, including the length of the artery, the thickness and the diameter of the vascular wall, along with the Young's modulus of the tissue, were used substantially as input data for the FSI computational simulations, which are described in the next chapter. The findings of the dilation were used to compare the output results of the computational models. This chapter illustrates the experimental process towards this assessment.

3.2 Working with fresh tissue

The purpose of this project is to investigate the strain that the cells experience inside the body, under physiological function, where the cells are alive and active. The vitality of the cells affects the properties of the tissue and may provide inaccurate results during testing. To this view, the femoral arteries that used in this study were dissected from animals just a few hours after slaughtering, as will be explained later on in this chapter. However, from dissection to testing there was a time gap, where the arteries would be exposed to air, causing the dehydration of the tissue and cell death that would cause significant changes to its properties. In order to avoid this and to keep the number of the live cells as high as possible, a solution called transport medium was prepared as follows: 100ml Hank's Balanced Salt Solution (HBSS, Sigma Life Science), 110μl Aprotinin Stock (Rordic Pharma), 1.1ml Hepes stock (Hepes buffer, Lonza), 1.1ml Penicilin/Streptomycin stock, 110μl Gentamicin solution (Sigma Life Science). The salt solution provides the cells with water and it contributes to the maintenance of the physiological pH, along with the Hepes stock. Aprotinin is used to bind to the enzymes and decrease their function, to

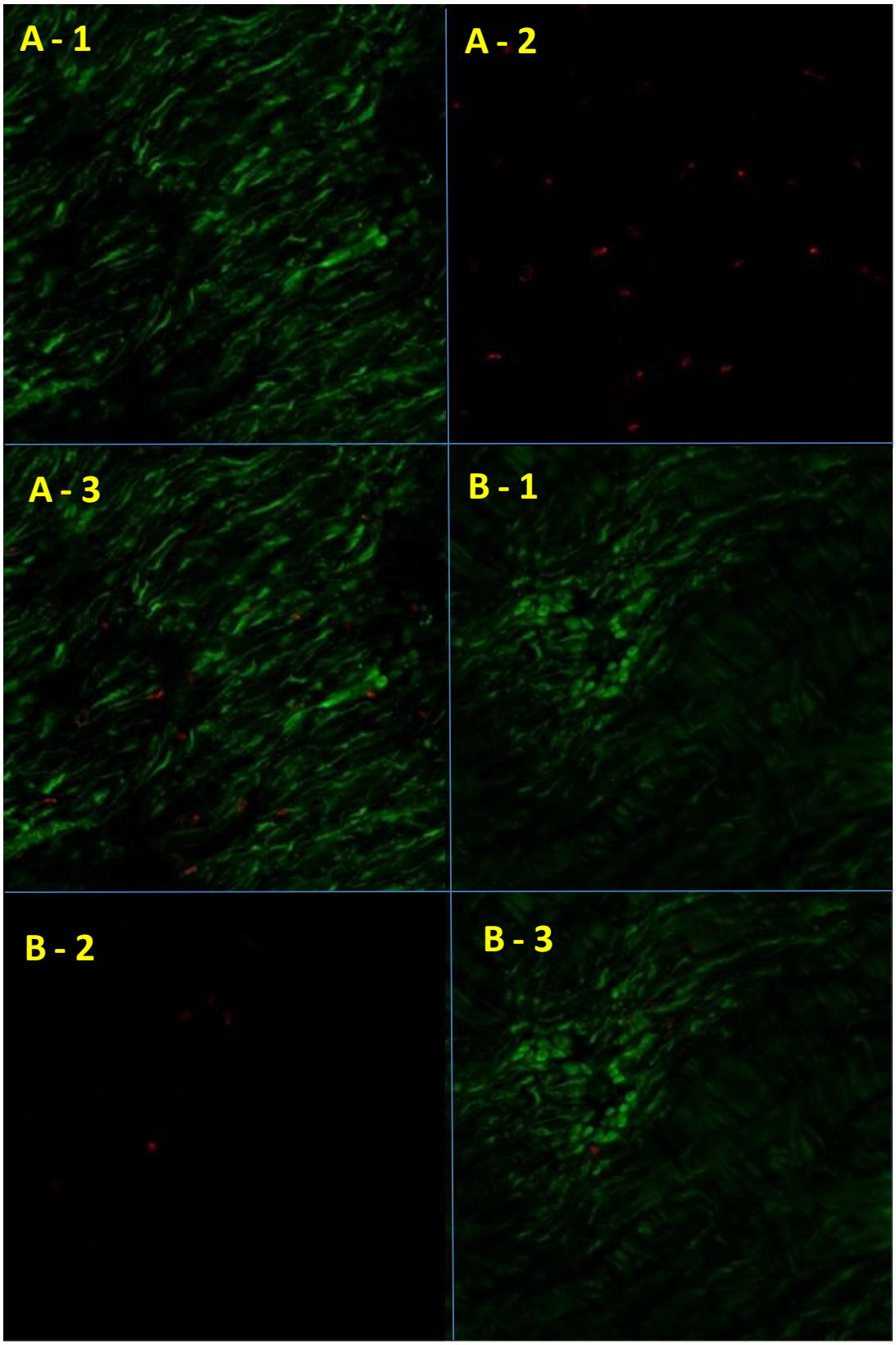

Figure 3.1: Cell viability test. The images indicated with A are from the sample that was treated with PBS, and B from the one treated with transport medium. Images A-1 and B-1 show the calcein fluorescence in live cells, while A-2 and B-2 the dead cells, which were stained with ethidium homodimer. The images A-3 and B-3 are the merged from the other two. In the second set of images, the number of the dead cells is much lower than in the first one.

prevent protein degradation. Gentamicin, Penicilin and Streptomycin are used as antibiotics, to prevent bacterial infections and possible contamination. Before further use of the transport medium, a cell viability test was performed to reassure its effect. One fresh porcine femoral artery was cut in half. One part of the artery was merged in a pot with transport medium and the other one in a pot with Phosphate Buffer Saline (PBS). The tissue in both pots was stained with calcein acetoxymethyl and ethidium homodimer-1 (Life Technologies) (4μl/10ml and 2μl/10ml respectively). Calcein is a cell-membrane permeable dye, which gives a strong green fluorescence after enzyme hydrolysis in live cells. On the other hand, ethidium homodimer is a non-permeable dye which binds to the DNA and emits red fluorescence. Both dyes are used to distinguish the live cells from the dead ones. After staining, the samples were washed three times, using the same fluid they were initially merged into, for 10 minutes each time at 120rpm. Images were then taken with upright confocal microscopy (Zeiss LSM510 META Inverted confocal microscope). The results are demonstrated in Figure 3.1. The ethidium homodimer has highlighted the dead cells that can be seen in Figure 3.1-A2 and B2. The set indicated with A has been treated with the PBS, while the set B with transport medium. The A set clearly illustrates a higher number of dead cells, while the B set suggests that transport medium assists the maintenance of the live cells, and therefore it will be used for the rest of the study.

3.3 Obtaining the geometrical properties of fresh porcine femoral arteries to use as input data for the computational simulations.

The computational model to follow was based on the physiological geometrical and uniaxially obtained mechanical properties (Young's modulus) of the porcine femoral arteries. Three femoral arteries were dissected from porcine legs of three different animals on the same day of slaughtering, which were delivered from a local abattoir. The arteries were kept in transport medium, as described earlier, until testing. Before the tests, the adventitia of each vessel was carefully removed, in order to ease the observation of the change in diameter of the artery. The adventitial layer of the vessels composes of fatty tissue, which basically protects the vessel

from the outer environment, and it doesn't present any further strength to the arterial tissue.

Sample	*t* Meas. 1 (mm)	*t* Meas. 2 (mm)	*t* Meas. 3 (mm)	Average (mm)
1	0.758	0.755	0.755	**0.756**
2	0.751	0.75	0.75	**0.75**
3	0.75	0.75	0.751	**0.75**

Table 3.6: List of the 3 measurements taken for vascular wall thickness using a thickness gauge, and their averaged values.

Sample	*d* Meas. 1 (mm)	*d* Meas. 2 (mm)	*d* Meas. 3 (mm)	Average (mm)
1	5.8	5.78	5.7	**5.75**
2	5.6	5.4	5.8	**5.56**
3	5.5	5.5	5.5	**5.5**

Table 3.7: List of the 3 measurements taken for vascular diameter using a cone shaped gauge, and their averaged values.

Sample	Length under test (mm)	Internal Diameter (mm)	Thickness (mm)
1	29	5.75	0.756
2	30	5.56	0.75
3	40	5.5	0.75
Average	**33**	**5.6**	**0.75**

Table 3.8: List of geometrical properties of the fresh femoral porcine arteries

First, the geometrical properties were determined in terms of the length, thickness, and internal diameter. The length was determined using a simple ruler, the thickness using a thickness gauge and the diameter using a cone shaped gauge. The values of the thickness and diameter of the tissue were noted after averaging 3 measurements. The multiple measurements for these parameters were taken due to the limitations that the above equipment carries. In the case of the pressure gauge, the vessel wall thickness may be pressurised during measurement, and thus provide inaccurate results. Therefore, such measurements, apart from the careful handling,

also require repeatability for more accurate assessment. Similarly, in the case of the cone shape gauge, the tissue may be expanded and increase the vascular diameter. The measurements for the vascular wall thickness are listed in Table 3.6 and for the vascular diameter in Table 3.7. The averaged values, along with the length measurements, where further averaged, in order to be used as geometrical parameters for the development of the 3D computational model to follow (Table 3.8).

3.4 Experimental procedure for the investigation of the strain in the vascular wall under static pressure.

The pressure test was carried out next, in order to determine the dilation of the vascular wall under controlled pressure. The apparatus for this test is described in Figure 3.2. For the pressure test, each artery was mounted on the rig and was fixed on both ends (Figure 3.3).

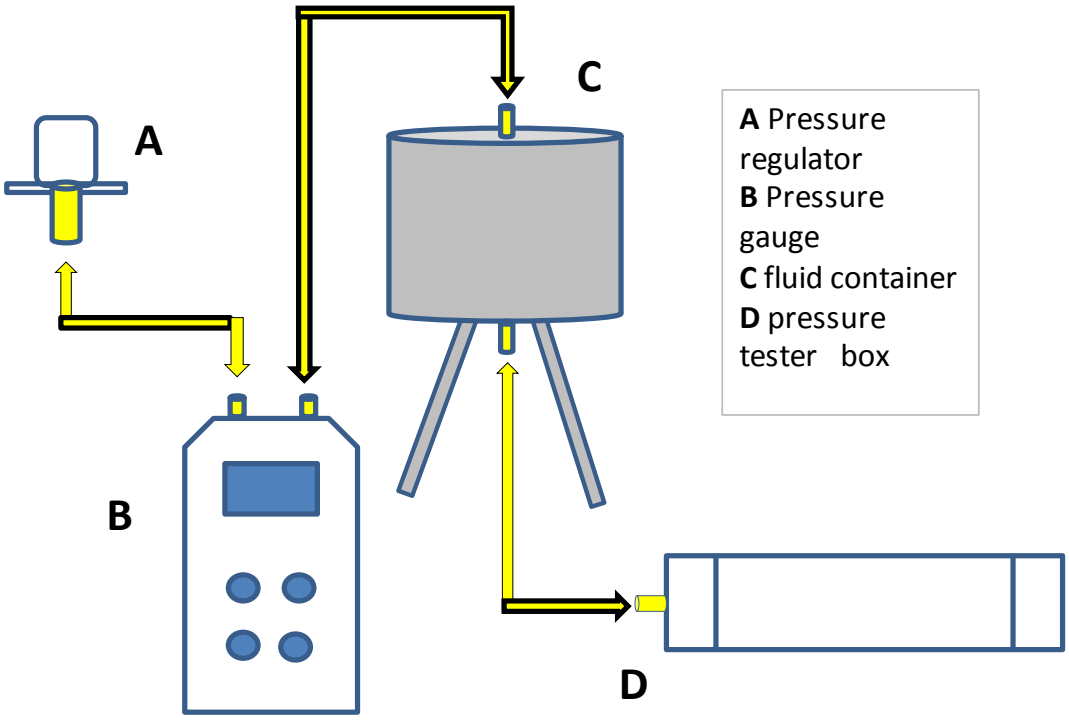

Figure3.2: Schematic of the apparatus used for the pressure test. This involved a pressure regulator (A) connected to a pressure gauge (B) in order to provide indication of the applied pressure. The gauge was then connected to a fluid tank (C) where PBS was flowing to the tester box (D), where the artery was mounted.

Figure 3.3: Illustration of the artery mounting on the pressure rig. The artery was fixed on both ends, using sutures and cable ties on specially designed stainless-steel barbs with a bore of 2mm to allow water to pass through. The white block at the left of this image is solid, and since fluid cannot go through, it allows the dilation of the artery.

Static pressure was applied to a container filled with PBS to pass through the artery, in order to cause its dilation. The pressure was applied using the pressure regulator and a pressure gauge, and was statically increased from 0 to approximately 120mmHg. Under physiological conditions, the pressure ranges between 80-120mmHg, where the properties of the material remain linear elastic. Beyond this limit the vascular tissue presents viscoelastic properties, as previously demonstrated in Chapter 2 (Figure 2.17). However, the purpose of this research was to investigate the strain under physiological conditions, and thus, no further pressure was applied. A camera was placed on the top of the rig on a fixed base and images were taken approximately every 10mmHg. The time-step for image capture and the increase in the pressure was between 1-2 seconds. Since the time-step was so small, no time dependent effects were taken in account during testing.

The images taken using the camera were processed in Photoshop. A triangular ruler was used during testing, placed under the artery (Figure 3.3) and was used as a length gauge in the image (setting a certain length into pixels). Using these features, the dilation was interpreted as the change in diameter of the artery

and was measured approximately in the middle, within a premarked space of a few millimetres wide. The results were then transferred to an Excel spreadsheet for further post-processing. The dilation percentage was then calculated according to equation $\%dilation = [(d_1-d_0)/d_0]*100$, where d_1=extended diameter and d_0=initial diameter. The results were plotted and are demonstrated in Figure 3.4.

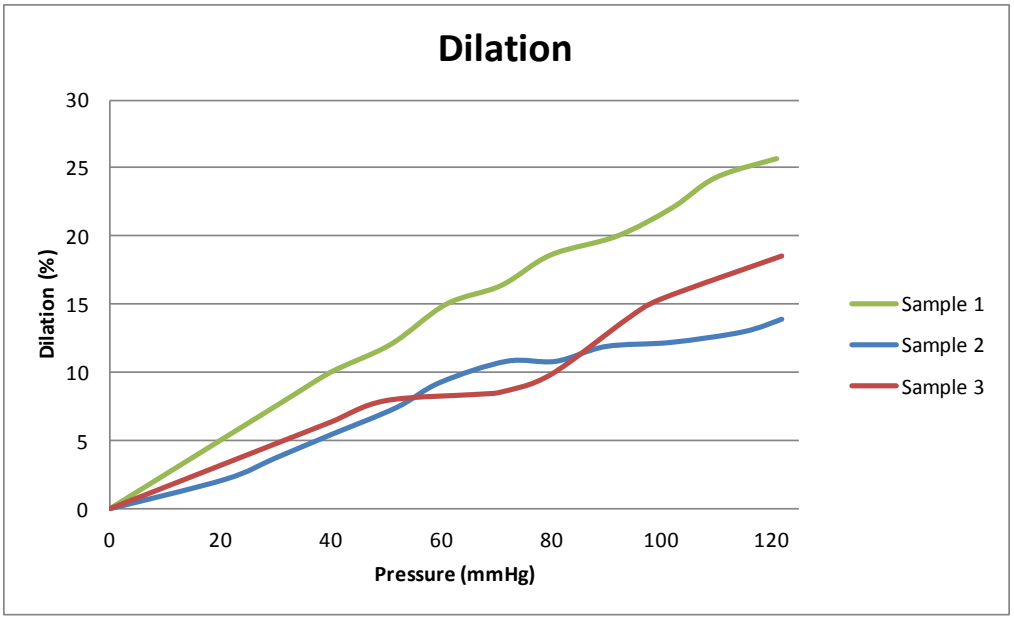

Figure 3.4: The dilation percentage of the three samples, as calculated after pressure test.

3.5 Description of the uniaxial tensile test

Following, each artery was dissected along the circumferential direction using a cutter with a 3mm width, as illustrated in Figure 3.5. The specimens were then mounted on a holder again along circumferential direction according to the protocol, with a fixed height of 6mm. The holder was then mounted on Instron (50N) and the test was performed in PBS at a rate of 10mm/m to failure. A preloading of 0.02N was applied for extra accuracy.

The recorded load/extension data is shown in Figure 3.6. This data was then post-processed in Excel to define the stress/strain relation (Figure 3.7), using the equations: $\sigma=F/A$ *and* $\varepsilon=L_1/(L_0+L_{0.02})$, where F was the recorded force, A the un-deformed cross-sectional area of the specimen, $L1$ the extension of the specimen, L_0 the initial gauge length of the specimen, and $L_{0.02}$ the extension of the specimen required to reach the preloading condition of 0.02 N.

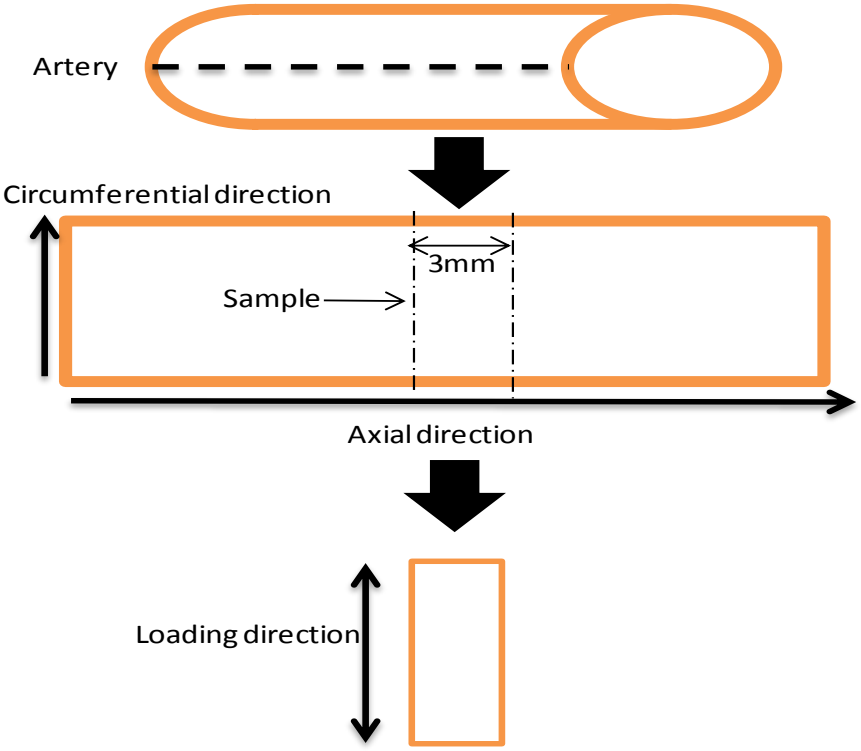

Figure 3.5: Schematic of the dissection process for sample extraction and loading test direction.

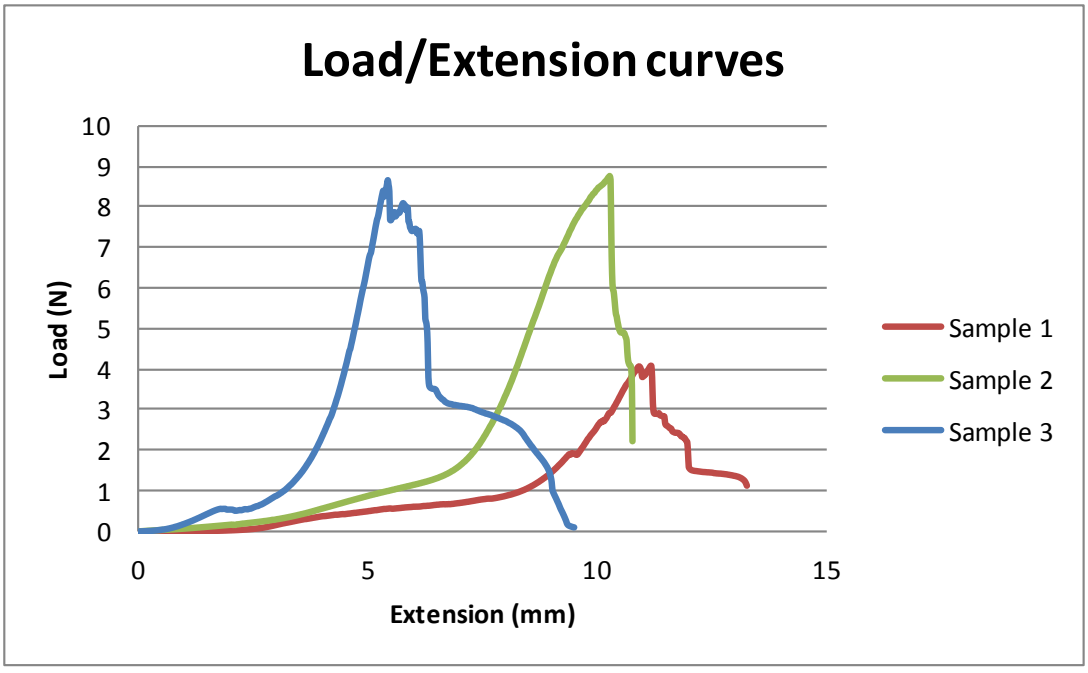

Figure 3.6: Plots for the load/extension curves obtained from uniaxial tensile test and processed in Excel.

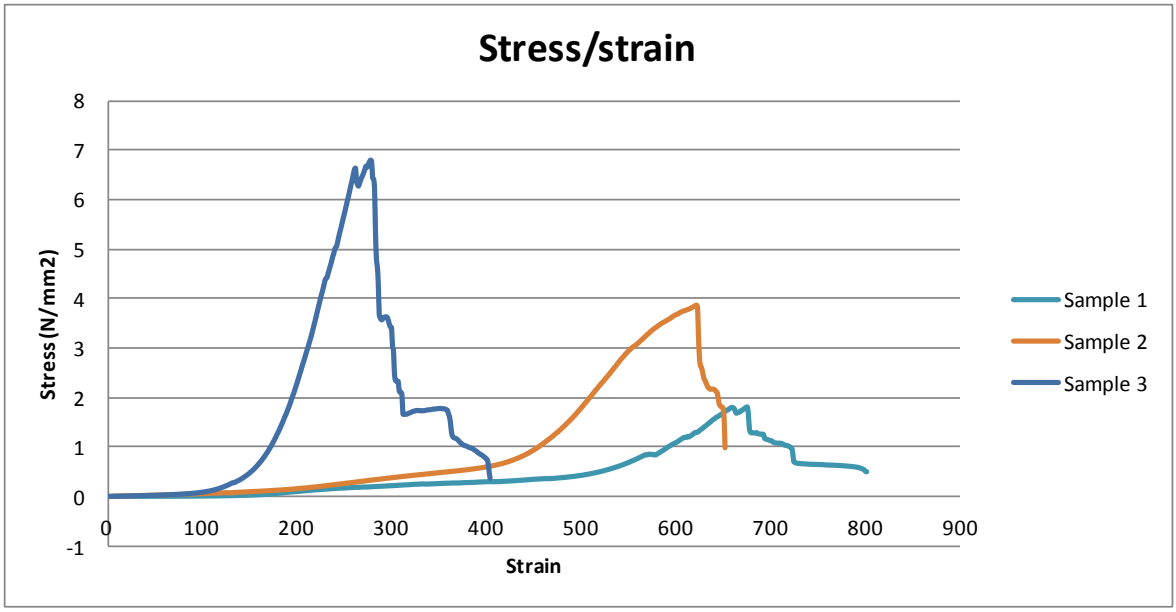

Figure 3.7: Plots for the stress/strain curves as calculated in Excel from the load/extension data.

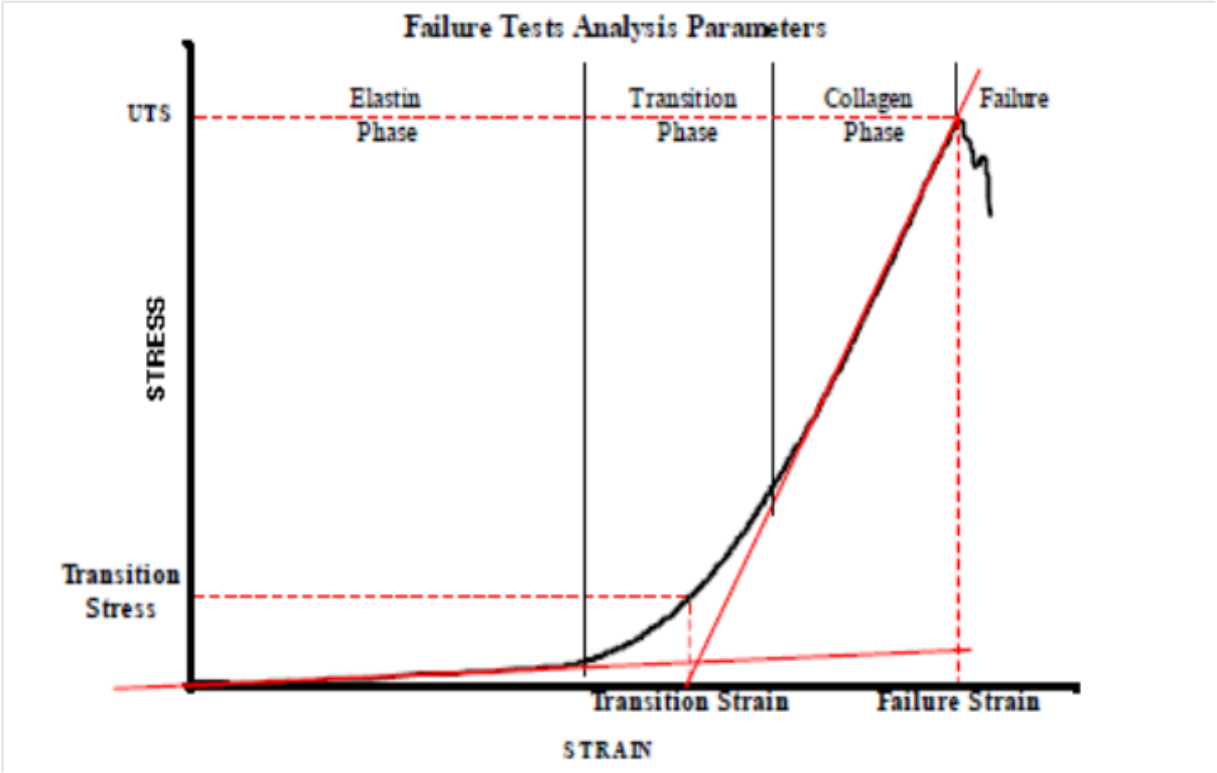

Figure 3.8: Typical stress/strain curve of soft tissue specimen subject to uniaxial loading until failure (Korossis, 2002). The curve is divided in three phases, the elastin phase, the transition phase and the collagen phase. During the elastin phase, the tissue is considered linear elastic, while as it enters the transition phase it exhibits non-linear behaviour, which continues within the collagen phase until failure.

As shown in Figure 3.8, a typical stress/strain graph of a soft tissue may be divided in three phases. The first phase is the elastin phase, where the tissue retains a linear elastic behaviour. This phase is rarely exceeded under physiological pressure (up to 120mmHg). Beyond this pressure, the material enters the transition phase, where it presents non-linear properties, ending to the final collagen phase and eventually to failure. Therefore, the area of interest for the present research is the elastin phase. The Young's modulus of this phase (elastic Young's modulus) was calculated by Excel, using the trendline option, giving the elastin phase slope. The obtained values are shown in Figure 3.9, along with the average value (error bar 95% CI.).

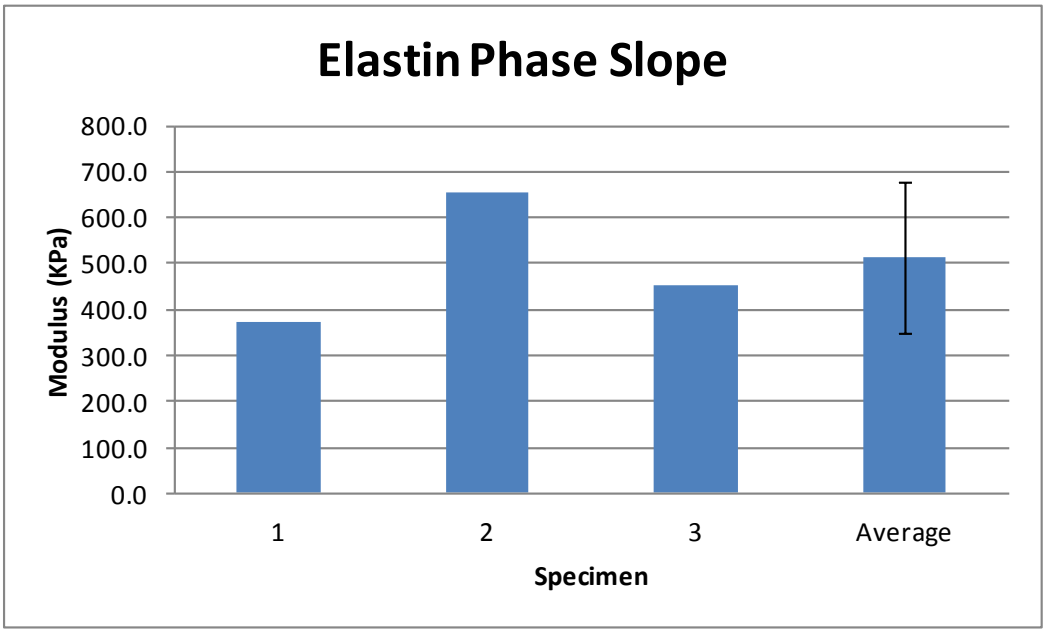

Figure 3.9: The elastin phase slope for the three samples, as calculated after uniaxial tensile test. The average of the three was used as input mechanical properties for the computational model.

3.6 Discussion

Three porcine femoral arteries were dissected from the legs of different freshly slaughtered animals. The number of the samples was kept low, in order to prevent any further animal killing, since the local abattoir had to slaughter a new animal for every fresh tissue order. The arteries were tested in terms of their properties (geometrical and mechanical), in order to be used as input parameters for

the computational simulations. In terms of the geometrical structure, the findings do not seem very different from one animal to the other (Table 3.1-3.3), however, there is a variation in their dilation (Figure 3.4).

The minimum dilation was noticed in sample 2 (~13%), and the highest in sample 1 (~25%), giving a difference of nearly 50%. On one hand, there is a limitation, concerning the accuracy of the image post-processing, that is the dilation results were based on manual measurements, but on the other hand, they do match with the uniaxial test results. The moduli determined by this test (Figure 3.9) are proportional to the dilation of each specimen. Specimen 1 has the minimum reported modulus, and thus, it gives the highest dilation, while specimen 2 with the highest modulus gave the smallest dilation. The difference in the moduli between specimen 1 and 2 (~370KPa and ~650KPa, respectively) is also high, justifying the behaviour of the samples under pressure testing.

Additionally, the samples were dissected from animals from the same abattoir. This means that the age and the nutrition of these animals are similar and should not be considered as effective parameters to the variation of the tissue properties. Therefore, the variation between the present findings is probably related to the quantity and/or quality of the tissue components, collagen and elastin.

Furthermore, it should also be noted that the pressure test carried out in this study does not represent a physiological condition, since the arteries under examination were fixed at both ends. The blood vessels inside the body apart from the dilation, they also expand longitudinally due to the pressure they experience. However, the longitudinal expansion of the arteries in the present study was restricted. Therefore, the applied load forced the arterial wall to perform a larger dilation. Additionally, the pressure was applied gradually and not instantaneously. Despite the small time-step (1-2 seconds), it took over 20 seconds for the pressure to increase from 0 up to 120mmHg. Thus, the constant applied pressure may have led to the increase of the strain (creep). This may also have contributed to an overestimation of the performed dilation.

Unfortunately, and under the best knowledge of the present author, the dilation of porcine femoral arteries has not been reported in the literature, and thus, the present results cannot be directly compared to similar investigations. However, previous studies have reported on similar properties on human femoral arteries. In

1972, Mozersky et al investigated the dilation and the elastic Young's modulus in humans of different age groups, all free from atherosclerosis. The dilation and the Young's modulus were calculated according to the recorded change in the external diameter, by echo-tracking. The results for the dilation were calculated as 2.6% for the young group (<35years), 1.9% for the middle-aged group (35-60years) and 1.7% for people over 60. The elastic Young's modulus was calculated as 260KPa, 388KPa and 628KPa for the same groups respectively. These reported values are much smaller than the ones obtained in the present study, however there is a number of limitations with the method described by Mozersky et al. Initially, the accuracy of the echo-tracking system in 1970's is questionable. Additionally, the measurements involved the external diameter of the arteries. The arteries *in situ* include the outer layer, which composes mostly of fatty tissue that serves to protect the arterial wall from the external environment. This layer was removed in the present study, in order to ease the measurements of the diameter change. In the study of Mozersky et al, the adventitial layer may have significantly underestimated the change in the actual diameter of the tissue.

More recently, in 2004, Kaiser et al investigated several parameters in brachial and coronary arteries in humans with vascular erectile dysfunction, but free from vascular disease. The results included the compliance of these arteries, which was calculated by the change in diameter and change in pressure. The measurements for the diameter change were taken by wall-tracking system with an ultrasound transducer. To facilitate the comparison between the results of the present study and the findings reported by Kaiser et al, the compliance was further calculated as $\frac{\Delta A}{\Delta P}$, where *A* is the cross sectional area of the artery and *P* is the applied pressure. The values for compliance of the present study and compliance of brachial artery reported by Kaiser et al are presented in Table 3.9.

Artery	Sample 1	Sample 2	Sample 3	Brachial (Kaiser et al 2004)
Compliance (mm^2/mmHg)	0.11	0.05	0.15	0.094

Table 3.9: Comparison of compliance between present findings and the ones reported by Kaiser *et al* 2004 for brachial arteries.

The brachial artery was chosen for comparison because it is of a similar size as the femoral arteries, and also they distant equally from the heart, therefore the pressure range is also similar. The values for compliance obtained for Samples 1, 2 and 3 give an average of 0.1±0.05 mm^2/mmHg. This comes in good agreement with the results reported by Kaiser et al.

Finally, in 2008, Roy et al developed FSI computational models based on previously reported parameters on femoral arteries of dogs. The computational results for artery compliance were compared to the findings of Megerman et al. (1986), which involved measurements *in vivo* and *ex vivo*. Unfortunately, this publication is no longer available and the methodology they followed is not described in detail, however the reported values for arterial compliance are listed in Table 3. 10. The reported values involved the compliance of the arteries within the pressure range 80-120mmHg. Again, in order to ease the comparison between results, the calculation for the compliance percentage for the Samples 1, 2 and 3 was given by$\frac{\mathrm{Dd}}{\mathrm{d}*\mathrm{DP}}$, where *d* is the external diameter and *P* the applied pressure. The average value of the samples presented in this study for compliance % is 0.28%±0.05. This also seems to be a good agreement between present and previously reported findings.

Artery	Sample 1	Sample 2	Sample 3	Dog femoral (Megerman 1986)
Compliance %	0.3	0.14	0.4	0.24-0.13

Table 3. 10: Comparison of compliance% between present findings and the ones reported by Megerman *et al* (1986) for femoral arteries of dogs

Concluding, the findings of the present investigation seem to be in a good agreement with similar findings that have been previously reported. Additionally, the findings from the pressure test seem in a good agreement with the uniaxial tensile test results, in terms of stiffness and dilation of the samples. Therefore, the geometrical and mechanical parameters obtained from the above experimental procedure (length, thickness, diameter, elastin Young's modulus) were averaged, in order to provide one value that will be used as input data in the computational model

to follow. The data obtained from the dilation test will also be further used for comparison with the computational findings for validation purposes.

Chapter 4. Investigation of the dilation of the arterial wall, using porcine femoral artery: Computational approach

4.1 Introduction

The aim of the work described in this chapter was to develop *in silico* platforms, with an ultimate purpose to extract information that cannot be obtained experimentally, such as the stress. The information on the stress levels on the arterial wall is of high importance, since the cellular proper function depends on them, and thus they can brought forward to optimise bioreactor conditioning for the development of TE vascular grafts. However, at this point the present investigation focuses on the development and the accuracy assessment of the computational models and it is beyond the scope of this project to present all the parameters that the computational simulations may provide.

Therefore, the following text describes the process development of the FSI computational models, based on the experimental data that were previously obtained (as described in Chapter 3). This data involved the geometrical (length, thickness, diameter) and the uniaxial mechanical parameters (elastin Young's modulus) of the porcine femoral arteries. The mechanical parameters for the fluid (density and viscosity) were taken from the literature. The first model was developed in order to simulate the experimental pressure test from Chapter 3. The purpose of this simulation was to obtain comparable findings between experimental and computational results, in terms of the arterial dilation under static pressure. This comparison was used towards the validation of the computational simulation. Additionally, verification of the computational simulation involved comparison between computational and analytical solutions for axial and circumferential stress. This process is necessary, in order to estimate whether the computational model can be used for further investigation. Further investigation in the present study involved the development of the same models, in terms of geometrical and mechanical parameters, however different pressure conditions. The purpose for this was to

approach more physiological conditions, by using pulsatile flow effects instead of static, as in the first model, within the physiological range (80-120mmHg).

This chapter describes the FSI computational simulations that were developed in order to investigate the dilation of the arterial wall under static and pulsatile flow. The simulations were developed and run using the commercial software Ls-Dyna.

4.2 Computational FSI: Mathematical Background

The commercial software that was chosen for the present investigation (Ls-Dyna) specialises on the FSI using the fully coupled method, that is the simultaneous simulation of both fluid and solid mesh. This method uses one of the parts as the master part and the other one as the slave part. In this case, the master part was the fluid, while the slave part was the solid. This was chosen because the deformation of the elastic solid is realised due to the pulsatile fluid flow, and thus, depending on it.

The governing equations for an incompressible fluid flow involve the continuity equation (Equation 1), as well as the Navier-Stokes (Equation 2):

$$\nabla \cdot \vec{u} = 0 \tag{1}$$

$$\rho\left[\frac{\partial \vec{u}}{\partial t} + (\vec{u} \cdot \nabla)\vec{u}\right] = -\nabla p + \mu \nabla^2 \vec{u} \tag{2}$$

where $\vec{u}$ is the velocity vector, ρ is the fluid density, p is pressure and μ is the viscosity. The chosen software allows the FSI simulation between the structure and the fluid, by employing the ALE formulation. In fluid dynamics, fluid flow through a fixed boundary includes the Eulerian description of the convective term. However, when any part of the computational domain is deformable, this description is no longer applicable and the Lagrangian description must be employed [Hron and Madlik, 2007]. Anywhere else in the fluid domain, the fluid flow can be described in an arbitrary coordinate system as long as it meets the coordinate requirements along the physical boundaries. This description is called an Arbitrary Lagrangian-Eulerian formulation (ALE). For this description, the convective velocity in the Navier-Stokes equation (Equation 2), is replaced by its difference with the moving coordinate velocity $\vec{u}_m$ as in Equation 3:

$$\rho\left[\frac{\partial \vec{u}}{\partial t}+\left((\vec{u}-\vec{u}_m)\cdot\nabla\right)\vec{u}\right]=-\nabla p+\mu\nabla^2\vec{u} \quad (3)$$

Moreover, it is obvious that when $\vec{u}_m=0$, Equation 3 corresponds to an Eulerian description, while when $\vec{u}_m=\vec{u}$, it corresponds to the Lagrangian (Figure 4.1).

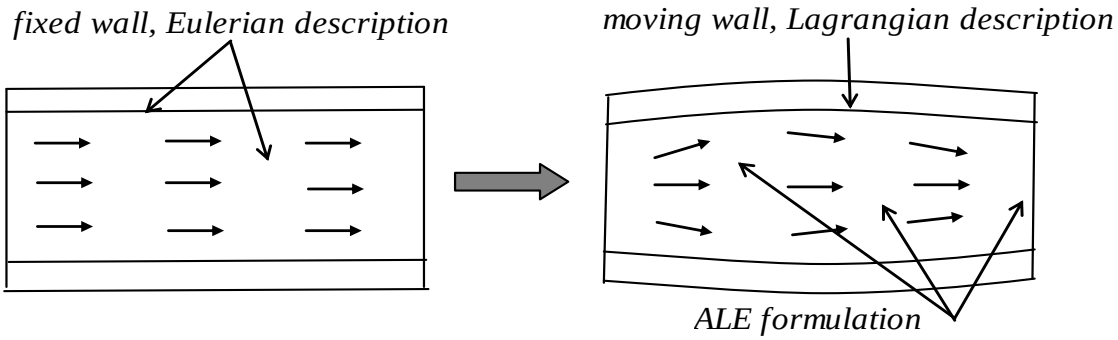

Figure 4.1: Schematic of mathematical formulation for fixed and moving boundaries. The Eulerian description applies to the fixed wall, while the Lagrangian to a moving boundary. When combined together, Arbitrary Lagrangian-Eulerian formulation, apply to the movement of the fluid, when this follows the moving boundary.

4.3 Construction of the computational models

The computational simulation involved the construction of a 3-dimensional model representing the blood flowing within a vessel. The blood was modelled as a cylinder, following the averaged geometrical properties as they were previously determined (Chapter 3), with a length of 33mm and 5.6mm diameter. All the parameters used for fluid and solid are listed in Table 4.1. The actual meshed geometries are shown in Figure 4.2 The fluid, it was set as incompressible (density ρ=1050kg/m^3) and Newtonian (viscosity μ=0.00345kg/m s). The vessel was modelled as a shell, because of its small thickness (0.74mm) and as a linear elastic material with a Young's modulus *E*=493.6KPa. The linear elastic material that was used by the software, obeys Hooke's law that implies a linear proportion between stress and strain. Both ends of the model were set to be fixed, in order to constrain movement and also to allow comparison with the experimental pressure test for validation purposes. The no-slip condition was also imposed at the inner wall surface.

The simulation was run under the Arbitrary Lagrangian-Eulerian (ALE) condition, using different pressure waveforms. The first pressure condition was linear starting from 0 up to 120mmHg, which represented the case of the experimental

pressure test. The second pressure condition was a simplified pulse starting from 80mmHg and reaching 120mmHg within 0.5 seconds. However because of the output results of this model, another simulation was run with the same pulse, this time starting from 0mmHg. Nevertheless, in a physiological case, the pressure never reaches 0, thus one more simulation was run with a double pulse, which initially starts from 0mmHg but then it continues from 80mmHg. The pressure conditions can be seen in Figure 4.3. All the models are listed in Table 4.2.

Fluid	**Value**	**Ref.**
density	1050kg/m^3	[Scotti&Finol 2007]
viscosity	0.00345kg/m s	
Solid		
length	33mm	Data obtained from experimental work in Chapter 3
diameter	5.6mm	
thickness	0.75mm	
Young's modulus	493.6KPa	

Table 4. 2: The geometrical and mechanical properties that were used to develop the 3D FSI computational models.

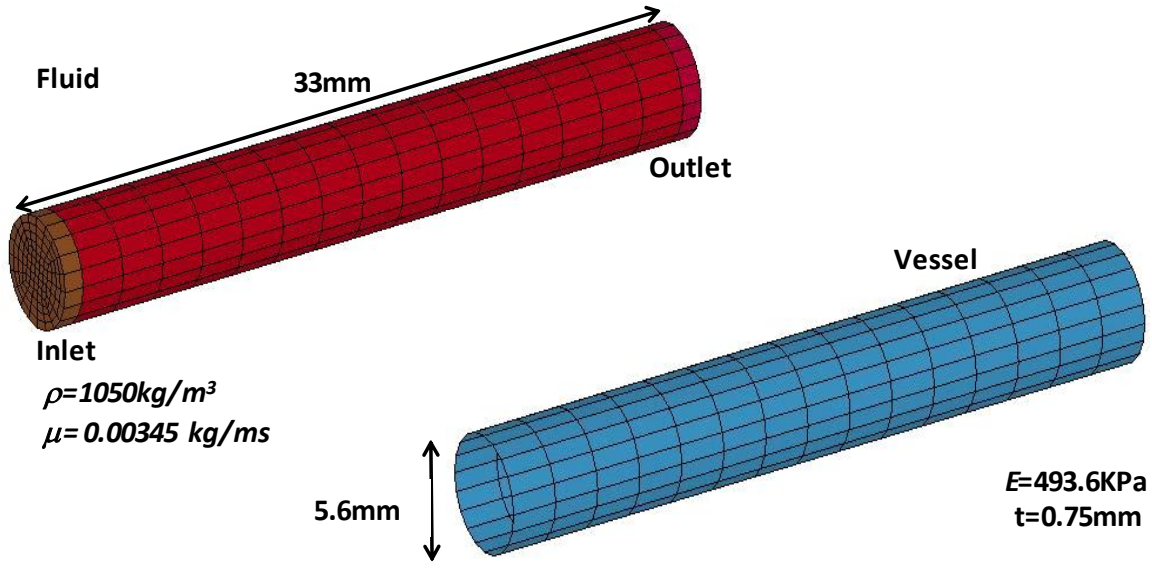

Figure 4.2: Demonstration of the mesh created to represent the blood and the arterial wall.

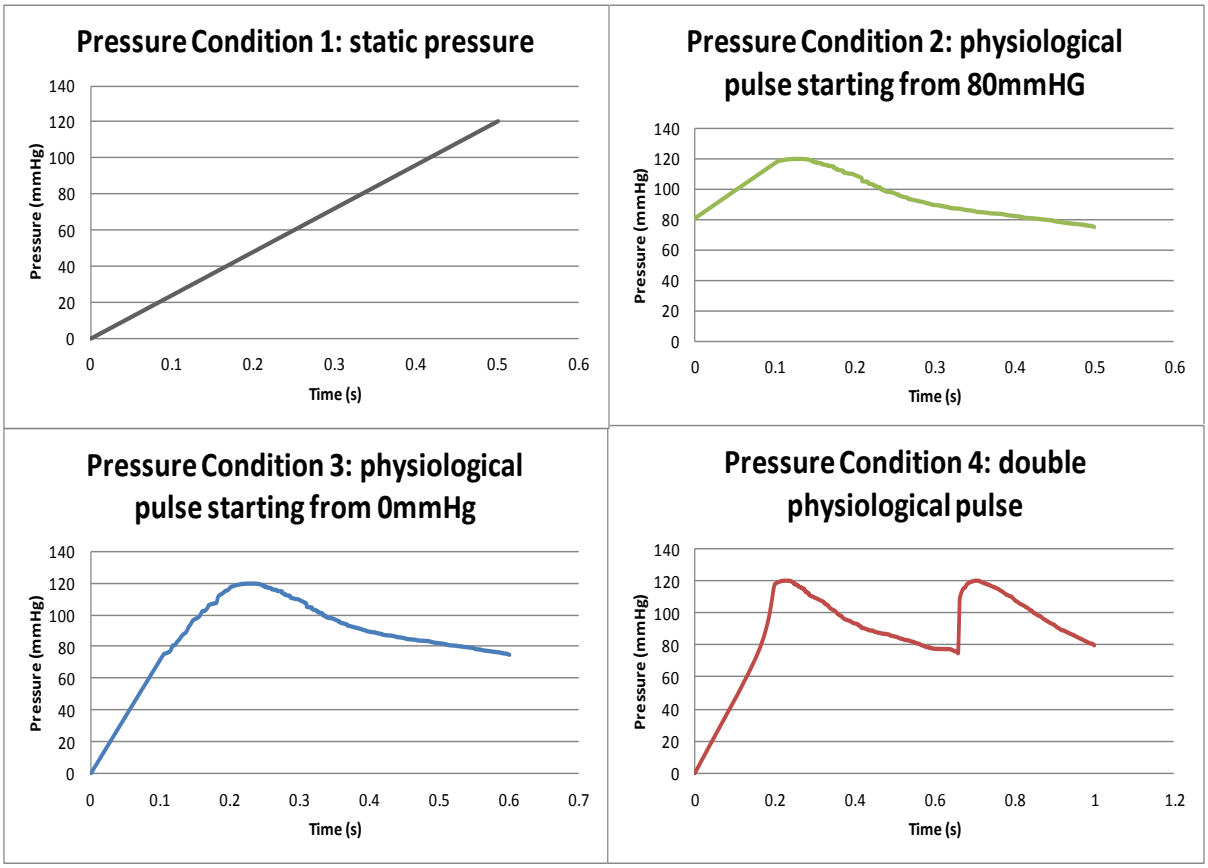

Figure 4.3: Pressure waveforms that were used as input conditions for the numerical simulations. Condition 1 represents a static pressure starting from 0mmHg up to 120mmHg. Condition 2 describes a physiological pulse starting from 80mmHg up to 120mmHg. Condition 3 describes a physiological pulse starting from 0mmHg and gradually develops up to 120mmHg. Condition 4 represents a double physiological pulse as it continues from condition 3.

Model	**Pressure Condition**	
	Inlet	**Outlet**
1	1	0
2	2	0
3	3	0
4	4	0
Mesh dependence	1	0

Table 4.2: Description of the pressure conditions application for each of the models.

The models were meshed with 1,260 solid brick elements for the fluid and 200 shell brick elements. A mesh sensitivity test was performed using 80,640 solid and 3,200 shell brick elements.

4.4 Results

4.4.1 Dilation under Static Pressure

The post-processing of the computational analysis involved the dilation percentage of the represented artery. This was calculated in Excel using the formula *[(Y(r_1)-Y(r_0))/ Y(r_0)]*100*, where *Y* represents the y-coordination of a node in the middle of the vascular wall. *Y(r_0)* and *Y(r_1)* represent the node without (no pressure applied) and with (pressure applied) dislocation along the y-axis, respectively (Figure 4.4).

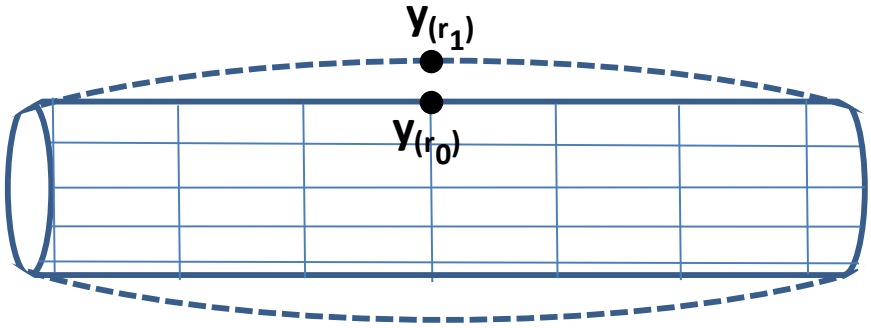

Figure 4.4: Schematic of the nodal coordinate, which was used to calculate the dilation percentage from the computational simulation.

Images for y-coordination contours are illustrated in Figure 4.5 for model 1 in different time intervals, including the last one (at time *t=0.5s*) where the maximum pressure was reached (120mmHg). The results from this model were compared to the ones with the finer mesh model, in order to check on the mesh sensitivity. These are demonstrated in Figure 4.6. At maximum pressure (p=120mmHg), the dilation (strain) percentage is approximately ~11%, while the one from the model with the finer mesh ~11.2%. Because of the small difference between the results of these two models, in order to reduce the computational cost, the remaining simulations were run using the same mesh as in Model 1.

The dilation results from Model 1 were further compared to the experimental findings that were described in the previous chapter. The overall dilation of the three experimental samples and the one given from Model 1 are plotted in Figure 4.7, while the maximum values (at pressure *p=120mmHg*) in Figure 4.8 along with the average of the experimental findings (95% C.I.).

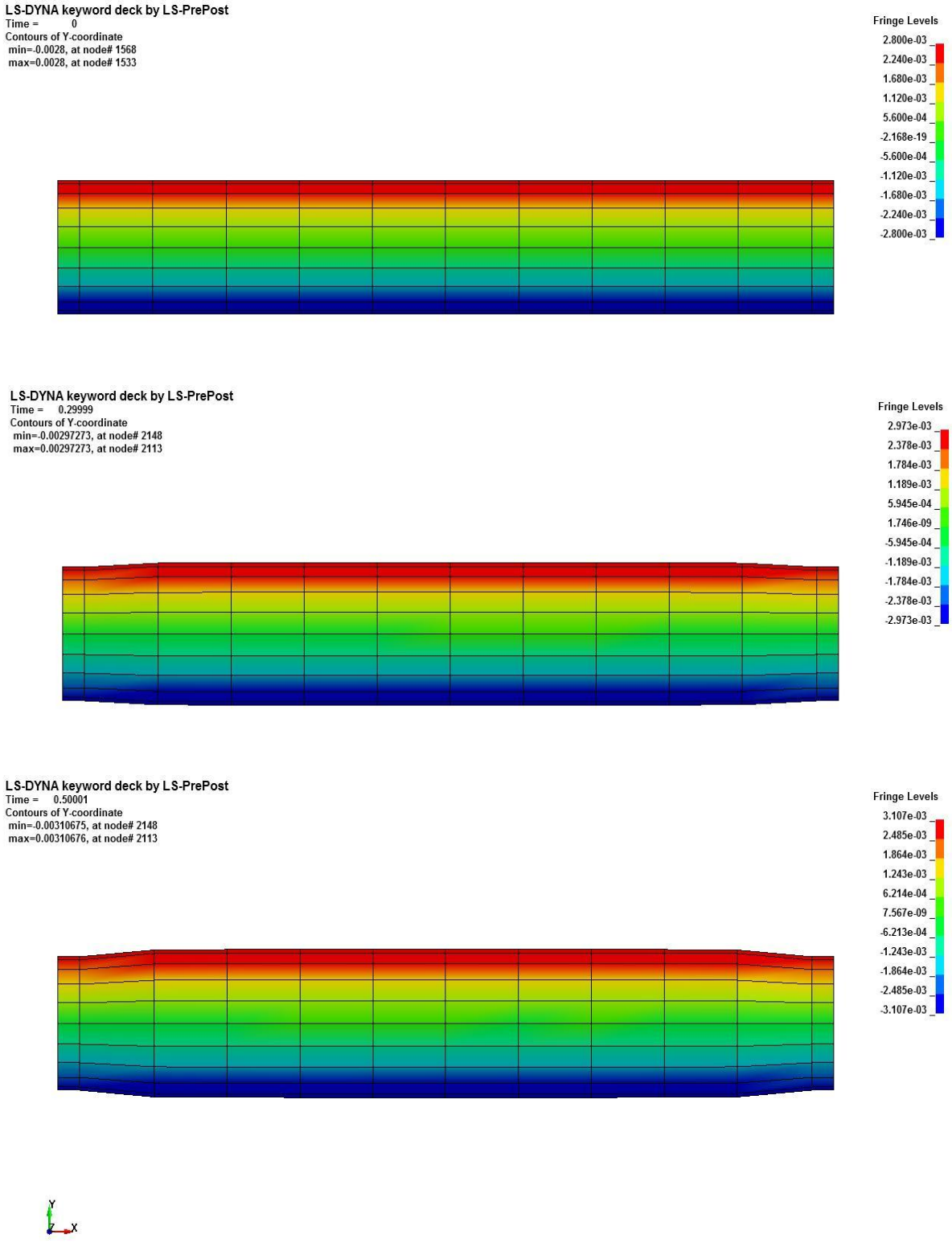

Figure 4.5: Contours of y-coordinate of the arterial wall for Model 1. Static pressure was gradually increased from 0mmHg up to 120mmHg, forcing the wall to dilate.

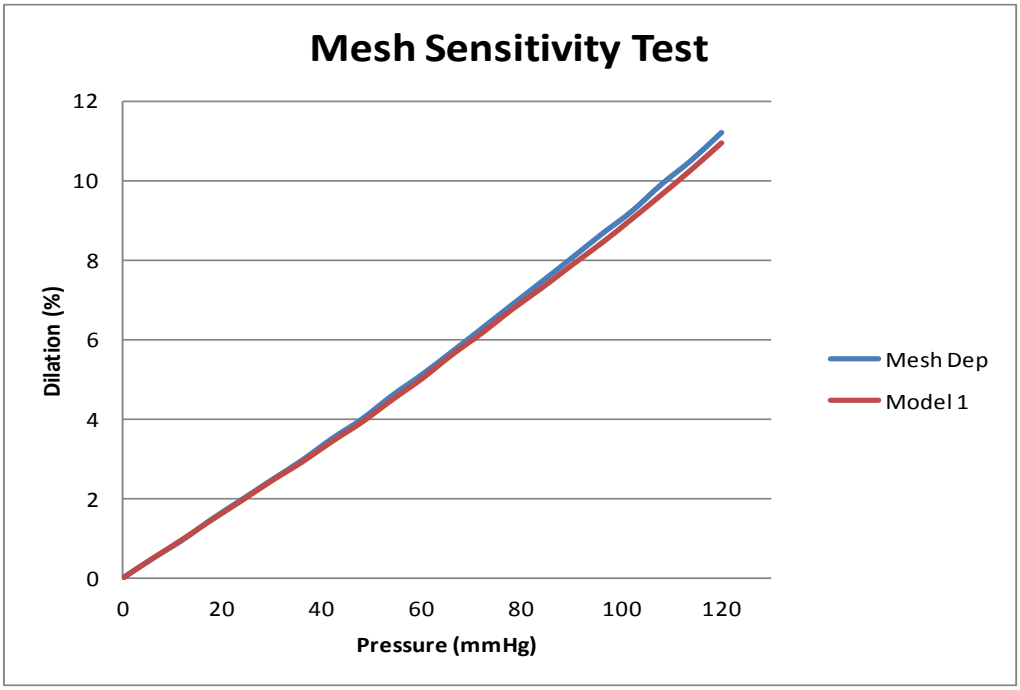

Figure 4.6: Mesh sensitivity test. Model 1 was compared with a finer mesh in terms of dilation in order to check on the mesh dependence. The small difference between the results allows the further use of Model 1.

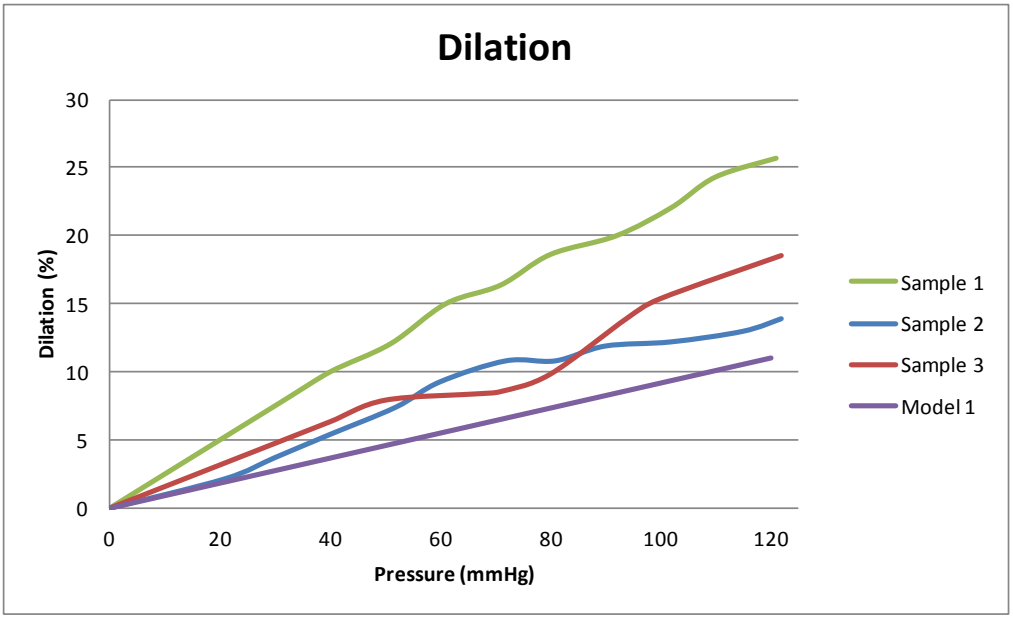

Figure 4.7: Comparison between experimental and computational dilation. Samples 1, 2 and 3 were the samples that were tested experimentally under static pressure, as described in Chapter 3. Model 1 performs a lower dilation compared to the experimental findings.

The computational model performed a much smaller dilation compared to the real arteries, and also, under maximum pressure it does not lie within the confidence interval of the average experimental value. The reason for this is probably because of the mechanical properties that were used for the computational simulation. The Young's modulus that was obtained from the uniaxial test involved the circumferential direction only. The tissue is much stiffer towards this direction, because of the collagen and elastin fibres' orientation.

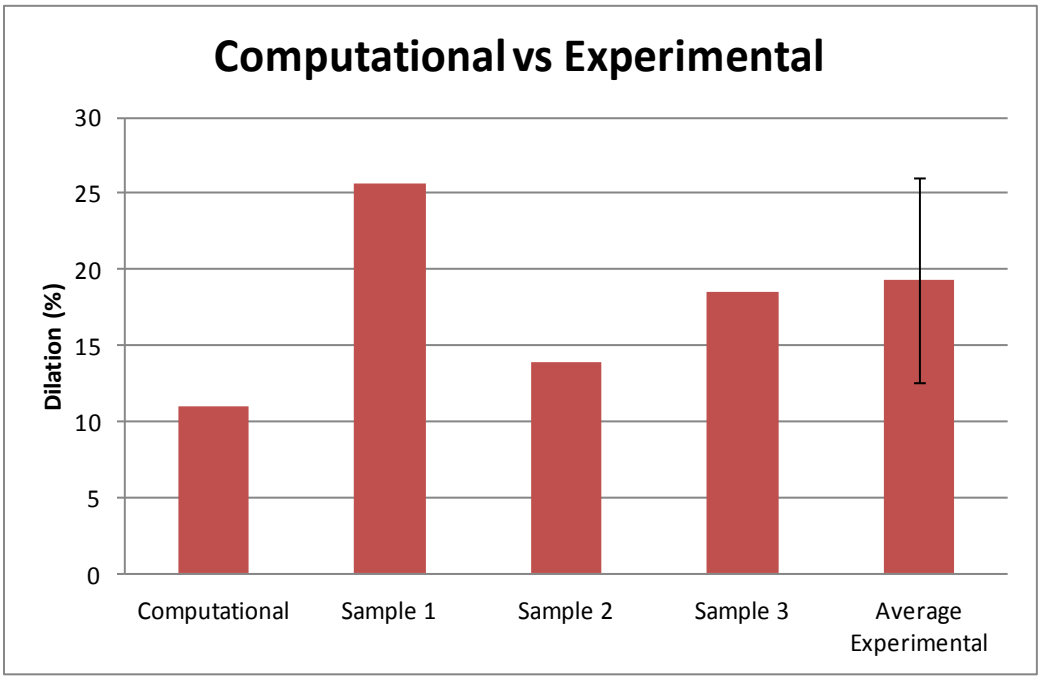

Figure 4.8: Comparison between experimental and computational dilation at highest pressure (120mmHg). The computational solution indicates the smallest dilation compared to the samples 1, 2 and 3. It does not lie within the confidence interval of the error bar (95%) of the average experimental value.

4.4.2 Computational model validation using an analytical solution for axial and circumferential stress.

An analytical solution for the axial and circumferential stress was calculated. The comparison between computational and analytical solutions serves to verify the mathematical process of the computational model. The formula for the axial stress is given as $\sigma = \frac{F}{A}$, where σ is the stress, F is the force applied and A the cross-sectional area of the solid material. This can be analysed as follows:

$$\sigma_{axial} = \frac{F}{A} \rightarrow \frac{p\frac{\pi * d^2}{4}}{\pi * d * t} = \frac{p * d}{4t} \quad (4)$$

where *p* is the internal pressure at inlet, *d* is the internal diameter of the vessel at the respective pressure, and *t* is the thickness of the vessel wall. Substituting the values for each parameter in Equation 4 for pressure *p*=120mmHg:

$$\frac{p * d}{4t} = \frac{16KPa * 6.22mm}{4 * 0.75mm} = 33.1KPa \quad (5)$$

The value of pressure 16KPa (Equation 5) was converted from 120mmHg, in order to meet the right units for the formula. Additionally, the circumferential stress according to Laplace equation may be estimated as:

$$\sigma_{circ} = \frac{p * d}{2t} = \ 66.3KPa \quad (6)$$

The results for the axial and circumferential stress obtained from Model 1 were plotted in Figure 4.9 and 4.10 respectively, and refer to a middle element of the arterial mesh, where dilation was earlier calculated. At pressure *p*=120mmHg, the maximum value for axial stress in Model 1 was noted at *t=0.5s* as σ_{axial}=30KPa, while for circumferential stress σ_{circ}=64.6KPa. Circumferential strain for Model 1 at *p*=120mmHg is 0.177 (Figure 4.11). According to the stress/strain results from the tensile test, the porcine femoral arteries at the same stress value (σ_{circ}≈65KPa) presented a strain of 0.11, 0.28 and 0.15 for Samples 1, 2 and 3, respectively (Figure 4.12). This gives an average of 0.18, which suggests a good agreement between computational, analytical and experimental findings. However, since the findings from the experimental uniaxial test were used as input parameters for the computational simulations, this comparison may only be considered as verification.

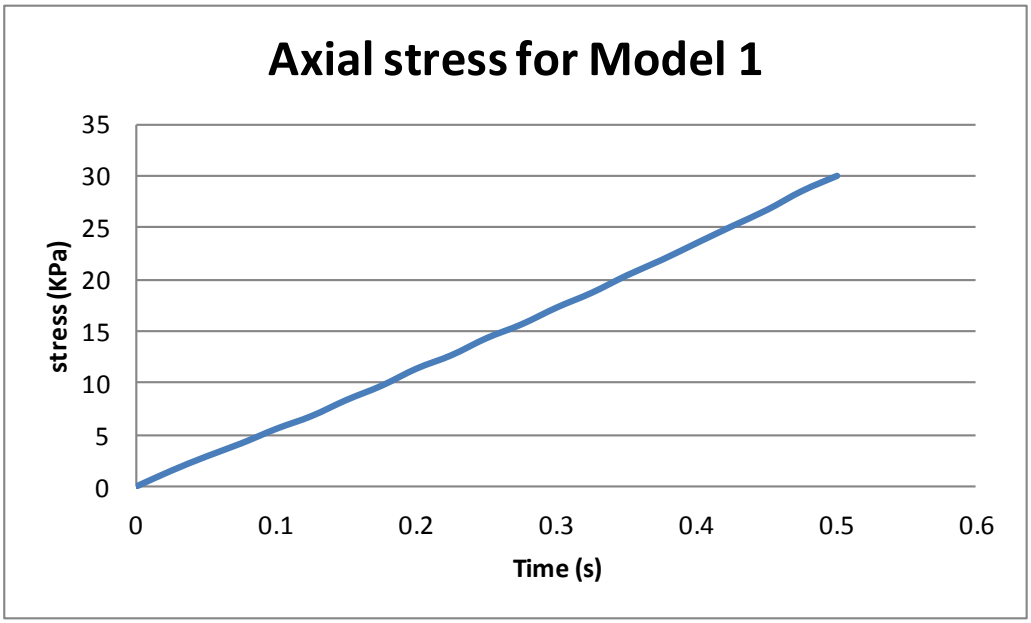

Figure 4.9: Axial stress as resulted from Model 1 simulation.

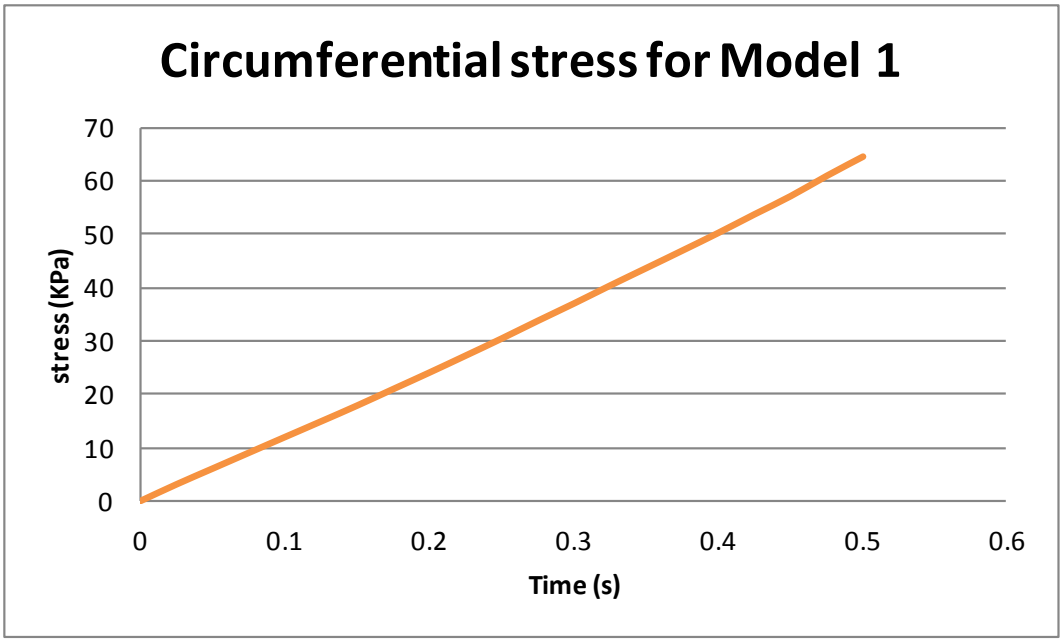

Figure 4.10: Circumferential stress as resulted from Model 1 simulation

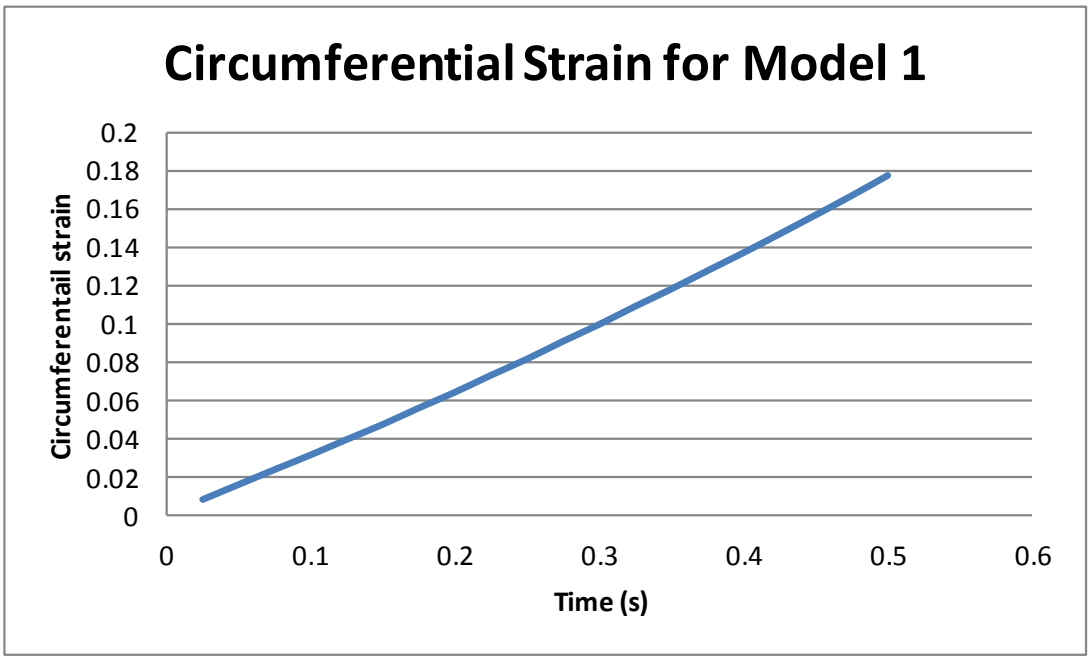

Figure 4.11: Circumferential strain as resulted from Model 1 simulation

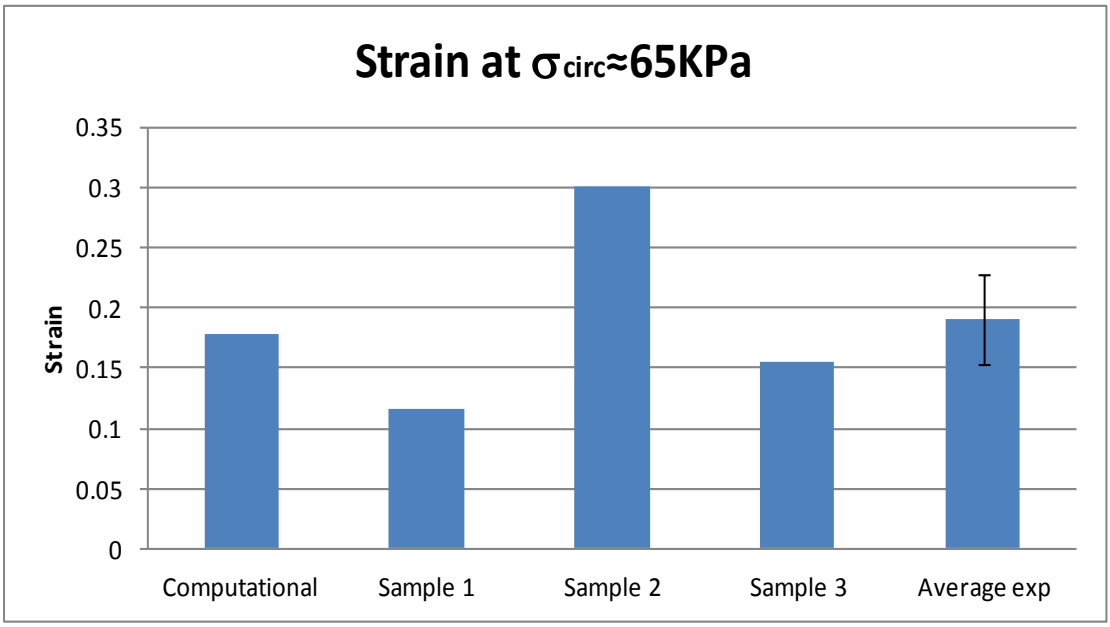

Figure 4.12: Circumferential strain for Model 1 and for the three samples after the uniaxial tensile test at σ_{circ}≈65KPa. The value for circumferential stress rises from the computational stress results at p=120mmHg (where σ_{circ}=64.6KPa. The Average experimental (CI 95%) results in good agreement with the computational result.

4.4.3 Dilation under pulsatile pressure

As previously described, the models 2, 3 and 4 were run under different pulsatile pressure conditions. The results for the dilation were obtained similarly as in the static pressure condition and were plotted in Figure 4.13. For Model 2, the pressure was starting at p=80mmHg, however this caused significant transient effects on the results, probably because of the explicit solver that is used in LS-Dyna. The highly non-linear behaviour of the model does not allow any further post-processing and this is the reason for the creation of the Model 3, where the pulse starts at p=0 and then it develops in a proper pulse by one second of the time. The dilation results from this model came out as a smooth graph that seems to follow the pressure wave with respect to time. For Model 4, the pressure pulse repeated a second cycle, allowing the fluid to develop itself with time. Similarly as in Model 3, the graph is smooth and was also plotted against the pressure wave in Figure 4.14, which indicates that pressure and dilation are in a good agreement. This presented linearity between pressure and dilation was expected, since the vascular wall was modelled as linear elastic. The peak values of the arterial wall dilation are listed in Table 4.3.

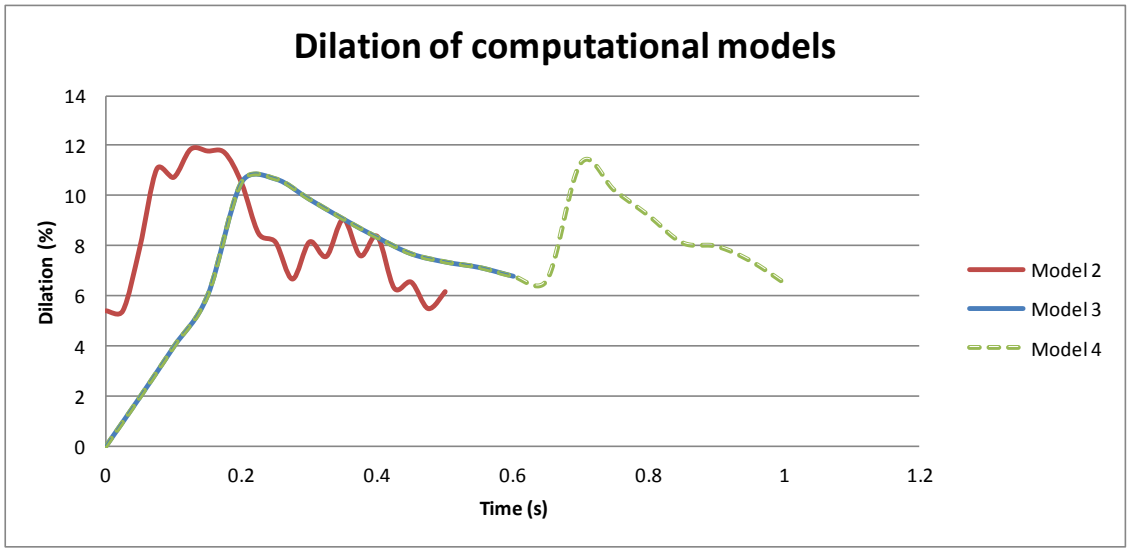

Figure 4.13: The dilation as resulted for Models 2, 3 and 4. Model 2 presents strong transient effects, while Models 3 and 4 look more smooth and reasonable.

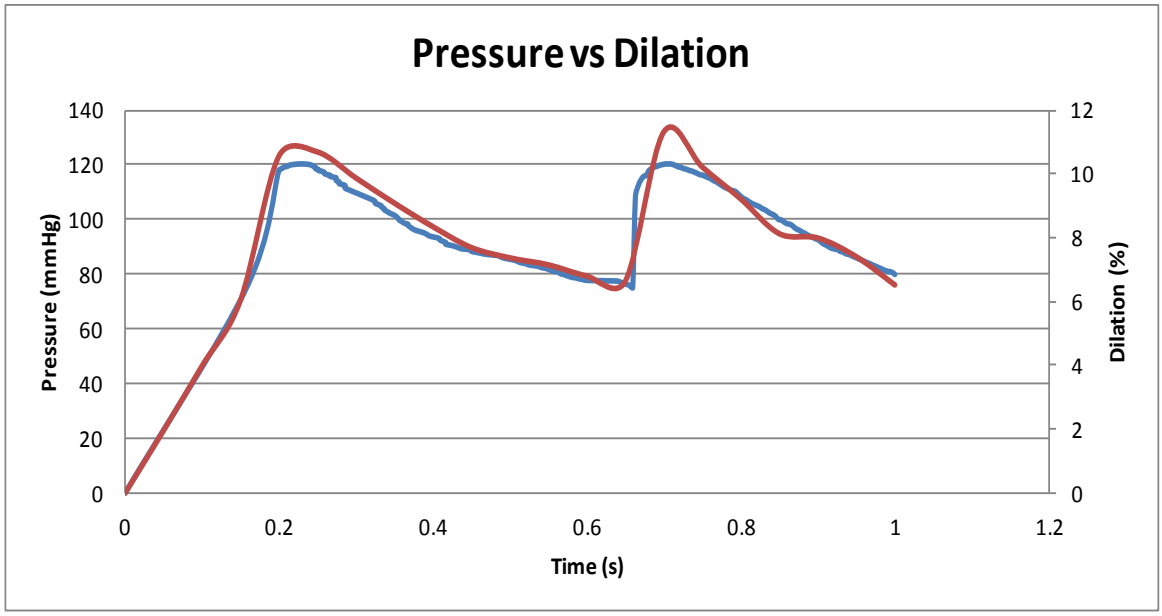

Figure 4.14: Plots of pressure vs. dilation. The dilation performed for Model 4 (red) seems to be in accordance with the pressure wave that was applied in the inlet boundary (blue).

Model	Max Dilation (%)	Time (s)
2	11.9	1.25E-01
3	10.7	2.50E-01
4	11.3	7.00E-01

Table 4.2: Maximum dilation that was noted for Models 2, 3 and 4.

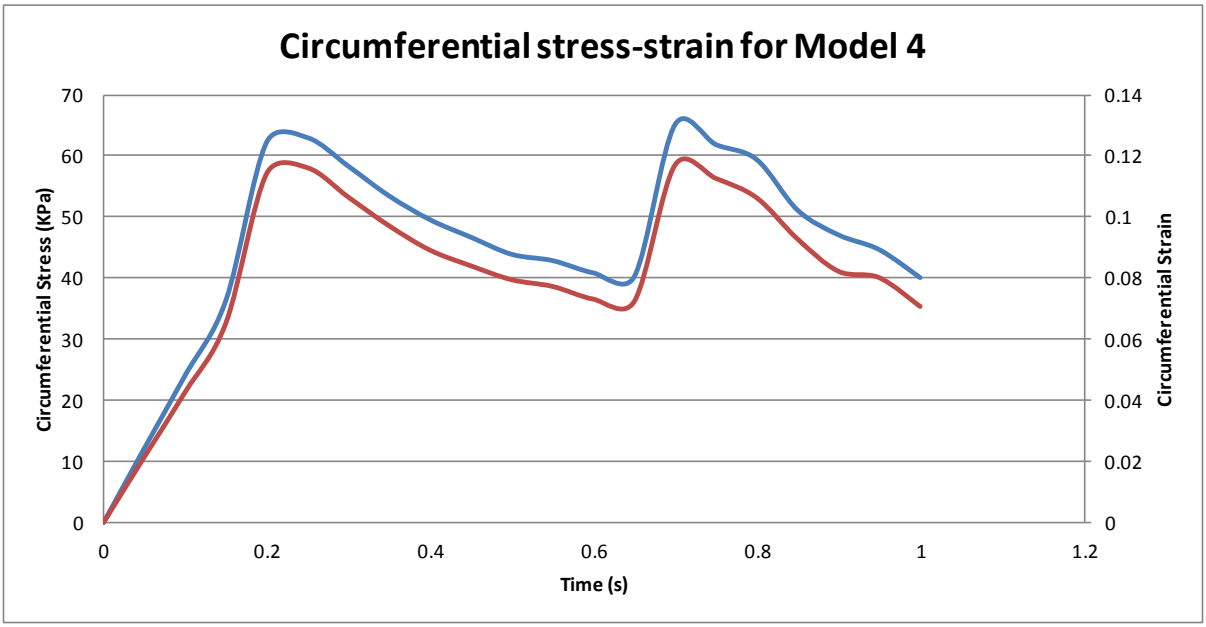

Figure 4.15: Plots of circumferential stress (blue) and strain (red) for Model4.

Model 4 was chosen for further post-processing, because of the two-cycle pressure condition, with the second cycle as the interval of interest. Further post-processing involved the circumferential stress and the circumferential strain (Figure 4.15), which were given at the same node/element, as in the earlier investigation under the static pressure condition. The maximum values for stress and strain were given at t=0.7s, where p=120mmHg during the second cycle, as σ_{circ}=65 KPa and ε_{circ}=0.117. The value of the circumferential strain is slightly lower than the ones obtained from Model 1 and experimental uniaxial test.

4.3 Discussion

The purpose of this work was to develop computational models, which would simulate the behaviour of the arterial wall under blood pressure. The investigation was focused on the dilation of the arterial wall, with the ultimate purpose to assess the strain levels, in order to bring them forward for investigation at the micro-level. Towards this, five computational models were constructed, using the same mesh under different pressure conditions.

The geometry of the mesh was build according to the information obtained experimentally, as described in Chapter 3. This information involved the length of the artery, the thickness, the diameter and the elastic Young's modulus of fresh porcine femoral arteries. As previously explained in Chapter 3, the elastic Young's modulus refers to the slope of the elastin phase of the arterial tissue that was obtained from uniaxial tensile test along the circumferential direction. The tissue properties were examined towards this direction, since the main focus of the present investigation was the dilation that the tissue performs under physiological blood pressure and the longitudinal extension of the tissue was not taken into account. Ideally, the mechanical properties of the arterial wall should be determined biaxially, since the dilation takes place in three dimensions, however, only a uniaxial test was performed, as a matter of availability. Additionally, the single modulus value was used in a linear elastic model, rather than a viscoelastic or any other hyperelastic material that is available from Ls-Dyna, because of the assumption that under a physiological blood pressure (120-80mmHg) the tissue does not exceed its linear phase.

The models were run under different pressure conditions. The first model (Model 1) was run under static pressure and it served to simulate the pressure test that was performed experimentally, as described in Chapter 3, for validation purposes. The comparison between experimental and computational results (Figures 4.7 and 4.8) suggested that the computational model performed a much lower dilation than the real tissue samples. The actual value of the maximum dilation was 11%, while the respective average from the experimental samples was approximately 19±6.7%. However, the analytical solution for the axial and circumferential stress came in a good agreement with the ones obtained computationally, indicating the computational model is mathematically correct. Additionally, the strain values at the calculated stress were also in good agreement between computational and experimental findings (Figure 4.12). This suggests that the reason that the model performed smaller dilation than the experimental findings probably lies on the mechanical properties that were used for the arterial mesh. The modulus that was obtained only along the circumferential direction provides a greater stiffness to the arterial wall, when compared to a more realistic case that would be determined more accurately after biaxial test. Furthermore, as explained in Chapter 3, the dilation during the experimental pressure test was probably overestimated due to creep, and this also provides a reason for the difference between experimental and computational findings.

The rest of the models (Model 2, 3 and 4) were run under pulsatile pressure, as an attempt to simulate more physiological cases. Model 2 was run under a single pressure wave, starting at p=80mmHg up to 120mmHg. The results obtained from his model, though, indicated transient effects (Figure 4.13). The reason for the transient effects is probably due to the explicit solver that Ls-Dyna uses for dynamic analysis. The explicit method solves the equations directly and not iteratively, as the implicit method. This is a good way to solve non-linear problems, however, the explicit method does not enforce equilibrium like the implicit, and thus, may lead to transient effects. For this reason Model 3 was run under the same pressure wave, this time starting at p=0, giving some time for the wave to be developed. The dilation curve that was resulted from Model 3 was smooth with no transient effects, however Model 4 was also run under a double pressure wave, in order to investigate the dilation under a fully developed pulse. The results for peak dilation from Models 3

and 4 are quite close (10.7% for Model 3 and 11.3% for Model 4), and also their average ~11% is the same as the one from Model 1 (Figure 4.8). The results for dilation and circumferential stress and strain for Model 4 suggest that for these parameters, static pressure could be used instead of a pressure wave for further investigation, in order to ease the simplicity and repeatability of the computational simulation and also to reduce the computational expense. However, the pulsatile flow models could be subject to further investigation. This could involve more physiological conditions for pressure/velocity profiles, more complex geometries and of course more realistic mechanical properties for the vascular wall.

Previous similar FSI computational studies on the dilation of femoral arteries have been reported by Kim et al (2008) (human) and Roy et al (2008) (canine). Both studies used the Mooney-Rivlin material instead of a linear elastic. The Mooney-Rivlin material is considered as hyperelastic, with the strain energy density function *W*:

$$W = C_1 (I_1 - 3) + C_2 (I_2 - 3) + C_3 (I_1 - 3)^2 + C_4 (I_1 - 3)(I_2 - 3) + C_5 (I_2 - 3)^2$$

where the constants C_1 -C_5 are obtained by fitting curves from experimental data [Roy *et al* 2008]. Unfortunately, the different data in mechanical properties that were used for those studies do not allow comparison with the ones used in the present investigation, therefore there can be no commentary in the difference in stiffness determined between studies.

In the study of Roy et al (2008), the boundary conditions involved an initial pressure pulse (ranged between 75-140mmHg) at the inlet and another at the outlet, which included the pressure drop that was determined experimentally. The blood flow was modelled as a non-Newtonian, using the Carreau model. The reported outcome results for compliance percentage within a pressure range 80-120mmHg varied between 0.2%-0.145%. The respective results from the present study were between 0.098% for the static pressure model (Model 1) and 0.097% for pulsatile pressure (Model 4). It was previously mentioned (Chapter 3) that the findings from the study of Roy et al (2008) were compared with the ones obtained by Megerman et al (1986). Recalling Table 3. 10 and adding the values from FSI computational models listed in Table 4.3.

Method	Artery	Compliance %
Experimental	Dog femoral (Megerman et al 1986)	0.24-0.13
	Porcine femoral Average (Chapter 3)	0.28±0.05
FSI	Dog femoral (Roy et al 2008)	0.2-0.145
	Model 1	0.098
	Model 4	0.097

Table 4.3: Comparison of compliance% from experimental and FSI studies between present and previous investigations.

The comparison between studies indicate a slightly lower compliance for the FSI models of the present study, still very close. The compliance% for the porcine femoral arteries as found from the pressure test is higher compared to the experimental (Megerman et al 1986) and FSI (Roy et al 2008). The experimental procedure carried out by Megerman et al (1986) is not described in detail, and also the material stiffness used to describe the solid mesh in the study of Roy et al (2008) is not comparable to the present investigation, however the results are still very close. This also indicates that the dilation of the porcine femoral arteries during pressure test was overestimated, and also, the linear elastic material that was used for Model 1 and Model 4, based only on the circumferential elastic modulus, contributed in a smaller dilation.

The FSI models developed by Kim et al. (2008) were based on realistic geometrical data of human femoral bifurcation, which was reconstructed by CT images of a 55 year old female volunteer suffering from paraplegia. The data they used for the Mooney-Rivlin model were taken from the literature [Prendergast et al 2003], which were obtained after uniaxial (longitudinally) and biaxial tensile tests in human femoral arteries. The boundary conditions involved a pressure pulse in the inlet and outlet. The pressure, however, was calculated with the Navier-Stokes equations for one dimensional flow in elastic tube, based on the geometry of the artery and the velocity flow. The velocity flow was obtained experimentally from contrast phase MRI data. This calculation, however, provided a pressure within a range of 0-40mmHg, which is considered low for femoral arteries. The results for the

dilation at peak systole were reported as 5.7% at the section before bifurcation starts and 3.7% at the branching section. The results from the present investigation are reported at *p*=40mmHg, to facilitate comparison to the ones obtained by Kim et al (2008), and are listed in Table 4.4. Again, comparison between FSI models indicates a low dilation for the results of the present study and a large dilation for experimental pressure test.

Method	Artery	Dilation %
Experimental	Porcine femoral Average (Chapter 3)	7.2±2.7
FSI	Human femoral (Kim et al 2008)	5.7 (Section 1) 3.7 (Section 2)
	Model 1	2
	Model 4	1.98

Table 4.4: Comparison of dilation% from experimental and FSI studies between present and previous investigations. The reported data for dilation% were obtained at p=40mmHg, in both experimental and computational cases.

In conclusion, a significant improvement of the present simulations should involve more realistic mechanical properties of the arterial tissue. This could be obtained by performing biaxial tensile testing. Alternatively, a description of another type of elastic or rubber material could be used, however, these materials also require parameters that should be determined experimentally. The dilation of the solid material is important in computational simulation, since it is the wall displacement that determines the strains and then calculates the stresses. Therefore, a change in this parameter affects the output data, which may be misleading in further use.

Apart from material properties, the results could have been affected by imposing a pressure at the outlet. For the simulations of the present study pressure was only imposed at the inlet of the vascular tube. At the outlet, the pressure was set to 0. A pressure pulse with a pressure drop could have resulted in different findings, and therefore further investigation could also include different outlet boundary conditions.

Nevertheless, the FSI models that were developed for the present study have been compared to analytical and experimental findings. Despite the small disagreement with the experimentally obtained dilation, there was a good agreement for the values of the circumferential stress and strain from the uniaxial test. Additionally, the models were mathematically verified, which allows the gradual improvement towards more physiological conditions.

The following investigation of the present study was focused on the effect of the macro-scale dilation in the microenvironment of the vascular wall, using computational and experimental methods. Because of the variation in the dilation between experimental and computational results, the values that were further applied were up to the average determined by the experimental data (≈20% extension of initial length).

Chapter 5. Investigation on the strain variation at the microenvironment of the vascular wall: Experimental Approach.

5.1 Introduction

This project was focused on the investigation on the macro-strains and how these translate into the microenvironment of a vascular wall. So far, the investigation was carried out at the macro-level. The results that were obtained from the macro-investigation (tissue dilation) were brought to be applied and examined at the micro-scale of the vascular wall. This investigation involved Finite element analysis and experimental procedures. The present chapter focuses on the FE analysis, while the experimental methods are described in the next chapter. The purpose of this part of research was to study the spread of the strain at the inner vascular wall, the tunica media, where the smooth muscle cells are embedded in the ECM of the tissue, which composes of collagen and elastin fibres. The focus of interest was to examine the strain that the fibres experience and its effect on the cells. The tunica media in small arteries comprises the greatest part of the vascular wall, and its study can assist on the development of tissue engineered blood vessels.

The ultimate purpose of the present investigation was to develop FEA models that can be employed as plattfroms to predict strains and stresses at the microenvironment of the vascular tissue. As mentioned earlier, stresses are of great importance for the cellular – and eventually for tissue – normal function. Information on these stresses are hard to be obtained experimentally. Therefore, computational methods are employed to provide this knowledge, so that it can be used to optimise bioreactor conditioning for the development of vascular grafts. Nevertheless, the present investigation at this point was not focused on the stresses, but on the strain. The reason for this was that the computational models were validated against experimenal findings. The strain variation was an ideal parameter to focus on, since first of all is closely related to stress, and secondly it could also be examined experimentally.

Despite the high importance in studying the microenvironment in the tunica media, there have been no other studies reporting on the strain – or the stress – on the collagen and elastin fibres of this layer.

This chapter describes the development of the computational simulation that was created, in order to investigate the strain at a micro-level. The model involved the simulation of collagen and elastin fibers. A 2-dimensional mesh map of collagen and elastin fibres was created in ScanIP software from tissue histology images of porcine femoral artery and it was run in Abaqus, as a 2D model, where it was given the mechanical properties of the materials and it was assigned the appropriate boundary conditions. The model was set as fixed from one side and stretched from the other side by 20% of its initial length. The 20% stretching was assessed previously from the macro-scale investigation, in Chapters 3 and 4, as the maximum performed dilation of the arteries under experimental test. The post-processing involved the analysis of the strain between different nodes, in order to investigate the strain spread between the collagen and elastin fibres. The obtained results were then compared to the ones found experimentally (described in the next chapter).

The following text describes the tissue histology process and imaging, the segmentation process in ScanIP, the description of the computational simulations in Abaqus, and the analysis of the computational results.

5.2 Materials and Methods

5.2.1 Tissue histology

The purpose of this process was to produce histology images that reveal the inner layer of the arterial wall, in terms of the collagen and the elastin fiber orientation. A schematic of this process is illustrated in Figure 5.1. The obtained images were used to create the mesh for the computational simulation, in order to investigate the strain effect at a micro-level.

To this purpose, one porcine leg from a freshly slaugthered animal (same day slaugther) was delivered from a local abatoir and the femoral artery was carefully removed. The artery was then cut in circumferential rings of about 0.5cm width. Each ring was then cut to form flat strips. The strips were then placed in plastic histological cassettes, where sponges were also used to keep the tissue samples as straight as

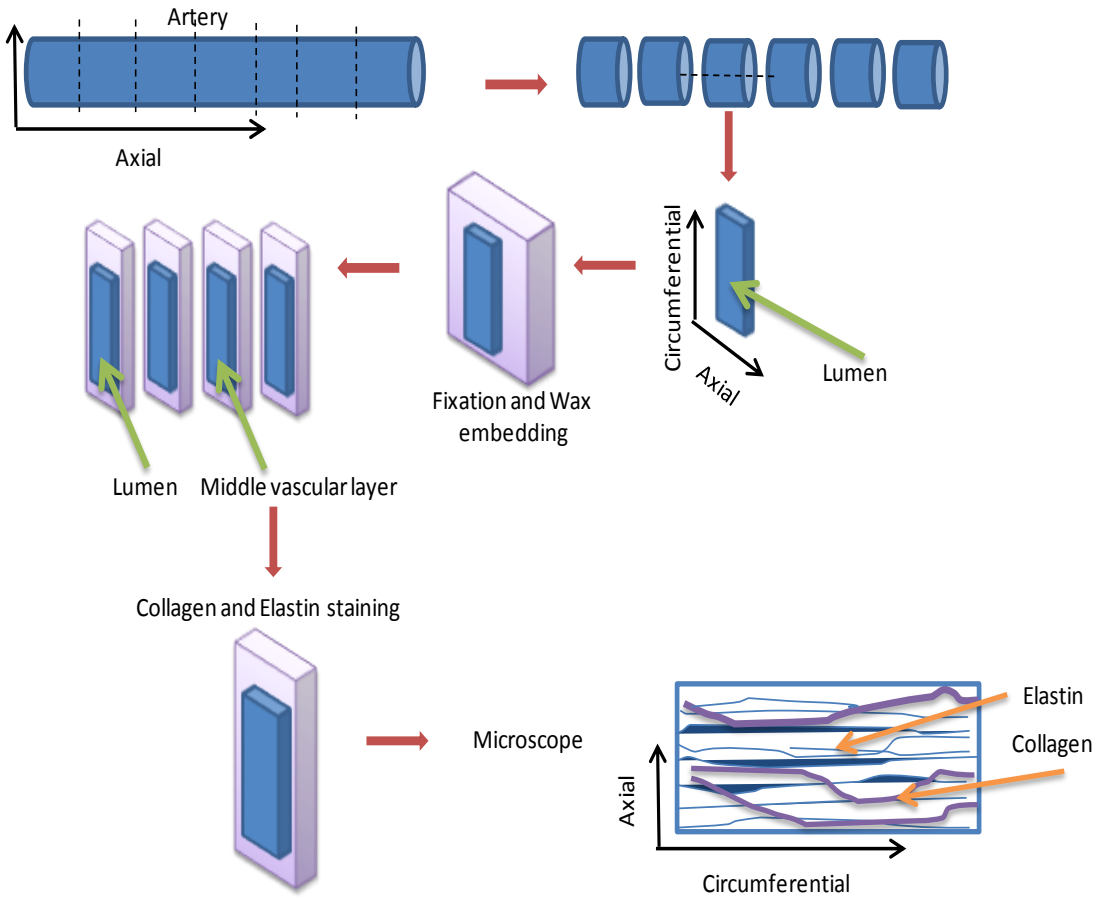

Figure 5.1: Schematic of histology process. One artery was initially disected in smaller rings. The rings were further cut to form flat sheets. After fixation in the tissue processor, the tissue layers were embedded in wax with the lumen facing the outer direction of the wax block. Samples of 5μm width were obtained in the microtome, where they were dissected along the circumferential direction. The samples that were chosen for the staining were within a depth between 50-150μm, in order to reveal the middle layer of the vascular wall. Collagen and elastin staining was further performed according to the in house protocol. Following, the samples were transfered to microscope for analysis and imaging.

possible. The cassettes were then immerged in formaline (BF 10%) overnight and then transfered for fixation to the tissue processor (Leica, TP11020). Within the tissue processor, the samples were immersed in each of the following solutions for an hour, under vacuum: neutral buffered formalin for fixation (10% w/v, Genta Medical, BFN250), a series of ethanol in different solutions between 70%-100% (v/v) for dehydration (Thermo Fisher Scientific Ltd, E/0555DF/25), xylene for tissue clearing (Genta Medical, LS81950/G) and finally in paraffin wax (Thermo Fisher Scientific Ltd, PS138/E). The temperature in this vacuum was a room temperature, except when the samples were immersed in the wax (~50ºC). Upon completion of

the tissue processor program, the specimens were removed from their cassettes and placed in metallic moulds (R.A. Lamb, E10.8/4161) in metalic histological cassettes with the lumen of the artery facing the bottom of the cassette. This enabled the isolation of histological sections from the lumen towards the media of the artery. The metallic moulds were then filled with molten wax, inside the wax oven (R.A. Lamb, E18/31). The samples were then left aside to cool, in order for the wax to fully solidify. The solidified wax was then removed from the metallic mould, and placed in a Leica rotary microtome (model RM2125 RTF). The specimens were then dissected in sections of 5μm width, at an angle of 4º, and placed in a water bath (R. A. Lamb, E65-2). The tissue stripes were then collected onto “Superfrost–Plus” microscope slides (Scientific Laboratory Supplies, MIC3040), and fixed by heating for 20 minutes at 60°C on a drying/hot plate (R. A. Lamb, E18.1). Following, the glass slides were placed in a slide holder (R.A. Lamb, E102).

The sections chosen for analysis were approximately the ones in a depth between 50-150μm of the tissue strips, in order to reveal the media layer of the vascular wall, as this is the main area of interest in the present study. These sections were then stained for collagen and elastin according to the established in-house protocol. In order for the specimens to clear from wax, the slide holder was immersed to dewax solution (Histo-Clear III, National Diagnostics HS-204) for about 10 minutes (2 washes), followed by washes in several ethanol (Thermo Fisher Scientific Ltd E/0555DF/25) concentrations (3x100%, 1x70%) and under running water for rehydration.

The sections were then immersed into 5 % (W/V) potassium permanganate (Thermo Fisher Scientific Ltd P/6520/53) for five minutes, an oxidizing agent which helps to minimize possible obscurence of the tissue detail. The samples were then washed in distilled water and were immersed into 1 % (w/v) oxalic acid (VWR International 1017440) for two minutes, for further bleaching, followed by two washes using distilled water, for rehydration. After two more baths in different ethanol consentration (70% and 95% (v/v) for one minute each), the samples were stained with Miller’s solution (Raymond A Lamb LAMB/080-D) for one hour, in order to reveal the elastin fibres. In order to clear the excessive stain, the sections were washed once more in ethanol (95% and 70% (v/v) this time) and under running water until clear. The sections were then stained in picro sirius red (VWR International F3B) for

one hour, for collagen detection, followed by washes in distilled water and ethanol in 70%(v/v) (for five seconds), and 100% (v/v) for five seconds, then two minutes and then three minutes. After immersion in histo-clear III twice for ten minutes, the staining procedure was completed by applying DPX mountant (Atom Scientific RRSP29) on the sections, in order to preserve the staining and the sliced were left aside overnight to dry.

The stained sections were then photographed under Olympus upright: Olympus BX51 (Image pro Plus Versions 4.5 & 7.1; Media cybernetics and later Zeiss Zen Blue 2014, Camera Olympus CX50 and latterly AxioCam MRc5), which are shown in Figure 5.2. From the obtained images, the collagen and the elastin fibers should be seen in red and blue respectively. However, the colours are not very clearly distinct, especially in the areas where the elastin staining is weak. For this reason, the images were taken under different brightness and contrast for all the samples, in order to allow the distinction between fibres. For example, collagen fibres look thicker and in the areas where they form bundles, elastin is not clearly or at all visible. Different contrast facilitates the elastin visibility by reducing the intensity of the coloured collagen bundles, as it can be seen in the first image of Figure 5.2. Additionally, low brightness gives better visibility in the fibres organisation and orientation, as shown in the second image in Figure 5.2.

The orientation of the fibers is clearly visible. The collagen fibers seem to be more abundant and more smoothly organised than the elastin. Although all the fibres seem to head to one direction (from the left to the right, for example), they do so in different angles. Further, despite the fact that the stained tissue samples were set straight under the microscope, the fibers seem to go diagonally. This can be considered as normal, since the fibers come in spirals to form the arterial tissue.

This process did not involve any cell staining. This was because the images obtained from the histology were to be used as a computational mesh, which at this stage should be quite simplified, in order to ease the computational simulation and reduce the computational cost. Additionally, since it is difficult to determine the strain in the cells experimentally, it will be investigated on the fibers, using the cells as reference points. For the computational case, the cells are not necessary, since the nodes of the mesh can be used as reference points instead. The next step of this process was to convert the obtained images into a computational mesh. One image

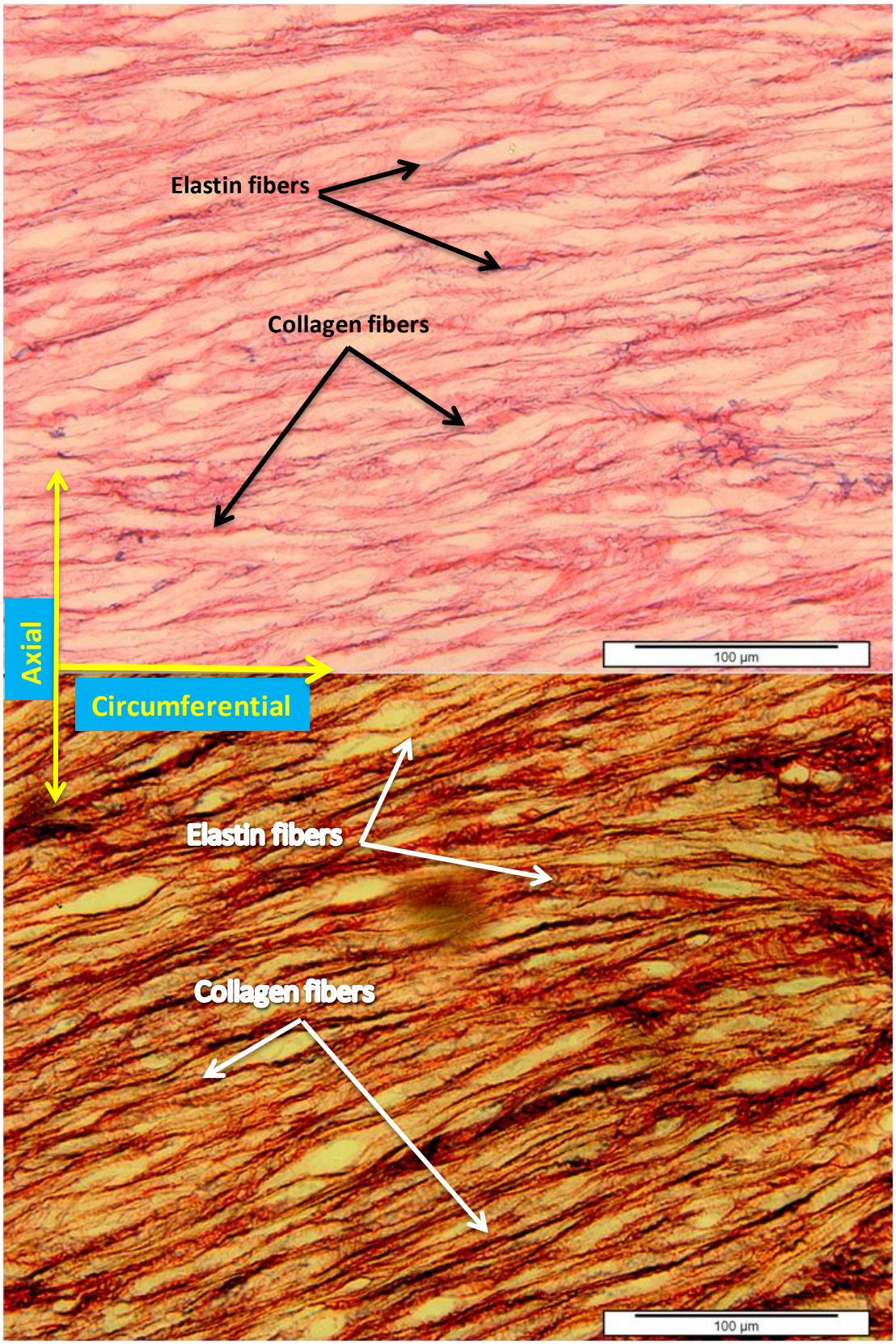

Figure 5.2: Images from arterial tissue histology. The images were taken under different brightness and contrast, in order to clearly distinguish the collagen from the elastin fibers. The scale bar indicates a length of 100 μm.

was selected out of one of the samples. The image selection was based on the clearest distinction between collagen and elastin fibres. The image conversion was realised using the commercial software Simpleware ScanIP, as described in the following text.

5.2.2 Image segmentation

Simpleware ScanIP is a commercial software that allows the conversion of image data into computational mesh. This software was created to process images from 3D scan data, such as MRI, CT, etc., and thus, the images can only be processed in a grey scale. An example of the software interface is shown in Figure 5.3. In the present case, the second image in Figure 5.2 was used, in order to develop the computational model. The image was in a TIFF file format with dimensions 2576x1932 pixels. Unfortunately, the grey scale of the image did not allow the exact identification of the fibers. The segmentation of the developed model was based on the threshold of the software, brightness and contrast, in order to identify the empty space between the fibers and the darkest parts, where the elastin fibers are dominant. In the areas where black&white view did not allow such a distinction, the components identification was based on observations on the other images of the same sample that were previously obtained from microscopy. Another drawback in the development of the present model was that there were areas in the image where collagen and elastin fibers coexist. However, the software can identify only one component at each point. In such cases, computer and advanced imaging experts could develop a computer code for each pixel of the image to allow the identification of two components at the same point. For an image in these dimensions, this process would involve around 5 millions codes. Of course this is beyond the scope of this study, in terms of time and expertise. An alternative solution was the user to decide which of the two materials should be identified, in order to assign the appropriate mechanical properties later on, during the FEA analysis. Of course, both materials are of great importance, since one provides the strength of the extracellular matrix and the other one the elasticity needed, in order to respond to the stresses that the tissue experience within the body. Despite the endless argument, the overlapped points were identified as elastin, under the assumption

that the elasticity is slightly more important in this study, rather than the strength, since the samples are stressed whithin physiological levels, and not to failure.

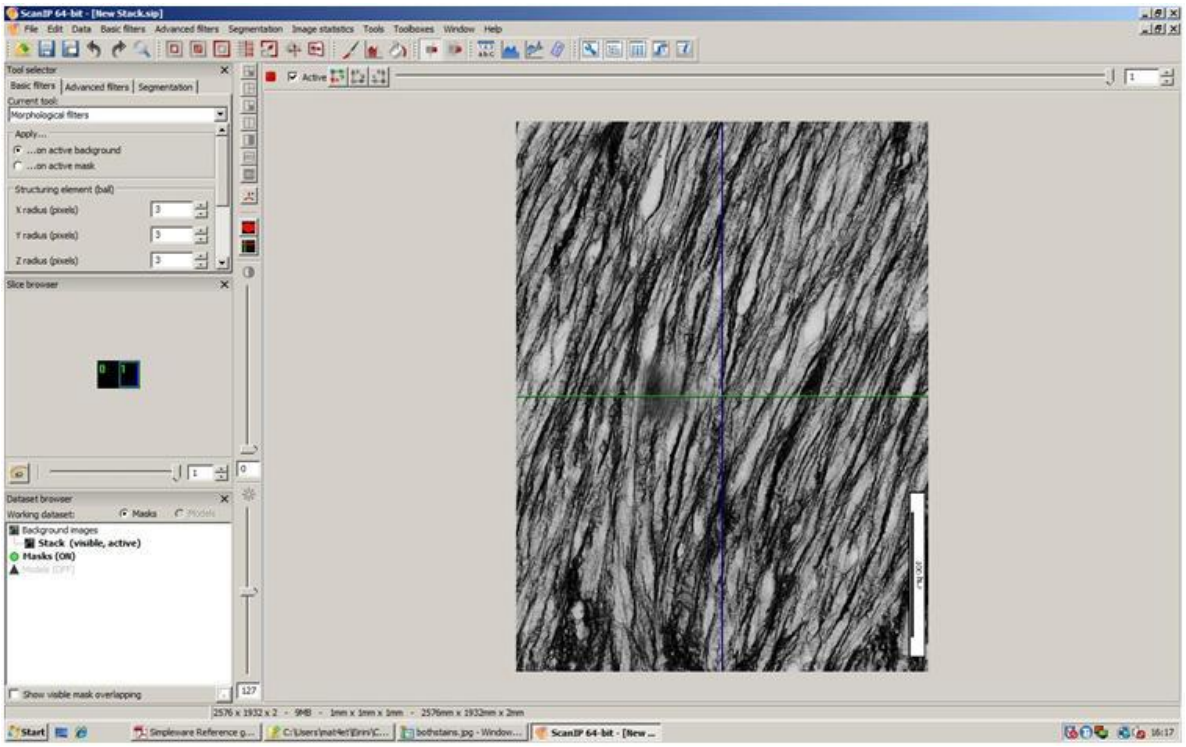

Figure 5.3: Illustration of the ScanIP interface. The inserted image from tissue histology appears in black and white, making hard to distinguish between collagen and elastin fibers.

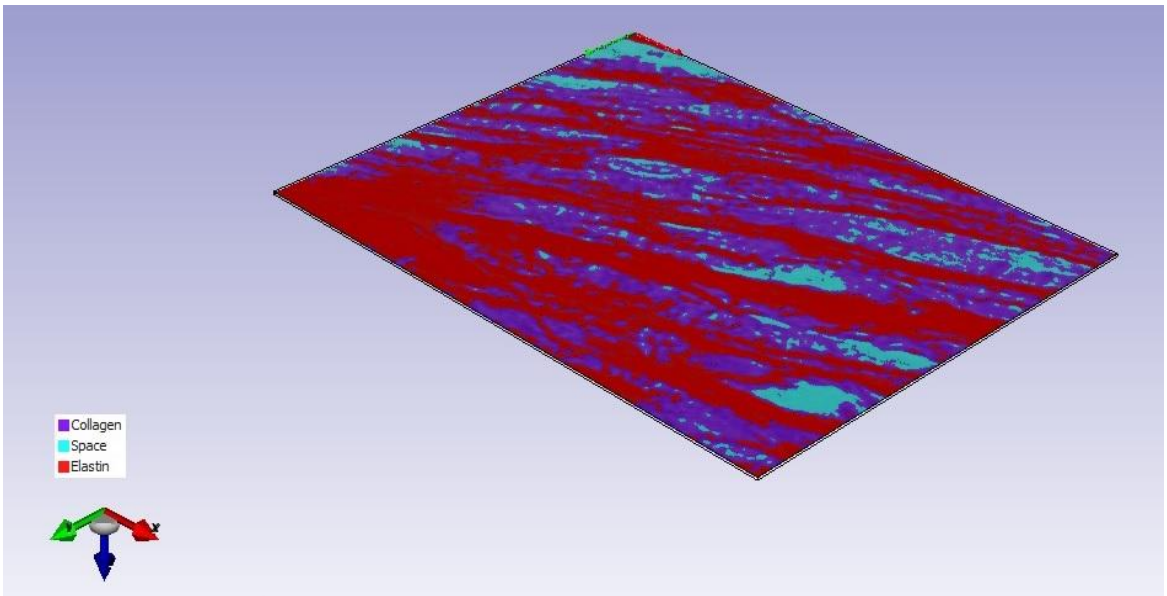

Figure 5.4: Demonstration of the masks created to identify each of the materials (collagen as purple, elastin as red and space as turqoise).

Three masks were then identified as elastin, collagen and empty space (Figure 5.4). In order to identify the mask for the empty space, the threshold was set at 180 and 255 for the lower and upper values respectively. Within this range, the space between the fibers seemed clearer and easier to be identified. Similarly, the range where the elastin fibers appeared more clearly seemed to be the one between 0 and 53 and for the collagen fibers 0 and 255. The masked image was conversed to a 2-dimensional mesh, resulting in 496,507 squared elements and 270,160 triangular, overall 766,667 elements. This type of mesh was basically an automatic suggestion of the ScanIP software. Any attempt to change the element type resulted in warning popups and eventually the mesh was recognised by Abaqus as incompatible. Despite the effort and advice, this problem remained unresolved and thus, the suggested mesh was used for further analysis. The mesh was exported as an input file and was imported in Abaqus for Finite element analysis.

5.5.3 Finite Element Analysis

The mesh created in ScanIP was imported in Abaqus software for further analysis (Figure 5.5). Using the same mesh, five (plus one for mesh sensitivity check) 2D models were created and run under different conditions. Each mask that was created in ScanIP was translated as a single section in Abaqus. Therefore, each section was allocated with different mechanical properties, according to the representing material. The first model (Model 1) that was created, was set as uniform, that is the same mechanical properties were allocated to all materials, using a linear elastic model, with a Young's modulus E=0.03GPa and Poisson's ration ν=0.45. The values that were used for this model are just random, because the purpose of this simulation was to check the effect of the space between the fibres. Therefore another model was developed (Model 2), where still the sections of collagen and elastin were given the same mechanical properties, while the space section was given a much lower value (1Pa). Within an arterial tissue, there is not any empty space. Between the fibres of collagen and elastin lie other substances, like fluid, nutrients, etc. These do not really affect the properties of the tissue and thus, they could be neglected. However, during histology process all these substances get destroyed and they leave empty spaces between the fibres, which

are clearly visible from the histology images. Using these images in ScanIP to construct the mesh for the simulations, these sections should not be treated as vacuum, because there is no such thing in a real case. Therefore, a really low Young's modulus was used to describe this section's material. For models 3, 4 and 5, space section Young's modulus was set as *E*=1Pa, elastin *E*=1MPa (Lillie and Gosline 2007), while different values were used for collagen material.

As explained in previous chapters, this study investigates the strain of the arterial tissue under physiological situations (or as close as possible). During such conditions, the tissue does not exceed its linear behaviour; therefore, the allocated mechanical properties of the components should involve the values obtained during the linear phase. In the case of the fibres, however, these have not been reported in the literature, and the only available information refers to the strength (collagen phase modulus) and not the elasticity (elastin phase modulus) of the material, after tests to the failure point. The value that was then used in the present simulations, was the lowest reported with *E*=3GPa (Sasaki and Odajima 1996), for Model 5, and was reduced by one order of magnitude, (0.3GPa and 0.03GPa) for models 4 and 3, under the assumption that the elastic modulus of a material is much lower than the collagen phase modulus. A similar argument holds for the modulus that was used for the elastin material. However, since this is much lower than the collagen value, it was used as reported for all three models. All the mechanical properties that were used for each model are listed in Table 5.1.

Finally, one more model was developed to check on the mesh sensitivity, meshed with 1,860,675 tetrahedral elements and was run under the same conditions that were used for Model 5. Again, at this number of elements this type of mesh was automatically suggested by ScanIp.

The left side nodes of the mesh were set as fixed for all models, and a displacement condition was used to the right side nodes. Each model was run 4 times, under a different displacement condition, 5% displacement of the initial length, 10%, 15% and 20%, towards the circumferential direction of the tissue. This displacement was chosen using the information provided from the experimental pressure test, described in Chapter 3, where the maximum dilation of the arteries was ~20%. The gradual increase in the applied displacement was used to investigate the local strain spread at different macro-scale strains.

Figure 5.5: This figure shows a part of the mesh developed for the computational simulation described. The actual size of the image was too big for the Abaqus interface, so that it had to be zoomed in in order to be seen into a more detail.

Model	Collagen (GPa)	Elastin (GPa)	Space (GPa)
1	0,03	0,03	0,03
2	0,03	0,03	1E-9
3	0,03	0,001	1E-9
4	0,3	0,001	1E-9
5	3	0,001	1E-9
6 (Mesh dependence)	0,03	0,001	1E-9

Table 5.1: List of the mechanical properties used for each of the tissue components (collagen, elastin and space) for each of the models developed.

5.3 Results

The present investigation focuses on the strain experienced by the cells that lie on the middle layer of the arterial wall, during dilation caused by the blood flowing within. Up to this point, only the macroscale displacement has been investigated in previous chapters. However, the present simulations were created in order to

examine how this strain is translated into a microscale level, at the level of the fibres and cells. For simplicity reasons, the simulation did not include any cells, and thus some reference points were determined on the mesh, in order to calculate the distance between them. The reference nodal points were selected to belong to the middle area of the mesh. The reason behind this was that when the mesh would be stretched uniaxially, it will present extremes at the edges, in terms of extension and shrinkage. Such extremes do not apply in a physiological condition. Therefore, the middle area of the mesh is a safer option for the present investigation.

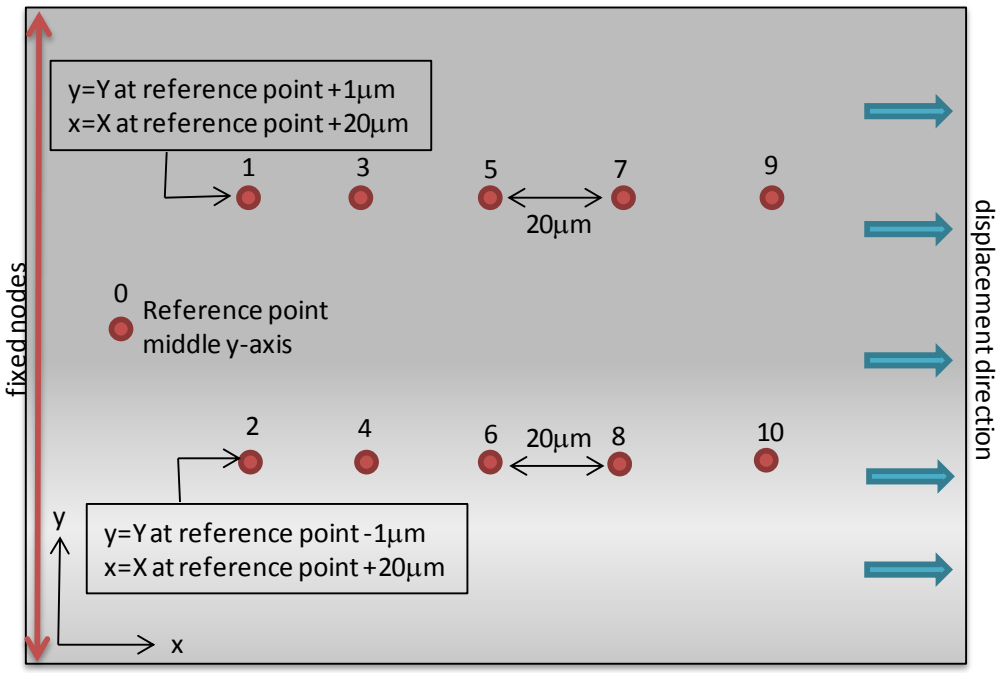

Figure 5.6: Schematic on the node identification on the mesh used for further investigation.

The node identification was realised with the aid of a Python script (Appendix I). The script was programmed to identify one node at the middle of the y-axis and early x-axis. Using this as a reference point (point 0), ten more nodes were identified, five at Y=(Reference point + 1μm) and another five at Y=(Reference point - 1μm), with an x-distance between them of 20μm. All the nodes were identified under the precondition to belong to a fibre (either collagen or elastin) and not on an empty space. The identified nodes can be seen on the schematic in Figure 5.6.

After identification, the script was set to report the exact position of each node, before and after stretching.

The script was also programmed to report the distance of each point from the reference point 0, in x-direction, in y-direction and the overall distance as well. The results reported here were based on the distance between the points. The distances calculated involved the ones between points 3-5, 5-7, 3-7, and 4-8. These points were chosen because of their position in the middle area of the sample and were used to examine the strain at smaller (p3-5 and p5-7) and larger (p3-7 and p4-8) initial distances. Using the values given by the script as initial distance and post-simulation distance, the strain percentage was calculated in Excel as $\%strain = [(L_1 - L_0)/L_0]*100$, where L_1=post-distance and L_0=initial distance between the nodes. The results were plotted in graphs, which are demonstrated in Figures 5.7, 5.8, 5.9 and 5.10, for each displacement condition, 5%, 10%, 15% and 20%. Each graph indicated the strain percentage as calculated between the respective points and for each of the models, along with the average values. All the error bars are within the confidence interval of 95%. For inhomogeneous materials, the average value of micro-strains should be expected to match the macro-applied strain (displacement imposed as boundary condition), and thus, to indicate the reasoning of the computational simulations.

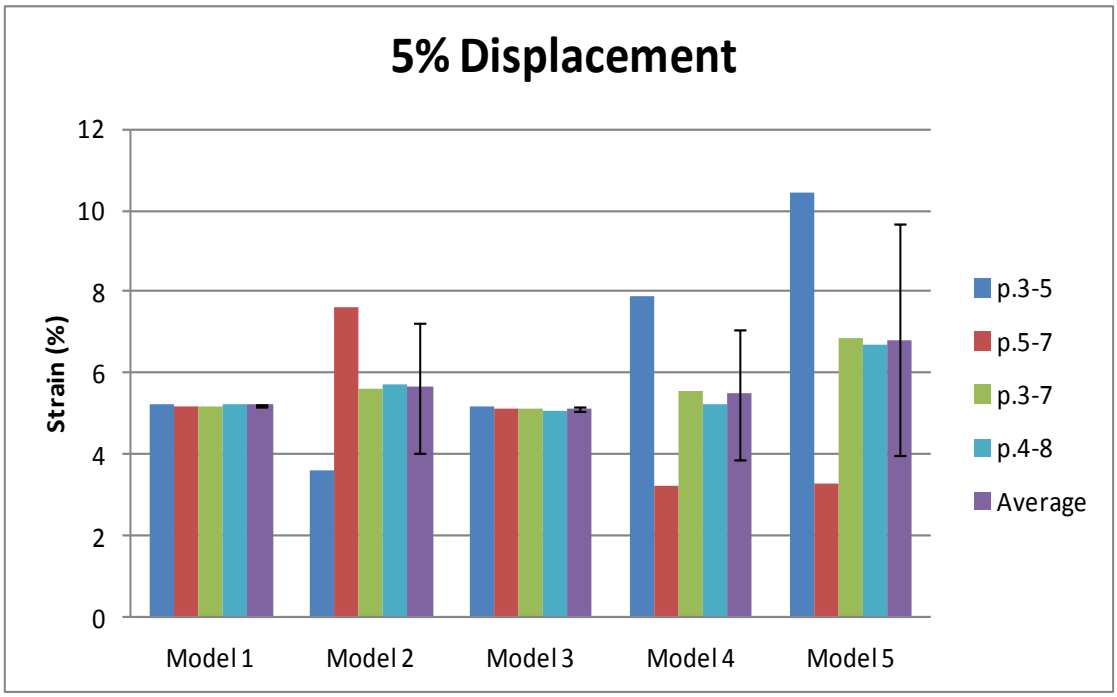

Figure 5.7: The micro-strain results obtained at 5% tissue displacement for four pair of nodes and their average for all five models. The error bar indicated a confidence interval of 95%.

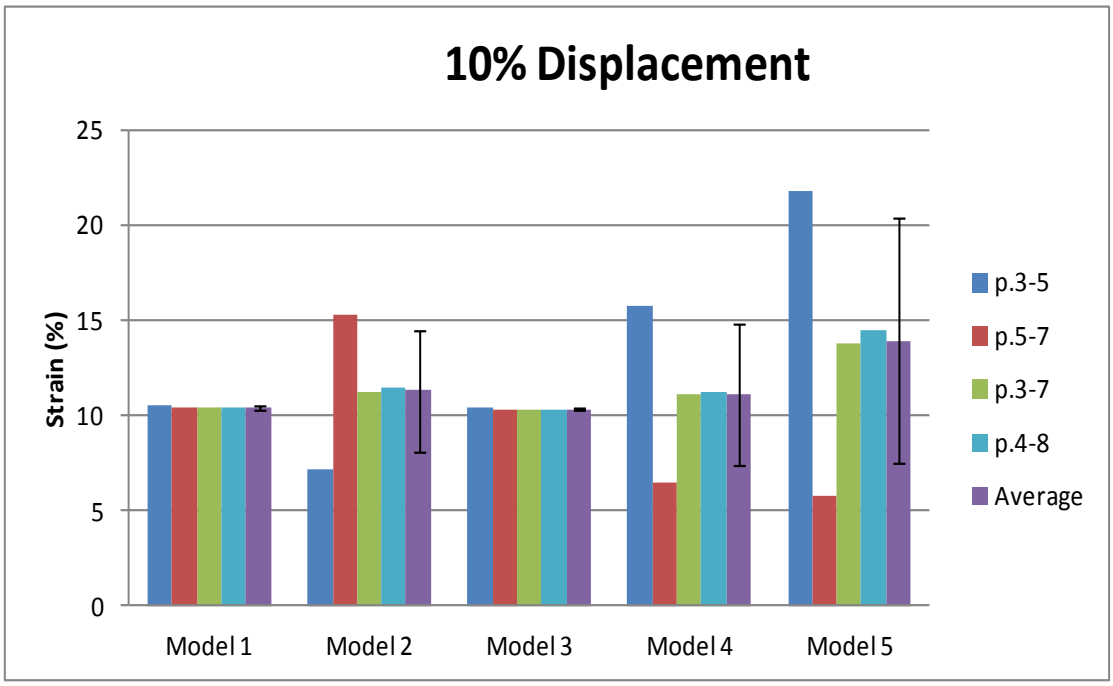

Figure 5.8: The micro-strain results obtained at 10% tissue displacement for four pair of nodes and their average for all five models. The error bar indicated a confidence interval of 95%.

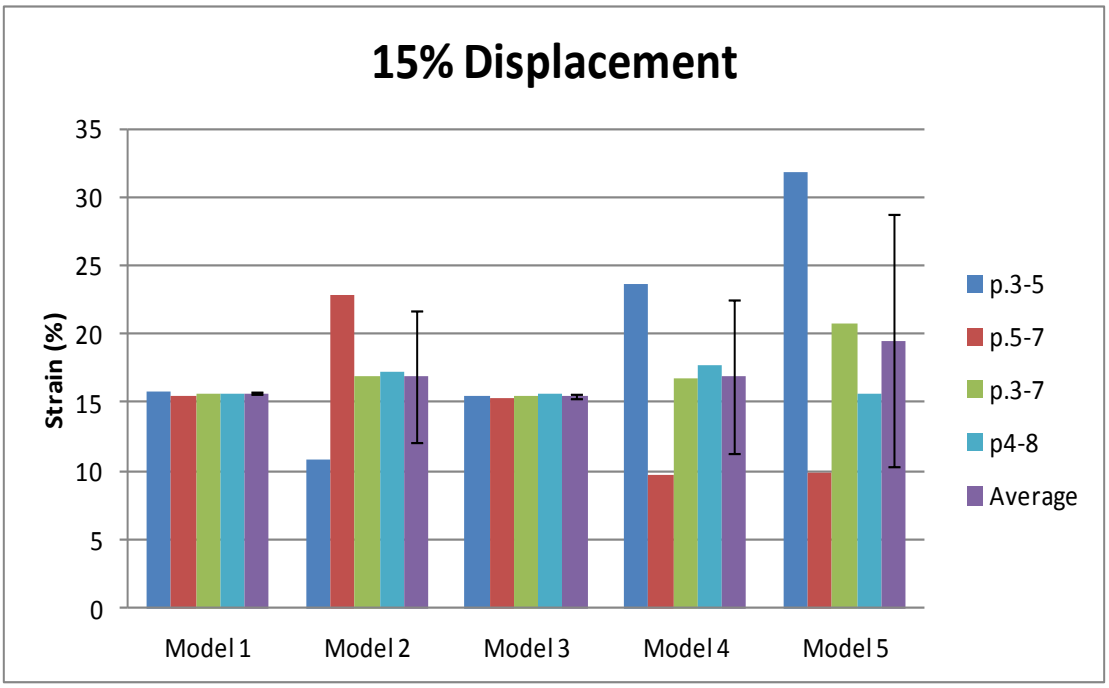

Figure 5.9: The micro-strain results obtained at 15% tissue displacement for four pair of nodes and their average for all five models. The error bar indicated a confidence interval of 95%.

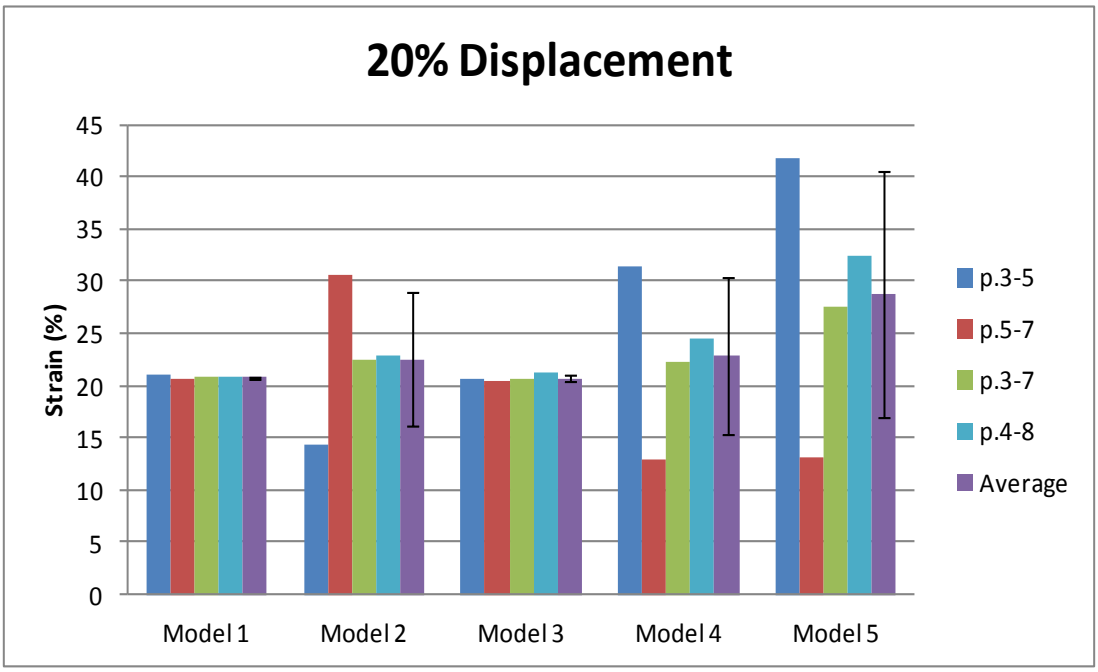

Figure 5.10: The micro-strain results obtained at 20% tissue displacement for four pair of nodes and their average for all five models. The error bar indicated a confidence interval of 95%.

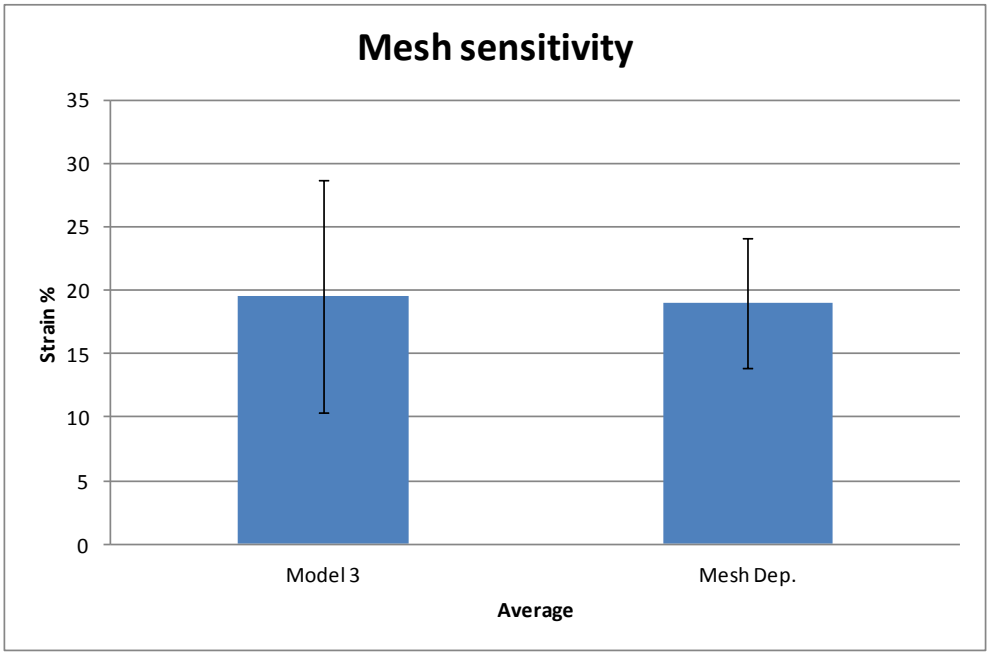

Figure 5.11: The results obtained from mesh sensitivity test. Model 3 was used at 15% displacement against a finer mesh model under the same conditions. The result indicate that the finer mesh model results in a smaller variation, as the error bar (95% CI) is smaller .

The results from the mesh sensitivity test are shown in Figure 5.11, where the distance average of the selected points is plotted for the finer mesh against the one of Model 3. The difference of the actual values (19% for the finer model and 19.5% for model 3) can be considered as negligible, however the difference of the error bar indicate more accuracy for the finer mesh model.

5.4 Discussion

The purpose of the work presented in this chapter was to investigate the strain at the micro-level of the arterial tissue using FEA. This was achieved by developing a 2D computational model, which was based on the histoarchitecture of the media layer of the arterial wall that was obtained from histological images that revealed the orientation of the collagen and elastin fibres. The images were segmented in Simpleware ScanIP, in terms of the main constituent ECM proteins of the arterial wall (collagen and elastin) and, subsequently, meshed as a shell using shell elements. This process carried several limitations. Firstly, the ScanIP interface utilised a grey scale that made it difficult to accurately distinguish between the elastin and the collagen fibres. Moreover, the regions where the elastin and collagen overlapped were identified as one material (either elastin or collagen). This decision could have affected the orientation of the fibres and, thus, the properties of the mesh, making it either stiffer or more elastic. In order to improve the mesh in terms of accuracy, more advanced imaging techniques, such as multiphoton laser microscopy and second harmonic generation, would have been necessary in order to distinguish between the collagen and elastin networks. However this was beyond the scope of the present project. Nevertheless, the developed mesh resulted in an adequate approximation, when compared to the histology images, in terms of the fibres orientation and consistency of the components.

Once developed, the meshed histoarchitecture was imported in Abaqus, where it was assigned the mechanical properties for each material, as well as the boundary conditions. The left-side nodes at the boundary of the geometry were fully constrained, while nodes at the right-side boundary of the geometry were subjected to either 5%, 10%, 15% or 20% strain along the x-direction (Figure 5.6), which corresponded to the circumferential direction of the arterial wall (Figure 5.1). Several

nodes were identified in the middle area of the mesh, with the aid of a Python script, which were used as reference points in the analysis. The coordinates of each of these nodes were recorded during the simulation and used in the calculation of the strain experienced by the collagen and elastin fibres.

Five models were run, using the same conditions but with different mechanical properties assigned to the ECM constituents and taken from the literature. The results obtained from this investigation indicated that there was a variation of strain between the points, which depended on the difference in the mechanical properties of the tissue components. The results for Model 1 appeared to be uniform, since the properties of the different ECM constituents were set to be the same, basically modelling a homogeneous material. In Model 2, however, the reduction of the modulus of the space regions to 1E-9 GPa, while keeping the modulus of the elastin and collagen to 0.03 GPa, produced a differentiation in the strain variation between the node intervals 3-5 and 5-7. On the other hand, the average strain between the node intervals 3-5 and 5-7 was roughly equal to the strain calculated for the node interval 3-7 (Figure 5.7). The variation in the strain between the node intervals 3-5 and 5-7 was manifested by an increase in the strain experienced by the node interval 5-7, compared to Model 1. This increase, which was a result of the reduction of the modulus of the space regions (ground substance) in Model 2, indicated that the ratio of the space regions to the combined amount of elastin and collagen was higher in the vicinity between nodes 5 and 7.

In models 3, 4 and 5, the modulus of the collagen fibres was set to 0.03 GPa, 0.3 GPa, 3 GPa, respectively, whereas in all 3 models the modulus of the space regions and elastin fibres was kept the same at 1E-9 GPa and 0.001 GPa, respectively. In Model 3, the reduction of the modulus of the elastin caused an increase in the strain calculated for the node interval 3-5 compared to Model 2, indicating the prevalence of elastin in the vicinity between nodes 3 and 5. As a result of this, the strain spread was equally balanced between the node intervals 3-5 and 5-7 in Model 3, with their average strain roughly equalling the strain calculated for the node interval 3-7 (Figure 5.7). Further increase of the modulus of collagen in Models 4 and 5, while keeping the modulus of the elastin and the space regions the same as in Model 3, generated a higher resistance to deformation in node interval 5-7, which was manifested by the lower strain calculated for this interval by Models 4 and 5,

compared to Model 3. This, in turn, resulted in node interval 3-5 to undertake the majority of the deformation. Similarly to the previous models, the average strain between intervals 3-5 and 5-7 was roughly equal to the strain calculated for node interval 3-7 by Models 4 and 5. In all models, the variation in the local strain variation did not seem to change significantly for the different global strain conditions (5%, 10%, 15% and 20%) simulated. This was expected, since all the components of the model were defined as linear elastic. Moreover, and in all global strain conditions applied, the average of the local strains (node intervals 3-5, 5-7, 3-7, 4-8) for Models 1, 2, 3 and 4 was approximately equal to the respective global strain applied. This was not the case for Model 5, in which the average of the local strains exceeded substantially the global strain in all strain conditions simulated (Figure 5.7, 5.8, 5.9, 5.10). In light of this, and due to the fact that the local strains in Models 1 and 3 were predicted to be too homogeneous for an inhomogeneous material and that the elastin and collagen modulus in Models 1 and 2 were set to be the same, Model 4 seemed to be the most reasonable, in terms of both inhomogeneicity and averaged strain.

These computational modelling results demonstrated that the local strain sampling was adequate to detect and take into account the inhomogeneity of the modelled tissue and that the applied global strain was translated differently at the local microenvironment. Due to the application of the global strain condition, the inhomogeneous mesh had to attain the applied strain, unless it got ruptured, which was not the case. The nodes under investigation were selected on the precondition to belong to a fibre, either collagen or elastin, but not necessarily to the same type. Moreover, the node intervals investigated might have includes any of the three ECM components modelled in the mesh. Since the collagen was modelled as the stiffer material, it generated a higher resistance to deformation, whereas the less stiff components of the tissue, such as the elastin, strained more in order to attain the applied global strain. As a result of the above, the node intervals that were investigated achieved different levels of local microstrain. In addition, the fibres in the mesh were not perfectly aligned along the direction of the applied global strain, due to the spiral alignment of the fibres in the arterial wall. This might have also affected the predicted local strains that were calculated along the x-direction (along the direction of the applied strain).

The observation that the applied global strain was translated differently at the local microenvironment was also reported by Screen *et al.* (2004) in an experimental study that investigated the translation of macroscale strain to the microscale in rat tail tendon fascicles, using the resident tenocytes as markers. That study indicated that the local strain values at the fibre-level were much smaller than the uniaxially applied macroscale strain, and concluded that this observation was due to the tendon histoarchitecture. Specifically, under unstrained conditions the collagen fibres of the tendon demonstrated an uncrimped configuration, whereas when strain was applied, they started to align along the direction of the applied strain and, eventually, started to stretch. A schematic of this process is demonstrated in Figure 5.12. Since the tenocytes (used as markers) were attached to the collagen fibres, the distance between them started to increase only after the collagen fibres uncrimped, aligned with the direction of the applied strain and then started to stretch. This process generated a lower strain in the collagen fibres (as calculated by the displacement of the tenocytes) than the applied global strain.

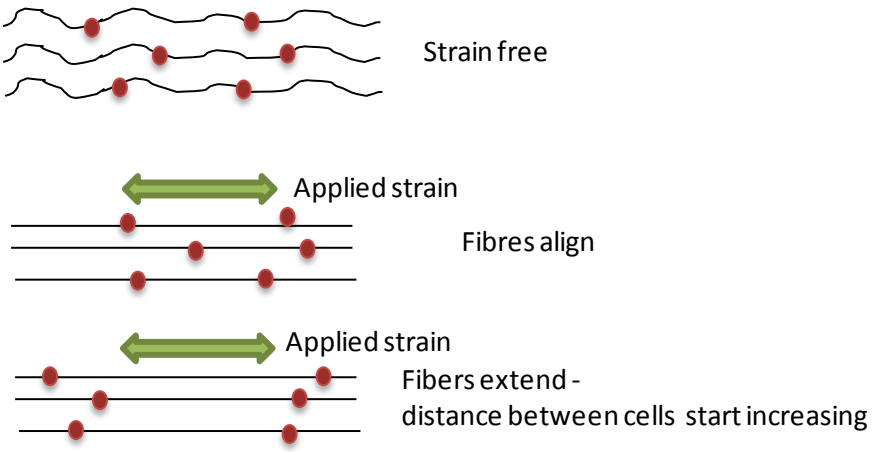

Figure 5.12: Schematic of the tendon fibres stretching process when loading is applied. Modified from Screen *et al. 2004.*

In the present study, the different values used for the modulus of the collagen and the elastin were not obtained from experimental measurements, since the literature only reports on experimentally-derived values for the high modulus phase of the collagen and elastin. The collagen modulus that was obtained from previous studies was used only for Model 5 (3GPa) and reduced by one order of magnitude

for each of Models 4 and 3, to 0,3 GPa and 0,03 GPa respectively, in an attempt to approximate the low modulus of collagen. However, since these moduli are difficult to be determined experimentally, the actual values might not be as significant as the orders of magnitude of the difference between the moduli of the ECM components. This later assumption was supported by the simulations, since the results indicated that it was required to increase the difference between the moduli of the collagen and elastin by at least 1 order of magnitude, in order to observe a significant effect in the local strain apportionment between the different node intervals studied.

Another limitation of the present study refers to the lack of the crimp effect in the computational simulations, since crimp has not been taken into account, and consequently has affected the outcome results.

Finally, it should also be mentioned that the mesh used in the models described in this chapter was limited to a shell and it was not a 3D structure, whereas the applied strain was applied uniaxially, as indicated in Figure 5.6. Physiologically, arterial tissue is a multi-laminar structure with multiple layers of collagen and elastin fibres, whereas it undergoes multiaxial deformation under the pulsatile flow of the blood. A more physiological model would involve a 3D mesh, based on a stack of sequential histology images that would more accurately describe the 3D structure of the arterial wall, as well as the application of biaxial strain as boundary condition and more realistic mechanical properties for ECM components.

Chapter 6. Investigation on the strain variation at the microenvironment of the vascular wall: Experimental approach.

6.1 Introduction

The aim of the present work was to develop experimental methods which would allow the visualisation of the local strain variation in the arterial wall, during stretching. The rationale behind this was to obtain comparable findings to the computational simulation, which was earlier developed for validation purposes. The developed method was inspired by Screen et al. (2003, 2004), where tendon fascicles were examined under the confocal microscope during stretching, with the aid of a specially designed rig. The embedded cells were stained and used as markers, and the distance between them was employed to assess the local strain spread. Similarly, for the present study, fresh arterial tissue was dissected and stained for cell nuclei. Following, the stained tissue strips were mounted on a uniaxial tensile rig, which was designed to fit under the confocal microscope. The tissue strips were uniaxially stretched up to 20% of their initial length, incrementally. This strain value derives from the earlier findings reported in Chapters 3 and 4, which were also used for the computational simulations.

Confocal microscopy carries the advantage of penetration, and thus allows the visualisation of the inner tissue layers. Several set of images of the stretched tissue were then obtained at each increment, illustrating the global strain effect in the microenvironment within the middle layer of the vascular wall. From the obtained set of images, identical pairs of cells were identified for each increment, and the distance between them was calculated to give information on the local strain variation. The findings were then compared to the ones obtained from the computational simulations, as described in Chapter 5.

6.2 Methods and Materials

Five femoral arteries were dissected from fresh porcine legs (same day of slaughtering), which were obtained from a local abattoir. The arteries were emerged into transport medium (prepared according to the in-house protocol as previously described in Chapter 3) straight after dissection and kept until staining, in order to remain alive. The excess fat around the tissue was carefully removed to prevent damage to the artery. The tissue was then stained with Hoechst (Invitrogen H3570, 10μg/ml), a blue fluorescent dye that stains the DNA and thus reveals the cell nuclei, even in live cells, without causing any damage. Hoechst was diluted in transport medium (1.8μl into 50ml) and the tissue was stained for 1 hour. The tissue was then washed three times, still with transport medium on the shaker for ten minutes.

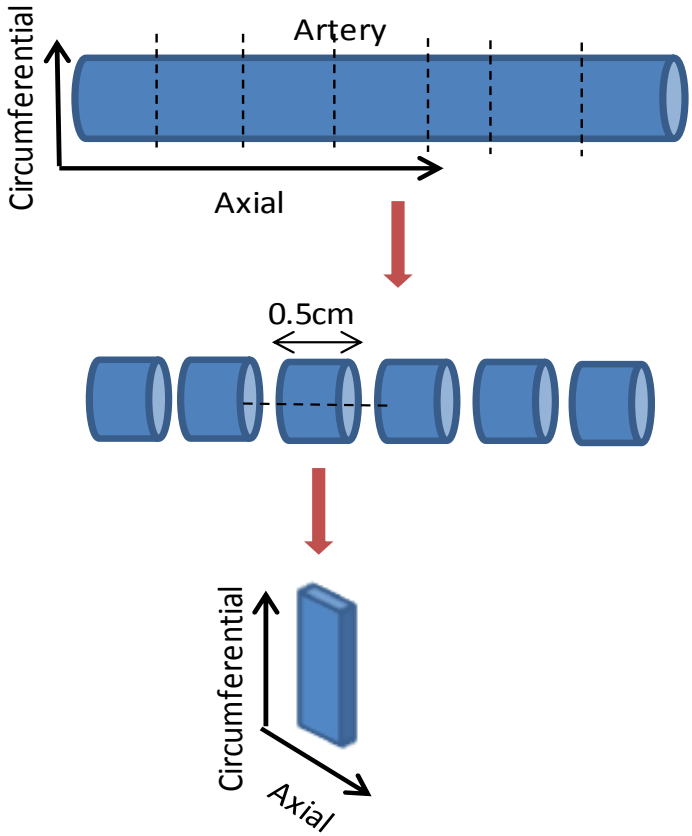

Figure 6.1: Schematic of the dissection process towards the sample collection for investigation.

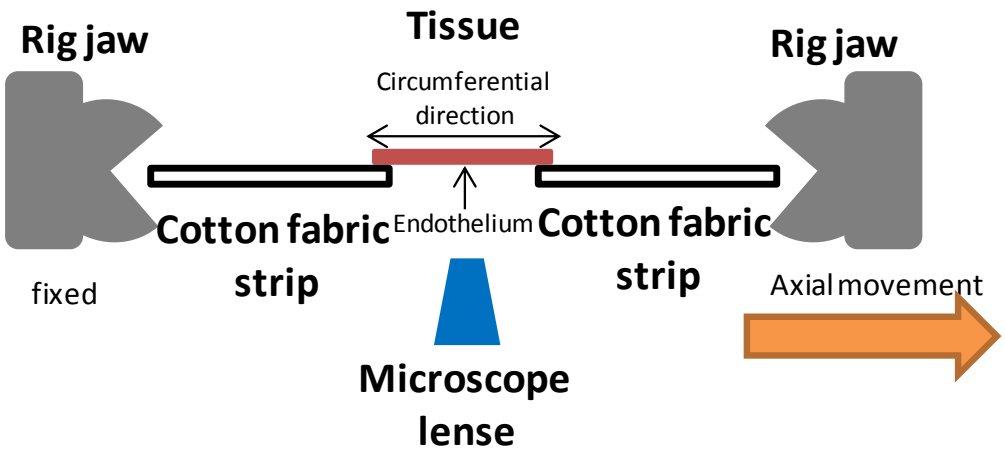

Figure 6.2: Schematic of the tissue mounting on the tensile rig

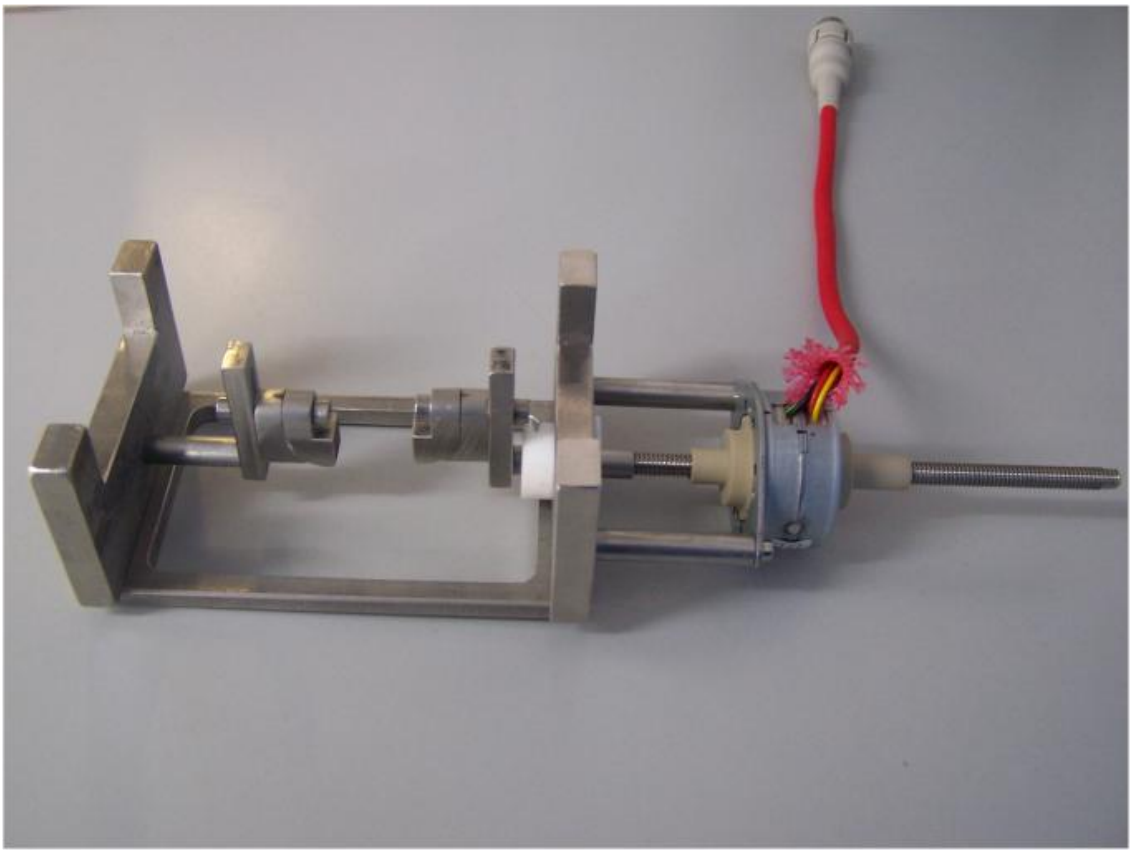

Figure 6.3: The uniaxial tensile ring was specially designed to fit under the confocal microscope. The left jaw of the rig may be fixed to the convenience of the user, while the right jaw may move at uniaxial direction (back and forth). The right jaw is connected to a console through which the user controls the system and it functions with electric power.

The arteries were then divided into smaller rings of length 0.5cm long. The rings were then cut to form flat strips. A schematic of the dissection process is shown in Figure 6.1. The top and the bottom edges of the tissue strips were carefully super-glued on cotton fabric strips, which were used to assist tissue mounting on the tensile rig. The tissue sample was positioned to be stretched along circumferential direction with the endothelium to face down (Figure 6.2).

The specimens were then mounted on a small tensile rig (Figure 6.3), which was specially designed to fit under the confocal microscope (Zeiss LSM510 META Inverted confocal microscope). The left jaw of the rig was fixed, while the right one allows movement along the axial direction, electrically. The movement of the right jaw was controlled with a console towards the desired direction (back or forth) to the desired distance (between 0.04-1.28mm). Before placing the rig under the microscope, the length of the tissue was measured from the one end of the fabric strip to the other, using an electronic calliper. According to this length (L_0), the 20% of displacement was calculated as (L_0*20)/100.

The experiment took place under the confocal microscope, because of its convenient penetration within the tissue wall (up to 100μm). The area of interest was in a depth between 30-50μm, depending on the focus clarity. Within the vascular tissue wall, this distant is sufficient to view the middle layer of the artery.

After focusing the desired plane, an image was taken to identify the zero-applied strain position of the tissue. The zero-applied strain, however, does not necessarily means zero-strain on the tissue. During mounting process the tissue unavoidably have been subject to stretching, therefore, at the zero-applied-strain the tissue may already have either a negative or a positive strain. For the imaging, the tiling option was selected, which allows the viewing of the broader area of the actual focus. For the present case, the tiling option was set 5x1, which tiles 5 images in the *x*-direction and a single image in the *y*-direction. This distance was enough to follow the same cells during stretching from 0 up to 20% strain of the tissue testing length.

Following the first image capture, the rig was set to move 0.2mm and then to stop. A distance of 0.2mm seemed ideal for the present experiment for several reasons: first, a larger distance would stretch the tissue further and it would be hard to refocus and follow the same cells, while a smaller distance would slow the step-by-step stretching process down, so that the tissue would dry out before it would

reach the certain strain percentage. At this point, the initial plane was refocused and another image was taken. This process continued until a 20% macro strain was reached.

Seven samples were used for this investigation, which were obtained out of five arteries. The capital letter at each sample represents the artery (A, D, E), while the number represents the samples from same artery (B1 and B2, C1 and C2).

6.3 Results

6.3.1 Confocal Microscopy

The sets of the images obtained for each of the samples were used to calculate the distance between certain cells, which were distinguishable in every image. The micro strain percentage was calculated at approximately 5%, 10% and 15% of macro strain, according to the formula $(L_i\text{-}L_0/L_0)*100$, where L_0 is the initial distance between the cells before any stretch is applied, and L_i is the distance where *i*=5%, 10%, 15% and 20% macro strain. An example of the set of images and the cells chosen is illustrated in Figure 6.4, where they can be seen in inverted colours. The results obtained for each of the samples were plotted for each of the strain percentages (Figures 6.5, 6.6, 6.7 and 6.8), as well as their average. The average value for 5% macro strain was 4.23±2.9%micro strain, for 10% was 10.1±4.2%, for 15% was 14.93±7.7% and for 20% was 20.1±6%. The error bars indicate a confidence interval of 95%. The initial distance between the cells for each of the samples is demonstrated in Table 6.1. For the samples B and C there were two measurements on each slide, that is the distance between two pairs of cells in the same tissue sample (1 and 2), while only one pair was followed for the samples A, D and E.

Sample	**A**	**B1**	**B2**	**C1**	**C2**	**D**	**E**
Cell distance (μm)	107	176.75	24.5	20.25	35.5	63.185	113.7

Table 6.1: List of the initial distance between the cells for each sample.

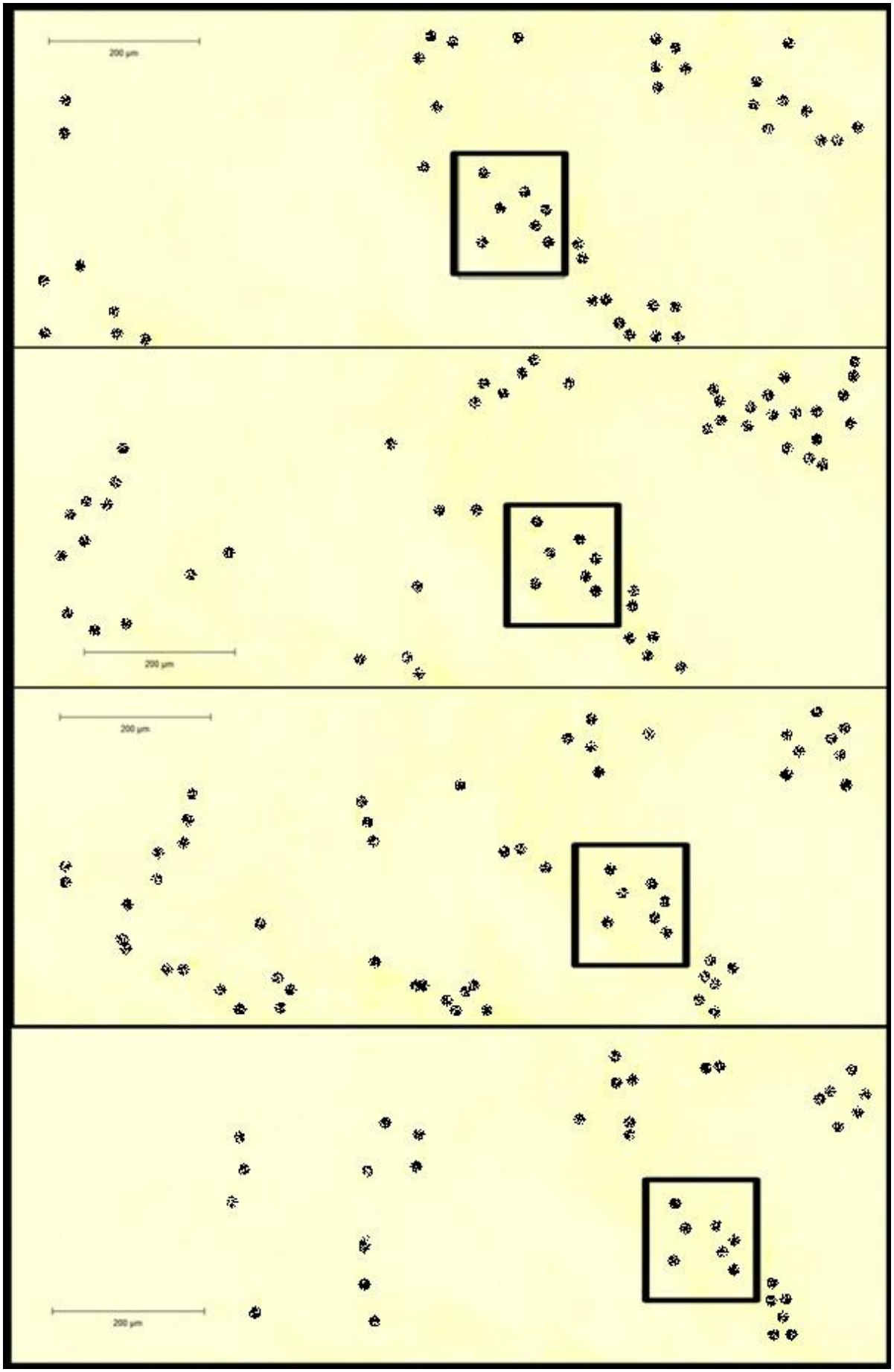
200 µm
200 µm
200 µm
200 µm

Figure 6.4: Illustration of the image post-processing for the calculation of the distance between certain cells at 0%, 5%, 10%, 15% and 20% of tissue macro strain. One pair of cells was initially identified and was followed in each stretching step. The chosen pairs of cells had to be clearly visible in order to proceed to the next step until a 20% of displacement was reached. The scale bar indicates a length of 200μm. The illustrated images were processed in Microsoft Paint, in order to invert the colours and to enable clear visualisation.

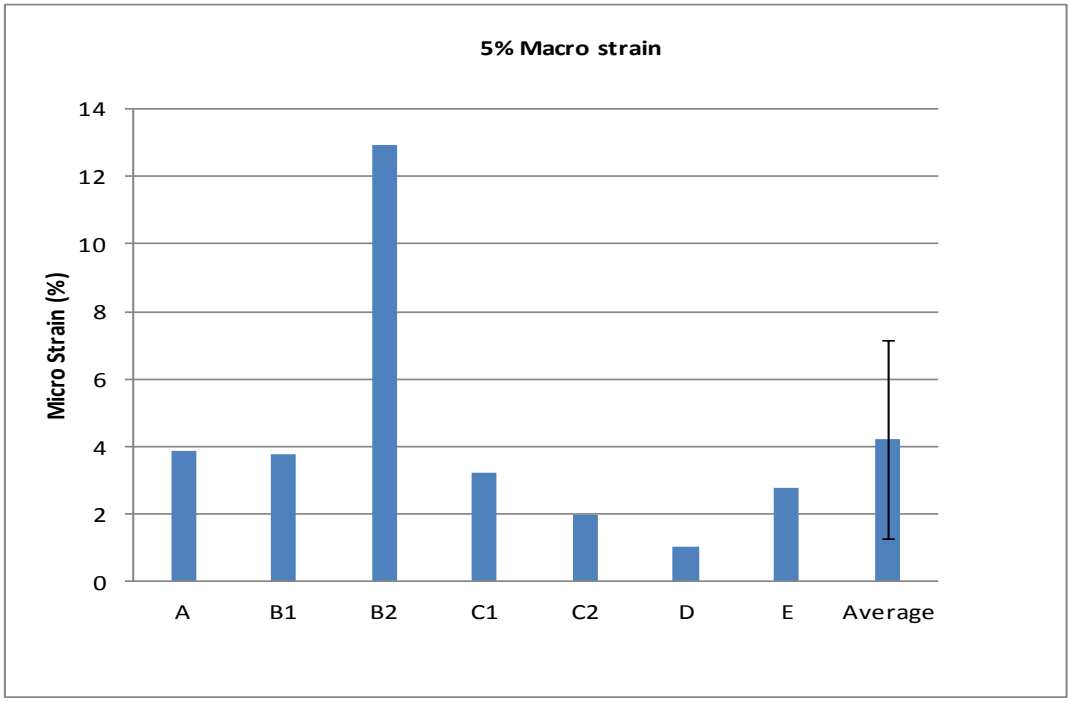

Figure 6.5: The results obtained indicate the strain percentage between the cells at 5% strain of the tissue.

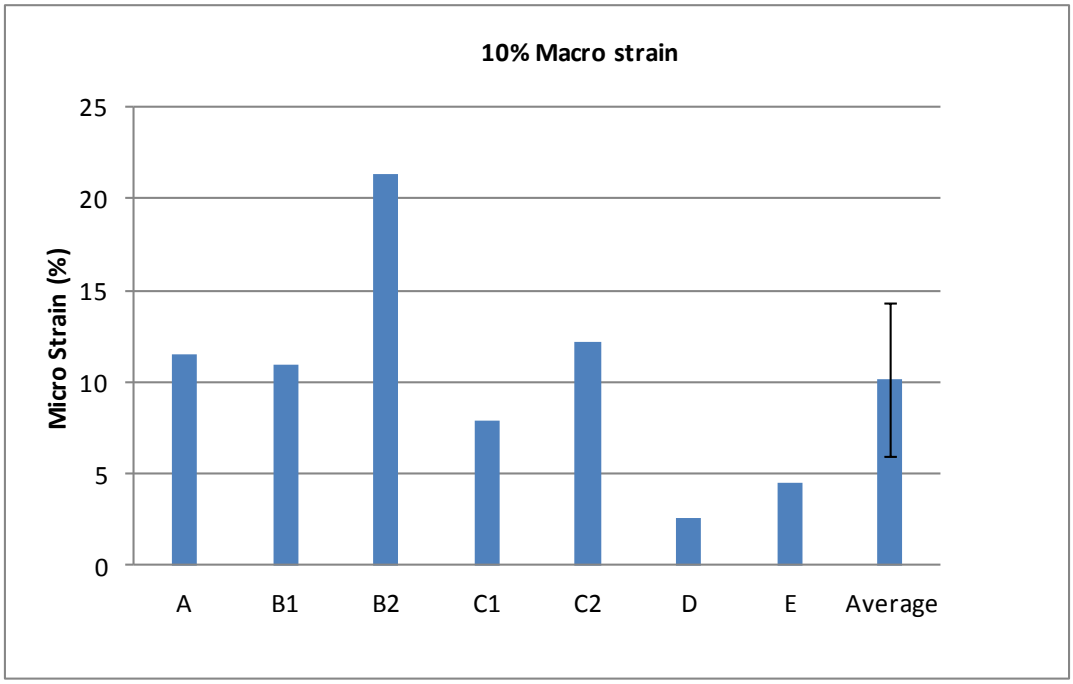

Figure 6.6: The results obtained indicate the strain percentage between the cells at 10% strain of the tissue.

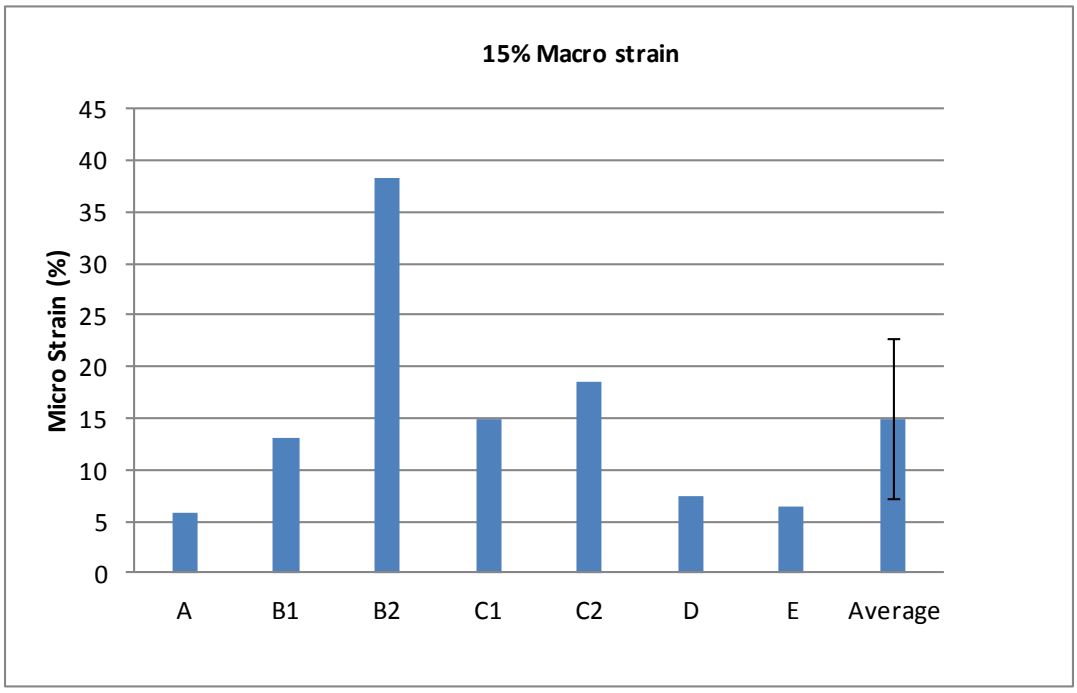

Figure 6.7: The results obtained indicate the strain percentage between the cells at 15% strain of the tissue.

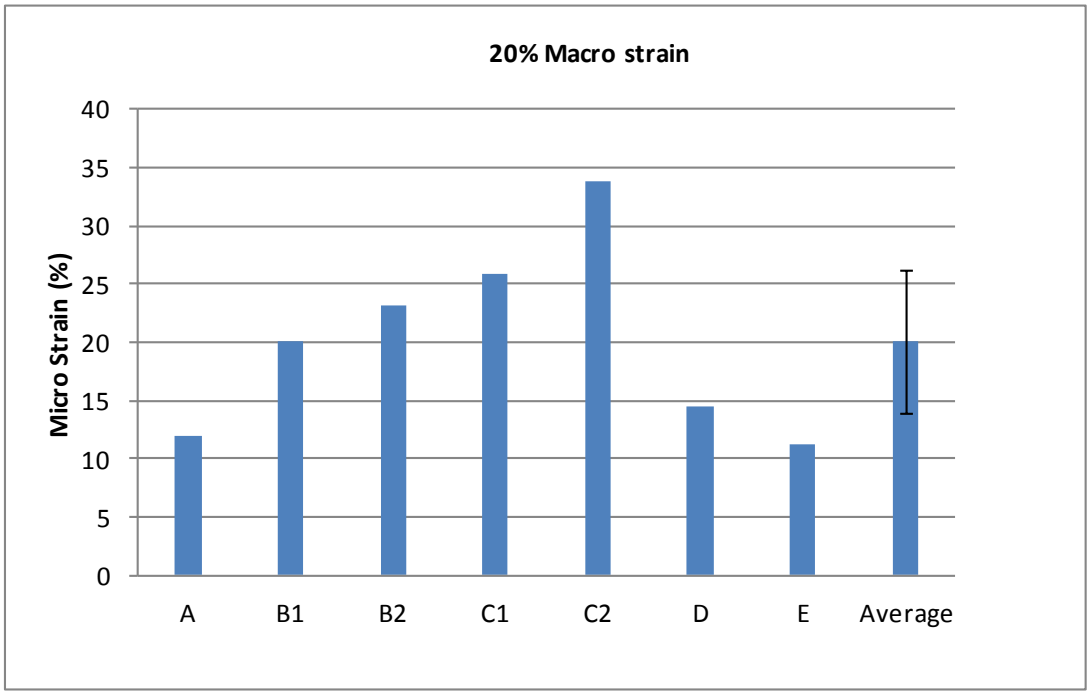

Figure 6.8: The results obtained indicate the strain percentage between the cells at 20% strain of the tissue.

6.3.2 Comparison between experimental and computational results

The experimental findings were then compared to the results obtained from the computational simulations that were previously described in Chapter 5. The averages for each run (Models 3, 4, and 5 and experimental) are demonstrated in Figure 6.9, while the actual values are listed in Table 6.2. As it can be seen from the graph, with just a few exceptions as in Model 5 at 20% of global strain, all the averages from the computational models lie within the error bar of the average obtained experimentally.

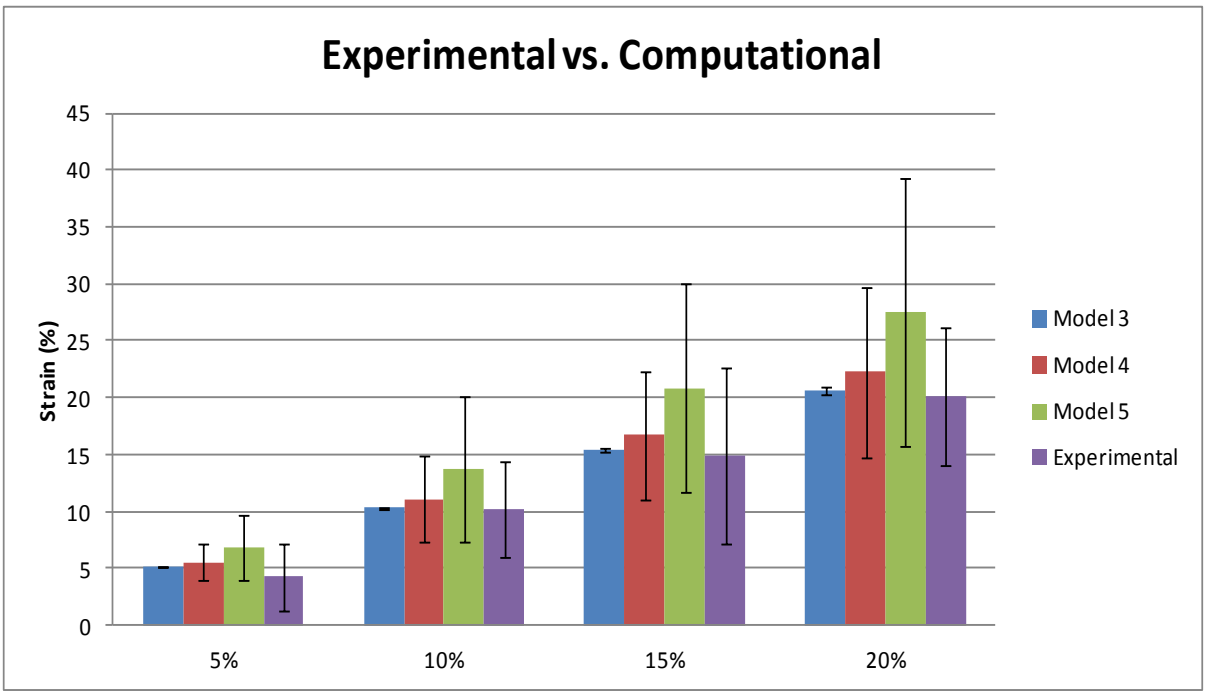

Figure 6.9: The results obtained indicate the strain percentage between the cells at 20% strain of the tissue

Macrostrain	5%	10%	15%	20%
Model 3	5.14	10.29	15.43	20.57
Model 4	5.56	11.09	16.69	22.22
Model 5	6.86	13.74	20.83	27.48
Experimental	4.23±2.9	10.17±4.2	14.9±7.7	20.1±6

Table 6.2: List of the actual averaged values obtained from computational models and experimental procedure.

6.4 Discussion

Five fresh femoral porcine arteries were stained for cell nuclei and strips of each tissue were stretched up to 20% of their initial length along circumferential direction, under the confocal microscope. The change in the distance between different pairs of cells was calculated during tissue stretching at different macro-strains (5%, 10%, 15% and 20%). The average value of the micro strain seems in a good agreement with the macro strain applied on the whole tissue, for all four cases. However, there seems to be a great variation between cell displacements along the tissue. The cells are supposed to be attached to a fibre, either elastin or collagen. Nevertheless, since elastin and collagen are two materials of different mechanical properties, they are expected to stretch differently. Additionally, the abundance, the orientation and the direction of the fibres play a significant role at this level of examination, and thus, the way they move apart from each other may vary, even within the same sample, as in the cases of B1 and B2, and C1 and C2. These findings prove the high inhomogeneicity of the vascular ECM.

Another factor that should be taken into account is the cell viability. All the tissue samples used were dissected from freshly slaughtered animals and during staining there were immerged in transport medium. Experiments for cell viability after similar process indicated a great viability percentage of the cells, however there well still a few dead ones. And since a dead cell may no longer be attached to any of the fibres and is free to float, it may move at a greater or a smaller distance than the remaining alive ones during macro stretching.

Additionally, this process carries another limitation in terms of the strain application. The tissue sample was inevitably subject to some stretching during mounting, which means that there was no truly zero-strain state at the beginning of the experiment. Moreover, the jaw of the rig was moving electrically. Despite the fact that it was proved accurate by performance tests, it could still carry a small error.

Furthermore, in some cases, despite the stretching, the distance between the cells gets smaller instead of larger (as in cases of A in Figure 6.7 and B2 in Figure 6.8). This is probably due to the complexity of the tissue mounting, and/or due to crimp effects.

Nevertheless, all the distances between randomly selected cells – which were chosen mostly according to their clear visibility in every stage of stretching – resulted in an average which was really close to the global strain. This is of great interest, because the samples were not derived from the same artery. On one hand, this may be a coincidence. However, the structure of the arterial wall is not very different to each other, since all the samples come from the same arteries of the same species. Theoretically, since it is difficult to study the strain distribution for an inhomogeneous material, the standard procedure is to divide it into smaller intervals and treat each one as homogeneous. Then their average should approach the globally applied strain. In the present study, the average in every strain condition (5%, 10%, 15% and 20%) was in a very good agreement with the global strain. This suggests that the sample size is good.

The great variation of micro-strain within the vascular wall is of great interest, but further investigation is needed for an extended discussion, which will include the staining of each component within the ECM. This is hard to be achieved, especially when dealing with fresh tissue, since fresh tissue means live cells, while the toxicity of the staining will probably kill the cells. Moreover, even if the cells survive the staining, it will probably be really difficult – if at all possible – to distinguish between the levels of the microscope focus. All this is beyond the scope of the present study, since this experimental procedure was carried out in order to examine whether the computational simulations can replicate the strain spread that was observed experimentally.

Comparison between computational and experimental findings indicated that the FEA results lie within the error bar of the average derived experimentally. However, the case of Model 3 seems very ideal, in terms that there is no such variation between the node distances. On the other hand, Model 5 provides much greater variation, not only compared to the other models, but also compared to the experimental findings. This is also the reason for the large error bars in all global strain scenarios (5%, 10%, 15% and 20%). There seems to be a good agreement though between the experimental and the Model 4 results. Despite the difference between their averages, there is a similar pattern in the variation between the point-distance, resulting in a similar error, since the error bars in the present case demonstrate the variation in the local strain. This suggests that Model 4 is the

closest approach to the *in vitro* study so far. Nevertheless, further investigation is needed, which this comparison was between a 2D computational model against a 3D tissue sample.

Furthermore, another point of interest between the computational and experimental findings lies on the initial distance between the points. The findings from the experimental procedure indicated that the variation between the results does not seem to be dependent on the initial distance between the cells. For example, the initial distance for B2 and C1 were similar (24.5μm and 20.25μm respectively), however the micro strain correspondence is very different in all four cases. Similarly for the distances between pairs A (107μm) and E (113.7μm). Additionally, the variation in micro-strain is also different even within the same tissue sample. The pattern in the distance for B1 and B2, as well as C1 and C2 also vary, despite that they belong to the same sample. For computational simulations, the strain variation between the points under examination was dependant on their initial distance. The greatest variation was seeing in the distance between point 3-5 and 5-7, whose initial distant was smaller. In contrast, the strain between the points 3-7 and 4-8, whose initial distance was greater, was closer to the average in all the models. This probably suggests that in FE analysis, smaller intervals should be examined, in order to obtain a better understanding on the strain variation, and eventually the stress.

Moreover, it should be noted that this investigation was based on uniaxial stretching of the tissue, while a biaxial case would be more realistic in order to estimate the way the macro strain is translated into the micro level within the arterial wall. In a biaxial case, theoretically, the micro-strain will be reduced. This reduction cannot be predicted at this stage, since the mechanical properties of the tissue are different along the axial and circumferential direction. However, as the overall loading will result not only to the dilation but also to the extension of the tissue, theoretically should decrease the strain in the circumferential direction. Additionally, as mentioned in Chapter 3, the restriction of the extension of the arteries during pressure test may have overestimated the tissue dilation, compared to the in situ condition. Similarly, the uniaxial stretching performed in this investigation has overestimated the local strains. That applies to the computational procedure as well as to the experimental one and will be included in some further investigation.

Therefore, a 3D model should be developed that will involve the correct mechanical properties of the tissue components and a 3D displacement, as in a realistic case. After validation of these computational simulations with a respective experimental procedure, the values of stress could be determined computationally and further used, in order to optimise the conditions in the vascular bioreactor.

Chapter 7. General Discussion and Conclusions

In spite of the great advances in the medical field, vascular pathologies remains the primary cause of fatality in western societies. Conventional treatments for such pathologies involve the replacement of the defected vascular tissue with either artificial conduits or natural vascular grafts of autologous, homologous and xenogenic origin. Such treatments carry several limitations, which are associated with the need for anticoagulation with and the low patency rate (for small sizes) of artificial grafts, the need for immunosuppression with and the limited supply of homologous tissue, the limited durability and lack of regeneration of the chemically-treated xenogenic tissue, and the sacrifice of a healthy conduit with the autologous tissue .

Tissue engineering of vascular conduits using natural scaffolds offers an attractive alternative for vascular reconstructions since they have the potential to repair, remodel and grow with the patient. However, an ideal tissue-engineered blood vessel has yet to be developed. In the case of *in vitro* tissue engineering, whereby a scaffold is seeded with cells *in vitro* and physically conditioned in a bioreactor designed to simulate the natural environment of the body, several parameters need to be determined and optimised in order to provide to the seeded cell an ideal environment for effectively migrating, proliferating, repopulating and, subsequently, regenerating the scaffold. One of these parameters includes the dynamic physical stimulus that the cells need to be exposed to in the bioreactor in order to regenerate the vascular tissue in a physiological manner.

Although researchers in the field agree on the type of macroscale physical stimulation (pulsatile flow and pressure) that needs to be simulated for vascular regeneration, the level of this physical stimulus still remains speculative, with suggestions ranging from foetal conditions, to normotensive adult conditions, to even pathological conditions. In addition, little is still know with regards to how the macroscale physical stimulus is translated to the microscale environment of the cells, especially when scaffolds with different histoarchitectures are employed. The main difficulty in dealing with these issues is that they are hard, and usually quite expensive, to be determined by experimental means, especially when scaffolds with

natural histoarchitectures are employed. An alternative method for such investigations is the computational approach.

The purpose of the present study was to develop computational models that simulated the natural histoarchitecture of the arterial wall with a view to investigating the behaviour of the native artery when exposed to physiological blood pressure. The main focus was to quantify the macroscale strain imposed to the vascular wall and to replicate its effect at the microscale environment of the extracellular matrix (ECM) protein fibres and cells. The reason that the present investigation was focused on the strain was due to the fact that only strain could be validated experimentally. Experimental validation, as well as mathematical verification, is crucial for computational simulations, since it is the only way to determine the accuracy of the numerical solutions. When a computational model has proved accurate enough, it can provide more parameters that are not always possible to be determined experimentally.

Although the current study was focused only on the natural arterial tissue and normal blood pressure conditions, with a view to quantifying the level of strain experienced by the cells under normotensive conditions, the developed computational models can also be employed to investigate macroscale-microscale strain translation under different blood pressure conditions (hypotensive, hypertensive). Such utilisation of the models can elucidate the effect of different pathological conditions on the strain experienced by the cells, and how this strain regulates cell function. In the field of tissue engineering, the developed models can be employed to study the effect of different scaffold architectures on the strain translation from the macroscale to the microscale, in order to optimise bioreactor operation (input conditions of pressure and flow) and, subsequently, *in vitro* cell mechanotransduction and tissue regeneration.

7.1 Investigation of the strain at the arterial wall at macro-level

In the context of the present study, Chapters 3 and 4 described the materials and methods used for the experimental and computational process, in order to determine the macroscale strain experienced by the arterial tissue. During the experimental process, fresh porcine femoral arteries were used and tested within 8

hours from in order to achieve an as-physiological-as-possible simulation of the natural tissue behaviour. The arteries were subject to dilation testing, during which the arteries were stepwise pressurised up to a static pressure of 120 mmHg and their dilation was measured at each pressure step. The results resorted were used to validate the numerical simulations of vascular dilation. The first limitation that this method carried was the small sample size. Additionally, during pressure test, the arteries were likely subject to creep, due to the time increments, and this may have resulted in an overestimated dilation. Moreover, the measurements for the initial and extended lengths were carried out manually from the images, and this process may also have resulted in an undetermined error.

The arteries were further assessed in terms of their geometrical (length, thickness and diameter) and mechanical (elastic Young's modulus) properties. The mechanical properties were determined after uniaxial tensile loading to failure. The uniaxial test is not considered as ideal, first because the arteries carry different mechanical properties at each direction, and also because their movement *in situ* does not take place in one direction. The recorded stress-strain behaviour of the arteries was used to determine their modulus during their elastin phase. The rationale for using the elastin phase modulus was the fact that under normal conditions tissues are loaded up to their transition phase, following a stress-strain behaviour close to their elastin phase stress-strain behaviour. Subsequently, the geometrical and mechanical properties of the arteries were used to construct the arterial mesh for the computational simulations.

Five models were run under different pressure conditions; one under static pressure and 3 under different pulsatile pressure waveforms. The models were validated for their accuracy both analytically and experimentally. The analytical solution for the axial and circumferential stress suggested reasonable accuracy of the numerical results. However, there was not a good agreement between the experimental and computational dilation. The reason for this was probably due to the mechanical properties that were used to describe the tissue material computationally. Physiologically, the artery dilates in three dimensions. However, the modulus that was used in the models was the one determined under uniaxial tensile testing along the circumferential direction. A more realistic simulation of the tissue should involve mechanical properties determined in a biaxial testing setting, in order

to take into account the axial direction as well. The utilisation of the circumferential direction modulus of the artery in the computational model increased the stiffness of the arterial model, which predicted smaller dilations compared to the experimental results.

Comparison with previous similar studies also indicated a large dilation for the experimental test and a lower for the computational simulations. This also justifies the overestimation in the arterial dilation from the pressure test, and also that further investigation is needed for the computational models. Further improvement on the computational models may involve more realistic mechanical properties and also different pressure conditions. Nevertheless, the models that were developed were simple, repeatable and mathematically verified, which allows further improvement.

7.2 Investigation of local strain at the arterial wall

The information on the dilation of the vascular wall obtained from the previous investigation was subsequently used in the microscale models of the arterial tissue. Chapter 5 described the procedure followed for the histological staining of the collagen and elastin fibres in the arterial wall. The micrographs obtained were used to develop the computational mesh that was employed for the FE analysis at the microscale level. A significant limitation of this process was that the tissue was stained in colour, while the software interface (Simpleware ScanIP) used provided a grey scale resolution of the images. Owing to this, it was hard to distinguish between the elastin and the collagen fibres. Additionally, there were several points where the collagen and elastin fibres overlapped and the user was called to decide which material will describe these points. Obviously any decision would affect the properties and eventually the whole behaviour of the mesh. This issue is not easy to overcome, and requires computing and advanced imaging expertise. Despite these limitations, a 2D mesh of the arterial wall along circumferential direction was created based on the tissue stained images and was imported into Abaqus for numerical analysis.

The FE mesh model of the arterial wall predicted a displacement of up to 20% of its initial length along the x-direction, which was representing the circumferential

direction. The modulus of the collagen and elastin used in the models were taken from literature sources. Ideally, the moduli that should be used in such as model for the collagen and elastin should be the ones corresponding to their initial linear region. However, this information is not yet available, and thus, the maximum modulus was used to define the materials in the initial models. More models were subsequently developed, with the modulus for the collagen reduced by one order of magnitude each time (from 3GPa, to 0.3GPa and 0.03GPa), as an attempt to approach more realistic conditions.

In order to assess the accuracy of the numerical models, an experimental procedure was followed, where fresh arterial tissue was stained for cell nuclei and was stretched under a confocal microscope with the aid of a specially designed rig. Strips of fresh porcine femoral arteries were mounted on the rig and were gradually stretched up to 20% of their initial length. Several pairs of cells were identified and followed until the end of stretching in a depth of 30-50μm, and images were captured at each strain step. The distance between the chosen cells was then calculated from the recorded images, providing information on how the fibres were stretching as a result of the strain applied at the macroscale. The results obtained from this process indicated great variation between the samples. However, their average was in good agreement with the applied macroscale strain of 5%, 10%, 15% and 20%. This also indicates that the variation between the local measurements could be found throughout a single sample and not only between different samples, since there was a single or couple of measurements for each one.

The experimental results were compared to the ones obtained from the FE analysis, and found to be in good agreement with the computational results of Model 4, where the collagen modulus was set at 0.3 GPa and the elastin modulus at 0.01 GPa. This did not necessarily mean that these were the correct values for the collagen and elastin modulus, but it was probably an indication that they differ by one order of magnitude. Nevertheless, even the correct values of the material properties were found and used, the results between experimental and computational methods could still be different, since the comparison is between a 2D computational model and a 3D tissue sample. Further studies need to be focused on investigating the strain in a 3D computational mesh, which could be achieved in ScanIP using a stack of tissue stained images.

In addition, and in order to improve the accuracy of the developed computational models, the mechanical properties of the arterial tissue obtained by biaxial tensile testing need to be used. This would simulate a more realistic situation of vascular dilation, in both experimental and computational procedures. Theoretically, in the case of biaxial macro-strain, the local variation will also take place in two directions, and thus, smaller cell displacement should be expected.

Further, the investigation should finally focus on the strain effect of the cells, in order to provide information on the stress that the cells experience, as well. However, the diameter of a smooth muscle cell varies between 2-10μm, while its length ranges from 50-400μm. The fibres bundles may vary between 10-100mm wide and can be tens of centimetres long. The difference in size between the fibres and the cells is probably a great challenge for their computational simulation and should be considered for further work.

Because of the novelty of the present investigation, there can be no comparison with previously reported studies. Even in the case of Screen et al. (2003) only tendon fascicles were examined, which comprise mostly of collagen fibres and thus, the strain variation cannot be similar to the arterial tissue, which carries highly inhomogeneous histoarchitecture. Additionally, no similar FEA studies have reported a realistic histoarchitecture of the arterial wall at this scale.

An improvement on the computational mesh and the mechanical properties of the ECM components, will also allow the study of strain variation in a more detail. That is by clearly distinguishing the fibres, the strain spread for each component can be determined computationally. This process is much more expensive – if at all possible – to be carried out experimentally.

7.3 Conclusions

- Hypothesis justified as it is possible to simulate the local strain variation in the arterial tissue as a response to the macro-strain, using computational simulations.

- The FSI models developed in this study are simple, repeatable and mathematically verified, which allows further improvement in terms of the tissue mechanical properties and more realistic boundary conditions.
- The FSI models were comparable with experimental findings and previously reported similar studies.
- The linear elastic material that was used for the arterial wall in FSI models resulted in similar findings for the cases of static and pulsatile pressure conditions. This means that static pressure can be used instead, which will save computational time.
- Further investigation on the FSI models should include biaxially determined mechanical properties of the arterial wall and more physiological pressure conditions.
- A novel approach for the investigation of the local strain variation in the middle layer of the arterial wall was delivered in the present study, both computationally and experimentally.
- The FEA models were subject to comparison against experimental findings. There is only a limited number of studies reporting on such comparisons on investigation at this level.
- Further investigation is needed on the improvement of the computational mesh, which requires computing and advanced images expertise.
- Further investigation on FEA models is also necessary. This should include the development of 3D models, appropriate mechanical properties for the ECM components, as well as biaxial strain conditions.

7.4 Future Work

The ultimate goal of the present investigation is to develop in silico platforms in order to extract information on the stress that the smooth muscle cells experience, with a view to optimise bioreactor conditioning for the development of tissue engineered blood vessels. Therefore, the presented work needs to be followed by a number of actions. As mentioned earlier, biaxial testing is necessary, in order to provide more realistic findings for both experimental and computational simulations. Additionally, the area of interest on the stress/strain should also be transferred to the

cells and not only the fibres of the extracellular matrix. This requires further development of experimental procedures and computational simulations, which remain a great challenge due to the size and location of the particular cells.

References

Adina , Theory and Modelling Guide, volume III: Adina CFD & FSI, Adina R&D Inc, 2006.

Aging Research, accessible at http://ageing-research.blogspot.com/ 2008_ 05_01_ archive.html, [last accessed at 30 January 2010].

Alden, K., Timmis, J., Andrews, P.S, Veiga-Fernandes, H. and Coles, M.C., Pairing experimentation and computational modeling to understand the role of tissue inducer cells in the development of lymph. Immunol. 3, 172, 2012.

Allen, R.A., Wu W., Yao M., Dutta D., Duan X., Bachman T.N., Champion H.C., Stolz D.B., Robertson A.M., Kim K., Isenberg J.S., Wang Y., Nerve regeneration and elastin formation within poly(glycerol sebacate)-based synthetic arterial grafts one-year post-implantation in a rat model. Biomaterials 35 (1) 165–173, 2014.

Alexopoulos, L.G., Williams, G.M., Upton, M.L., Setton, L.A. and Guilak, F., Osteoarthritic changes in the biphasic mechanical properties of the chondrocyte pericellular matrix in articular cartilage., J. Biomechanics, 38, 509-517, 2005.

Armentano, R.L., Levenson, J., Barra, J.G., Fischer, E.I., Breitbart, G.J., Pichel, R.H. and Simon, A., Assessment of elastin and collagen contribution to aortic elasticityin conscious dogs, American Journal of Physiology, 1991, 260, H1870-H1877.

Avolio, A.P., Multi-branched model of the human arterial system, Med. Biol. Eng. Comput. 18, 709-718, 1980.

Bader, H., The anatomy and physiology of the vascular wall, In: Handbook of Physiology, Section 2: Circulation, Volume II, (Ed. Hamilton, W.F.), Chapter 26, American Physiological Society, Washington D.C., 1963.

Badylak, S.F., Lantz, G.C., Coffey, A. and Geddes, L.A., Small intestinal submucosa as a large diameter vascular graft in the dog, Journal of surgical research, 1989, 47(1), 74-80.

Balar, S.D., Rogge, T.R. and Young, D.F, Computer simulation of blood flow in the human arm, J. Biomech., 22, 691-697, 1989.

Ballyk, P.D., Steinman, D.A. and Ethier, C.R., Simulation of non-Newtonian blood flow in an end-to-side anastomosis, Biorheology, 31, 565-86,1994.

Barra,J.G., Armentano, R.L., Levenson, J., Fischer, E.I., Pichel, R.H. and Simon, A, Assessment of smooth muscle contribution to descending thoracic aortic elastic mechanics in conscious dogs, Circulation Research, 1993, 73, 1040-50.

Bergan, J.J., Schmid-Schönbein, G.W., Smith, P.D., Nicolaides, A.N., Boisseau, M.R., Eklof, B., Chronic venous disease, N Engl J Med. 3;355(5):488-98, 2006.

Benrashid, E., McCoy, C.C., Youngwirth, L. M., Jina Kim, Manson, R. J., Otto, J. C., Lawson, J. H. Tissue engineered vascular grafts: Origins, development, and current strategies for clinical application, Methods, 99, 13-19, 2016.

Berglund, J.D. and Galis Z.S., Designer blood vessels and therapeutic revascularisation, British Journal of Parmacology, 140, 627-636, 2003.

Booth, C., Korossis, S.A., Wilcox, H.E., Watterson, K.G., Kearney, J.N., Fisher, J., Ingham, E., Tissue engineering of cardiac valve prostheses I: development and histological characterization of an acellular porcine scaffold, J Heart Valve Dis, 11(4), 457-62, 2002.

Borau, C., Kamm, R., Garcia-Aznar, J., Mechano-sensing and cell migration: a 3D model approach, Phys. Biol. 8, 6, 2011.

Bozkurt, O., Tissue Engineering of blood vessels, Biomaterials and Tissue Engineering research centre, Middle-East Technical University, Biotechnology Research Unit, http://www.biomed.metu.edu.tr/courses/ term-papers.htm, [last accessed at 7 September 2008].

Campbell, J.H, Efendy, J.L., and Campbell, G.R., Novel vascular graft grown within recipient's own peritoneal cavity, Circ. Res., 1999, 85, 1173-1178.

Cancer research UK, http://www.cancerhelp.org.uk/cancer_images/circul.gif , [last accessed at 7 September 2008].

Capillary Circulation, http://www.capillarycirculation.com, [last accessed at 29 January 2010].

Carew, T.E., Vaishnav, R.N. and Edwards, J.E., Compressibility of the arterial wall, Circulation Research, 1968, 23, 61-68.

Chandra, K.B., Vonesh, M.J., Roy, A., Greenfield, S., Kane, B., Greene, R. and McPherson, D.D., Computation of vascular flow dynamics from intravascular ultrasound images., Med. Eng. Phys., 18, 295-304, 1996.

Chen, J. and Lu, X.Y., Numerical investigation of the non-Newtonian pulsatile blood flow in a bifurcation model with a nin-planar branch, J Biomech., 39, 818-832, 2006.

Chen, W., Lou, J., Hsin, J., Schulten, K., Harvey, S.C., Zhu, C., Molecular Dynamics Simulations of Forced Unbending of Integrin αVβ3, PLoS Comput. Biol. 7, 2, 2011.

Chien, S., Mechanotransduction and endothelial cell homeostasis: the wisdom of the cell., Am J Physiol Heart Circ Physiol, 292, H1209-H1224, 2007.

Cho, Y.I. and Kensey, K.R., Effects of the non-Newtonian viscosity of blood on flows in a diseased arterial vessel: Part I: Steady flows, Biorheology, 28, 241-262, 1991.

Conklin, B.S., Richter, E.R., Kreutziger, K.L., Zhong, D.S. and Chen, C., Development and evaluation of a novel decellularised vascular xenograft, Medical Engineering & Physics, 2002, 24, 173-183.

Coosa Valley Technical College, http://www.cvtcollege.org/Ac_Programs/dms_vascular/studentmisty.html, [last accessed at 7 September 2008].

Dale, W.A. and Lewis, M.R., Further experiences with bovine arterial grafts, Surgery, 80(6):711-21, 1976.

Darby, C.R., Roy, D., Deardon, D. and Cornall, A., Depopulated bovine ureteric xenograft for complex haemodialysis vascular access, Eur J Vasc Endovasc Surg., 31, 2: 181-186, 2006.

Dardik, H., Miller, N., Dardik, A., Ibrahim, I., Sussman B, Berry, S.M., Wolodiger, F., Kahn, M., Dardik. I., A decade of experience with the glutaraldehyde-tanned human umbilical cord vein graft for revascularization of the lower limb. J Vasc Surg 7:336-46,1988.

Dardik, H., Wengerter, K., Qin, F., Pangilinan, A., Silvestri, F., Wolodiger, F., Kahn, M., Sussman, B., Ibrahim, I.M., Comparative decades of experience with glutaraldehyde-tanned human umbilical cord vein graft for lower limb revascularization: an analysis of 1275 cases. J Vasc Surg 35(1):64-71, 2002.

Edelma, E.R., Vascular Tissue Engineering: Designer Arteries, Journal of American Heart Association, Circular Research, 1999, 85, 1115-1117.

Fung, Y.C., Biomechanics: mechanical properties of living tissues, 2nd ed. Berlin: Springer; 1993.

Fung, Y.C., Biomechanics: Mechanical properties of living tissues, Second Edition, Springer, New York, 1993.

Giannoglou, G.D., Soulis, J.V., Farmakis, T.M., Farmakis, D.M. and Louridas, G.E., Haemodynamic factors and the important role of local low static pressure in coronary wall thickening, Int. J. Cardiol., 86, 27-40, 2002.

Gibson, C.M., Diaz, L., Kandarpa, K., Sacks, F.M., Pasternak, R.C., Sandor, T., Feldman, C. and Stone, P.H., Relation of vessel wall shear stress to atherosclerosis progression in human coronary arteries, Arterioscler. Thromb., 13, 310-315, 1993.

Gijsen, F.J., van de Vosse, F.N. and Jansse, J.D, The influence of the non-Newtonian properties of blood on the flow in large arteries: Steady flow in a carotid bifurcation model, J. Biomech., 32, 601-608, 1999.

Gosselin, C., Vorp, D.A, Warty, V., Severyn, D.A., Dick, E.K., Borovetz, H.S., and Greisler, H.P., ePTFE coating with fibrin glue, FGF-1, and heparin: effect on retention of seeed endothelial cells, J Surg. Res, 60, 327-332, 1996.

Greenwald, S.E, Ageing of the conduit arteries, J. Pathol. 211, 2: 157-172, 2007.

Guilak, F. and Mow, V.C., The mechanical environment of the chondrocyte: a biphasic finite element model of cell-matrix interactions in articular cartilage, J. Biomechanics, 33, 1663-1673, 2000.

Health Plan of New York, www.hipusa.com/.../heart_disease/index.html, [last accessed at 7 September 2008].

Herring M, Smith J, Dalsing M, Glover J, Compton R, Etchberger K, Zollinger T., Endothelial seeding of plytetrafluoroethylene femoral popliteal bypasses: the failure of low-density seeding to improve patency., J. Vasc. Surg., 20, 650-655, 1994.

Hilbert, D., An efficient Navier-Stokes solver and its application to fluid in elastic tubes, Colloquia Mathematica Societaris Janos Bolya, 50, 439-447, 1986.

Hillen, B, Hoogstraten, H.W. and Post, L., A mathematical model of the flow in the circle of Willis, J. Biomech, 19, 187-194, 1986.

Hron, J. and Madlik, M., Fluid-structure interaction with applications in biomechanics, Non-Linear Analysis: Real World Applications, 2007, 8, 1431-1458.

Hu, J.J., Lu, P.C, Lou C.W., Lee M.C., Lin J.H., Small-diameter vascular grafts composed of polyester/spandex fibers: Manufacturing techniques and property evaluations, Materials Letters, 171, 42-45, 2016.

Hughes, T.J.R., A study of the one-dimensional theory of arterial pulse propagation, PhD Thesis, University of California, Berkeley, 1974.

Humphrey, J.D., Cardiovascular Solid Mechanics: Cells, Tissues, and Organs, Springer, New York, 2002.

Humphrey, J.D., Vascular adaptation and mechanical homeostasis at tissue, cellular, andsub-cellular levels, Cell Biochem. Biophys. 50, 2: 53-78, 2008.

Ilegbusi, O.J., Hu, Z., Nesto, R., Waxman, S., Cyganski, D, Killian, J., Stone, P.H. and Feldman, C.L., Determination of blood flow and endothelial shear stress in human coronary artery *in vivo*, J. Invasive Cardiol., 11, 667-674, 1999.

Jafari, A., Mousavi, S.M. and Kolari, P., Numerical investigation of blood flow. Part I: In microvessel bifurcations, Communications in Nonlinear Science and Numerical Simulation, 13, 1615-1626, 2008.

Jin, S., Yang, Y., Oshinski, J., Tannenbaum, A., Gruden, J., Giddens, D., Flow patterns and wall shear stress distributions at atherosclerotic-prone sites in a human left coronary artery--an exploration using combined methods of CT and computational fluid dynamics., Conf Proc IEEE Eng Med Biol Soc., 5:3789-91, 2004.

Johnston, B.M., Johnston, P.R., Corney, S. and Kilpatrick, D., Non-Newtonian blood flow in human right coronary arteries: Steady state simulations, Journal of Biomechanics, 37, 709-720, 2004.

Johnston, B.M., Johnston, P.R., Corney, S. and Kilpatrick, D., Non-Newtonian blood flow in human right coronary arteries: Transient simulations, Journal of Biomechanics, 39, 1116-1128, 2006.

Julie R. Fuchs, M.D., Boris A. Nasseri, M.D. and Joseph P. Vacanti. 'Tissue engineering: A 21st Century Solution to Surgical Reconstruction' Ann Thorac Surg, 72, 577-591, 2001.

Kaiser,D.R., Billups, K., Mason, C., Wetterlings, R., Lundberg J.L. and Bank, A.J., Impaired Brachial Artery Endothelium-Dependent and -Independent Vasodilation in Men With Erectile Dysfunction and No Other Clinical Cardiovascular Disease., Journal of the American College of Cardiology, 43:2, 179-184, 2004.

Kawasaki, T., Sasayama, S., Yagi, S., Asakawa, T. and Hirai, T., Non-invasive assessment of the age related changed in stiffness of major branches of the human arteries, Cardiovascular Research, 21, 678-87, 1987.

Kim BS, Mooney DJ. Development of biocompatible synthetic extracellular matrices for tissue engineering. Trends Biotechnol, 16, 224-230, 1998.

Kim, Y.H., Kim, J.E., Ito Y., Shih, A.M., Brott, B. and Anayiotos, A., Heamodynamic analysis of a compliant femoral artery bifurcation model using a Fluid Structure Interaction Framework. Annals of Biomech Eng., 36: 11, 1753-63, 2008.

Klipp, E. and Liebermeister, W., Mathematical modelling of intracellular signalling pathways, BMC Neurosci., 7 (Suppl. (1)), S10, 2006.

Korossis ,S.A., Wilcox, H.E., Watterson, K.G., Kearney, J.N., Ingham, E., Fisher, J., In-vitro assessment of the functional performance of the decellularized intact porcine aortic root, J Heart Valve Dis, 14, 3: 408-21, 2005.

Korossis, S, Biomechanics & Hydrodynamics of decellularised aortic heart valves for tissue engineering, PhD thesis, University of Leeds, 2002.

Krams, R., Wentzel, J.J., Oomen, J.A., Vinke, R. Schuurbiers, J.C., de Feyter, P.J., Serruys, P.W. and Slager, C.J., Evaluatoin of endothelial shear stress and 3D geometry as factors determining the development of atherosclerosis and remodeling in human coronary arteries *in vivo*. Combining 3D reconstruction from angiography and IVUS (ANGUS) with computational fluid dynamics, Arterioscler., Thromb., Vasc. Biol., 17, 2061-2065, 1997.

Ladak, H.M., Milner, J.S. and Steinman, Rapid three-dimensional segmentation of the carotid bifurcation from serial MR images, J. Biomech. Eng., 122, 96-99, 2000.

Ladak, H.M., Thomas, J.B., Mitchell, J.R., Rutt, B.K. and Steinman, D.A., A semiautomatic technique for measurement of arterial wall from black blood MRI, Med. Phys., 28, 1098-1107, 2001.

Lanne, T., Stale, H., Bengtsson, H., Gnstafsson, D., Bergqvist, D., Sonesson, B., Lecerof, H., Dahl, P., Non-invasive measurement of diameter changes in the distal abdominal aorta in man, Ultrasound in Medicine and Biology, 18, 5: 451-457, 1992.

Langille, B.L. and Adamson, S.L. Relationship between blood flow direction and endothelial cell orientation at arterial branch sites in rabbits and mice. Circ Res, 48, 481 – 488, 1981.

Lantz, G.C., Badylak, S.F., Hiles, M.C., Coffey, A.C., Geddes, L.A., Kokkini, K., Sandusky, G.E. and Morff, R.J., Small intestinal submucosa as a vascular graft: a review, J Invest Surg, 6, 297-310, 1993.

Laurent, S., Tropeano, A.I. and Boutouyrie, P., Pulse pressure reduction and cardiovascular protection, J. Hypertens. Supp., 24, 3: S13-S18, 2006.

Lee, S.W and Steinman, D.A., On the relative importance of rheology for image-based CFD models of the carotid bifurcation, J Biomech. Eng., 129, 273-278, 2007.

Lei, M., Archie, J. and Kleinstreuer, C., Computational design of a bypasss graft that minimizes wall shear stress gradients in the region of the distal anastomosis, J. Vasc. Surg., 25, 637-646, 1997.

Leung, J.H., Wright, A.R., Cheshire, N., Crane, J., Thom, S.A., Hughes, A.D. and Xu, Y., Fluid structure interaction of patient specific abdominal aortic aneurysms: a comparison with solid stress models, BioMedical Engineering OnLine, 5, 33-47, 2006.

Levick, J.R., An introduction to cardiovascular physiology, Hodder Arnold, Fourth Edition, London, 2003.

Levick, J.R., An introduction to cardiovascular physiology, Hodder Arnold, Fifth Edition, London, 2010.

L'heureux, N., Paquet, S., Labbe, R., Germain, L. and Auger, F.A., A completely biological tissue-engineered human blood vessel, FASEB J, 12, 47-56, 1998.

Li, J.K.J., Dynamics of the vascular system, Series on Bioengineering & Biomedical Engineering – Vol I, World Scientific, Singapore, 2004.

Lillie, M.A and Gosline, J.M., Mechanical properties of elastin along the thoracic aorta in the pig, J Biomechanics, 40, 2214-2221, 2007.

Liepsch, D., An introduction to biofluid mechanics-basic models and Applications, J. Biomech., 35, 415-43, 2002.

Liu, Y., Lai, Y., Nagaraj, A., Kane, B., Hamilton, A., Greene, R., McPherson, D.D. and Chandra, K.B., Pulsatile flow simulation in arterial vascular segments using intravascular ultrasound images, Med. Eng. Phys., 23, 583-595, 2001.

Long, Q., Xu, X.Y., Bourne, M. and Griffith, T.M., Numerical study of blood flow in an anatomically realistic aorto-iliac bifurcation generated from MRI data, J. Magn. Reson. Imaging, 43, 565-576, 2000a.

Long, Q., Xu, X.Y., Ariff, B, Thom, S.A., Hughes, A.D and Stanton, A.V., Reconstruction of blood flow patterns in a human carotid bifurcation: A combined CFD and MRI study, J. Magn. Reson. Imaging, 11, 299-311, 2000b.

Long, Q., Xu, X.Y., Collins, M.W, Bourne, M. and Griffith, T.M., Magnetic resonance image processing and structured grid generation of a human abdominal bifurcation, Comput. Methods Programs Biomed., 56, 249-259, 1998a.

Long, Q., Xu, X.Y., Collins, M.W., Griffith, T.M. and Bourne, M., The combination of magnetic resonance angiography and computational fluid dynamics: A critical review, Crit. Rev. Biomed. Eng., 26, 227-274, 1998b.

Ls-Dyna® keyword users manual, version 971, VolumeI, 2007. Available at: http://lstc.com/pdf/ls-dyna_971_manual_k.pdf
[Last accessed May 2016].

Martini, F.H., Fundamentals of Anatomy and Physiology, Prentice Hall, Upper Saddle River, New Jersey, Third edition, 1989.

Matsuura, J.H., Black, K.S., Levitt, A.B., Rosenthal, D., Wellons, E.D., Fallon, M.T., Davenport, C.K., Goodman, C.L., Pagelsen, N.D. and Ollerenshaw, J.D. Cellular remodeling of depopulated bovine ureter used as an arteriovenous graft in the canine model, Journal of the American College of Surgeons, 198, 5: 778-83, 2004.

Maurits, N.M, Loots, G.E and Veldman, A.E.P., The influence of vessel wall elasticity and peripheral resistance on the carotid artery flow wave form: A CFD model compared to *in vivo* ultrasound measurements, J. Biomech., 40, 427-436, 2007.

MedImaginery, http://www.medimagery.com/atherosclerosis.html, [last accessed at 7 September 2008].

Megerman, J., Hasson, J.E., Warnock, D.F., L'Italien, G.J., Abbott, W.M. Noninvasive measurements of nonlinear arterial elasticity. Am. J. Physiol. Heart. Circ. Physiol. 250, H181-H188, 1986.

Morris, P.D, Narracott, A., Tengg-Kobligk, H., Silva Sotto, D.A., Hsiao, S., Lungu, A., Evans, P., Bressloff, N.B., Lawford, P.V., Hose, D.R., Gunn, J.P., Computational Fluid Dynamics modeling in cardiovascular medicine., Heart, 0:1-11, 2015.

Mozersky, D.J, Sumner, D.S, Hokanson, D.E. and Strandness D.E., Transeutaneous Measurement of the Elastic Properties of the Human Femoral Artery., Circulation, Volume XLVI, 948-955, 1972.

Nerem, R.M, Levesque, M.J. and Cornhill J.F., Vascular endothelial morphology as an indicator of the pattern of blood flow. J Biomech Eng, 103 172 – 176,1981.

Nichols, W.W. and O'Rourke, M.F., McDonald's blood flow in arteries: Theoretical, experimental and clinical principles, Fourth Edition, Arnold, London, 1998.

Niklason, L.E., Abbott, W.M., Gao, J., Klagges, B., Hirschi, K.K., Ulubayram, K., Conroy, N., Jones, R., Vasanawala, A., Sanzgiri, S., and Langer, R., Morphologic and mechanical characteristics of engineered bovine arteries, J. Vasc. Surg., 33, 628-638, 2001.

Niklason, L.E., Gao, J., Abbott, W.M., Hirschi, K.K., Marini, R., Langer, R., Functional arteries grown *in vitro*, Science, 284, 489-493, 1999.

Nørgaard, B.L., Leipsic, J., Gaur, S., Seneviratne, S., Ko, B.S., Ito, H., Jensen, J.M., Mauri, L., De Bruyne, B., Bezerra, H., Osawa, K., Marwan, M., Naber, C., Erglis, A., Park, S.J., Christiansen, E.H., Kaltoft, A., Lassen J.F., Bøtker, H.E., Achenbach, S., Diagnostic performance of noninvasive fractional flow reserve derived from coronary computed tomography angiography in suspected coronary artery disease: the NXT trial (Analysis of Coronary Blood Flow Using CT Angiography: Next Steps), J Am Coll Cardiol., 63 (12):1145-55, 2014.

Oberkampf, W.L. and Trucano T.G., Verification and Validation in Computational Fluid Dynamics, 2002 available at: http://ftp.demec.ufpr.br/CFD/bibliografia/erros_numericos/Verification%20and%20Validation%20in%20computational%20fluid%20dynamics.pdf
[Last accessed 3/12/2016]

O'Callaghan, S., Walsh, M. and McGloughlin, T., Numerical modeling of Newtonian and non-Newtonian representation of blood in a distal end-to-side vascular bypass graft anastomosis, Med. Eng. Phys., 28, 70-74, 2006.

Olivier, L.A. and Truskey, G.A., A numerical analysis of forces exerted by laminar flow on spreading cells in a parallel plate flow chamber assay, Biotechnil. Bioeng. 42, 963, 1993.

O'Rourke, M.F and Hashimoto, J., Mechanical factors in arterial aging: a clinical perpective, J. Am. Coll. Cardiol, 50, 1: 1-13, 2007.

Oscuii, H.N., Shadpour, M.T. and Ghalichi, F., Flow characteristics in elastic arteries using a fluid-structure interaction model, American Journal of Applied Sciences, 4, 8: 516-524, 2007.

Pappas, P.J., Hobson, R.W., Meyers, M.G., Jamil, Z., Lee, B.C., Silva, M.B., Goldberg, M.C., Padberg, F.T., Patency of infrainguinal polytetrafluoroethylene bypass grafts with distal interposition vein cuffs. Cardiovasc Surg. 6(1):19-26, 1998.

Pearson, A., Guo, R., Orsinelli, D., Binkley, P. and Pasierski, T., Transesophageal, echocardiographic assessment of the effects of age, gender, and hypertension on thoracic aortic wall size, thickness, and stiffness, American Heart Journal, 128, 344-51, 1994.

Perktold, K. and Rappitsch, G., Computer simulation of local blood flow and vessel mechanics in a compliant carotid artery bifurcation model, Journal of Biomechanics, 28, 845-856, 1995.

Perktold, K., Rappitsch, G., Hofer, M and Karner, G., Numerical simulation of mass transfer in a realistic carotid artery bifurcation model, Am. Soc. Mech. Eng. Bioeng. Div. Publ. BED 35, 85-86, 1997.

Perktold, K., Resch, M. and Florian, H., Pulsatile non-Newtonian flow characteristics in a three-dimensional human carodtid bifurcation model, ASME J. Biomech. Eng., 113, 464-475, 1991.

Perktold, K., Resch, M. and Peter, R.0., Three dimensional numerical analysis of pulsatile flow and wall shear stress in the carotid artery bifurcation. J. Biomechanics, 24, 409-420, 1991a.

Perktold, K., Resch, M. and Florian, H., Pulsatile non-Newtonian flow characteristics in a three-dimensional human carotid artery bifurcation model, Trans. ASME J. Biomech. Engng, 113, 4646475, 1991b.

Perktold, K., Tatzle, H. and Schima, H., Computer simulation of hemodynamic effects in distal vascular graft anastomoses, Am. Soc. Mech. Eng. Bioeng. Div. Publ. BED 26, 91-94,1993.

Peyton, S.R., Kalcioglu, Z.I., Cohen, J.C.,Runkle, A.P., Van Vliet, K.J., Lauffenburger, D.A., Griffith, L.G., Marrow-derived stem cell motility in 3D synthetic scaffold is governed by geometry along with adhesivity and stiffness, Biotechnol Bioeng.,108(5):1181-93, 2011.

Pietrabissa, R. and Inzoli, F., Computational analysis of the fluid dynamics of a Pulsatile flow in an elastic tube, In Bouisset, S., Metral, S. and Monod, H., editors, Proceedings of XIVth Congress, Paris, 4, 1040-1041, 1993.

Politis, A.K., Stavropoulos, G.P., Christolis, M.N., Panagopoulos, F.G., Vlachos, N.S., and Markatos, N.C., Numerical modeling of simulated blood flow in idealized composite arterial coronary grafts: Steady state simulations, J. Biomech., 40, 1125-1136, 2007.

Politis, A.K., Stavropoulos, G.P., Christolis, M.N., Panagopoulos, F.G., Vlachos, N.S., and Markatos, N.C., Numerical modeling of simulated blood flow in idealized composite arterial coronary grafts: Transient flow, J. Biomech., 41, 25-39, 2008.

Prendergast, R.J, Lally, C., Daly, S., Reid, A.J., Lee, T.C., Quinn, D. and Dolan, F., Analysis of prolapsed in cardiovascular stents: a constitutive equation for vascular tissue and finite element modeling., J. Biomech. Eng., 125: 5, 692-699, 2003.

Raines, J.K., Jaffrin, M.Y. and Shapiro, A.H., A computer simulation of arterial dynamics in the human leg, J. Biomech., 7, 77-91, 1974.

Ratcliffe, A., Tissue Engineering of vascular grafts, Matrix Biology 19, 353-357, 2000.

Reuderink, P.J.R., Analysis of the flow in a 3D distensible model of the carodit artery bifurcation, PhD thesis, Eindhoven University of Technology, 1991.

Rhodin, J.A.G., Architecture of the vessel wall, In: Handbook of Physiology, Section 2: The Cardiovascular System Volume II: Vascular smooth muscle, (Eds. Bohr, D.F., Somlyo, A.P. and Sparks, H.V. Jr.), Chapter 1, Americal Physiological Society, 1980.

Roy, A.S., Back, L.H., Banerjee, R.K., Evaluation of Compliance of Arterial Vessel Using Coupled Fluid Structure Interaction Analysis, MCB, 5, 4, 229-245, 2008.

Rutten, M.C.M., Fluid solid interaction in large arteries, PhD thesis, Eindhoven Technical University, 1998.

Sasaki, N. and Odajimat,S, Stress-Strain curve and young's modulus of a collagen molecule as determined by the X-Ray diffraction technique, .J. Btomechics, Vol. 29, No. 5, pp. 655-658, 1996

Schmidt, S.P., Hunter, T.J., Sharp, W.V., Malindzak, G.S., Evancho,M.M.,. Endothelial cell seeded four millimeter Dacron vascular grafts. J. Vas. Surg. 1, 434-441, 1984.

Schneider K.H., Aigner P., Holnthoner W., Monforte X., Nürnberger S., Rünzler D., Redl H., Teuschl, A.H., Decellularized human placenta chorion matrix as a favorable source of small-diameter vascular grafts, Acta Biomaterialia 29, 125–134, 2016.

Schwarz, U.S. and Bischofs, B., Physical determinants of cell organization in soft media, Medical Engineering and Physics, 27, 763-772, 2005.

Scotti, C.M., Shkolnik, A.D., Muluk, S.C. and Finol, E.A., Fluid-structure ineraction in abdominal aortic aneurysms: effects of asymmetry and wall thickness, BioMedical Engineering online, 4, 64-85, 2005.

Scotti, C.M and Ender A. Finol, E.A., Compliant biomechanics of abdominal aortic aneurysms: A fluid–structure interaction study. Computers and Structures 85, 1097–1113, 2007.

Screen, H R C , D A Lee, D L Bader and J C Shelton, Development of a technique to determine strains in tendons using the cell nuclei. Biorheology, 40, 361-368, 2003.

Screen, H R C , D A Lee, D L Bader and J C Shelton, An investigation into the e € ects of the hierarchical structure of tendon fascicles on micromechanical properties Proc. Instn Mech. EngrsVol. 218Part H: J. Engineering in Medicine, 2004.

Screen, H.R.C., Shelton, J.C., Chhaya, V.H., Kayser, M.V, Bader, D.L. and Lee, D.A, The Influence of Noncollagenous Matrix Components on the Micromechanical Environment of Tendon Fascicles, Annals of Biomedical Engineering, Vol. 33, No. 8, 1090–1099, 2005.

Serruys, P.W., Kutryk, M.J., Ong, A.T. Coronary-artery stents. N Engl J Med, 2;354(5):483-95, 2006.

Siauw, W.L., Ng, E.Y, and Mazumdar, J., Unsteady stenosis flow prediction: A comparative study of non-Newtonian models with operator spitting scheme, Med. Eng. Phys., 22, 265-277, 2000.

Sonesson, B., Hansen, F., Stale, H. and Lanne, T., Compliance and diameter in the human abdominal aorta - the influence of age and sex, European Journal of Vascular Surgery, 7, 690-7, 1993.

Soulis, J.V., Giannoglou, G.D., Chatzizisis, Y.S., Seralidou, K.V., Parcharidis, G.E. and Louridas, G.E., Non-Newtonian models for molecular viscosity and wall shear stress in a 3D reconstructed human left coronary artery, Medical Engineering and Physics, 30, 9-19, 2008.

Spark, J.I., Yeluri, S., Derham, C., Wong Y.T. and Leitch, D., Incomplete cellular depopulation may explain the high failure rate of bovine ureteric grafts, Br J Surg., 2008, [Epub ahead of print].

Steele, B.N., Wan, J., Ku, J.P., Hughes, T.J.R. and Taylor, C.A., *In vivo* validation of a one-dimensional finite element method for simulation-based medical planning for cardiovascular bypass surger., IEEE Trans. Biomed. Eng., 50, 6: 649-656, 2003.

Stefanadis, C., Stratos, C., Boudoulas, H., Kourkoulis, C. and Toutouzas, P., Distensibility of the ascending aorta: comparison of invasive and non-invasive techniques in healthy men and in men with coronary artery disease, European Heart Journal, 11, 990-6, 1990.

Steinman, A. and Ethier, C.R., The effect of wall distensibility on flow in a two-dimensional end-to-side anastomosis, Journal of Biomechanical Engineering, 116, 294-301, 1994.

Steinman, D.A., Vinh, B., Ethier, C.R., Ojha, M., Cobbold, R.S. and Johnston, K.W., A numerical simulation of flow in a two-dimensional end-to-end anastomosis model, J. Biomech. 115, 112-118, 1993.

Stone, G.W., Lansky, A.J., Pocock, S.J., Gersh, B.J., Dangas, G., Witzenbichler, B., Guagliumi, G., Peruga, J.Z., Brodie, B.R., Dudek, D., Möckel, M., Ochala, A., Kellock, A., Parise, H., and Mehran, R. Paclitaxel-Eluting Stents versus Bare-Metal Stents in Acute Myocardial Infarction, N Engl J Med 360:1946-1959, 2009.

Sumpio, B.E, Riley, J.T. and Dardik, A., Cells in focus: endothelial cell, The International J Biochemistry & Cell Biology, 34, 1508-1512, 2002.

Tai NR, Salacinski HJ, Edwards A, Hamilton G, Seifalian AM. Compliance properties of conduits used in vascular reconstruction. Br J Surg, 87, 1516-1524, 2000.

Tasciyan, T.A., Banerjee, R., Cho, Y.I. and Kim, R., Two-dimensional pulsatile hemodynamic analysis in the magnetic resonance angiography interpretation of a stenosed carotid arterial bifurcation, Med. Phys, 20, 1059-1070, 1993.

Taylor, C.A. and Draney, M.T., Experimental and computational methods in cardiovascular fluid mechanics, Annu. Rev. Fluid Mech., 36, 197-231, 2004.

Taylor, C.A. and Humphrey, J.D., Open problems in computational vascular biomechanics: Hemodynamic and arterial wall mechanics, Comput. Methods Appl. Mech. Engrg., 2009.

Teebken, O.E., Bader, A., Steinhoff, G. and Haverich, A., Tissue Engineering of Vascular Grafts: human cell seeding of decellularised porcine matrix, Eur. J. Endovascular Surgery, 19, 381-186, 2000.

Teebken, O.E., Puschmann, C., Aper, T., Haverich, A., Mertsching, H. Tissue-engineered bioprosthetic venous valve: a long-term study in sheep. Eur J Vasc Endovasc Surg. Apr 25(4):305-12, 2003.

Thienel, U., Loike, J. and Yellin, M.J., CD154 (CD40L) induces human endothelial cell chemokine production and migration of leukocyte substs, Cell Immunol. 198, 87-95, 2000.

Tiwari A, Salacinski H, Seifalian AM, Hamilton G. New prostheses for use in bypass grafts with special emphasis on polyurethanes. Cardiovasc Surg, 10, 191-197, 2002.

Tseders, E.E. and Purinya, B.A., The mechanical properties of human blood vessels relative to their location, translated from Mekhanika Polimerov, 2, 320-325, 1975.

Tu, C. and Deville, M., Pulsatile flow of non-Newtonian fluids through arterial stenoses, J. Biomech., 29, 899-908, 1996.
UK transplant, available at http://uktransplant.org.uk/ukt/default.jsp, accessed at August 1, 2008.

Umpleby, H.C., Fermor, B., Symes, M.O., Williamson, R.C. Viability of exfoliated colorectal carcinoma cells. Br J Surg. 71(9):659-63, 1984.

Valencia, A. and Villanueva, M., Unsteady flow and mass transfer in models of stenotic arteries considering fluid-structure interaction, International Communications in Heat and Mass Transfer, 2006, 33, 966-975, 2006.

Valencia, A., Zarate, A., Galvesz, M. and Badilla, L., Non-Newtonian blood flow dynamics in a right internal carotid artery with a saccular aneurysm, Int. J. Numer. Methods Fluids, 50, 751-764, 2006.

Walburn, F.J. and Schneck, D.J., A constitutive equation for whole human blood, Biorheology, 13, 3: 201-10, 1976.

Wang, K.C., Dutton, R.W. and Taylor, C.A., Improving geometric model construction for blood flow modeling, IEEE Eng. Med. Biol. Mag., 18, 33-39, 1999.
Weinberg, C.B and Bell, E., A blood vessel model constructed from collagen and cultured vascular cells, Science, 231, 397-400, 1986.

Womersley, J.R., Oscillatory motion of a viscous liquid in a thin-walled elastic tube. I: The linear approximation for long waves, Philos. Mag., 7, 199-221, 1955.

Womersley, J.R., Oscillatory flow in arteries: the constrained elastic tube as a model of arterial flow and pulse transmission, Phys. Med. Biol., 2, 178-187, 1957.

Wooton, D.M. and Ku, D.N., Fluid mechanics of vasacular syst4ems, diseases, and thrombosis, Annu. Rev. Biomed. Engrg., 1, 299-329, 1999.

Wu, W., Allen R.A., Wang Y., Fast degrading elastomer enables rapid remodeling of a cell-free synthetic graft into a neo-artery, Nat. Med. 18 (7) 1148–1153, 2012.

Yow, K.-H., Ingram, J., Korossis, S.A., Ingham, E. and Homer-Vanniasinkam, S., Tissue Engineering of vascular conduits, British Journal of Surgery, 93, 652-661, 2006.

Yucel, D., 'Tissue Engineering of blood vessels', Biomaterials and Tissue Engineering research centre, Middle-East Technical University, Biotechnology Research Unit, http://www.biomed.metu.edu.tr/courses/ term-papers.htm, [last accessed at 7 September 2008].

Zaman, M.H., Trapani, L.M., Sieminski, A.L., Mackellar, D., Gong H, Kamm, R.D., Wells, A., Lauffenburger, D.A., Matsudaira, P., Migration of tumor cells in 3D matrices is governed by matrix stiffness along with cell-matrix adhesion and proteolysis, Proc Natl Acad Sci U S A, 103 (29):10889-94, 2006.

Zarins, C.K., Giddens, D.P., Bharadvaj, B.K., Sottiurai, V.S, Mabon, R.F., and Glagov, S., Carotid bifurcation atherosclerosis. Quantitative correlation of plaque localisation with flow velocity profiles and wall shear stress, Circ. Res. 53, 4: 502-514, 1983.

Zhao, S.Z., Xu, X.Y. Hughes, A.D., Thom, S.A., Stanton, A.V., Ariff, B. and Long, Q, Blood flow and vessel mechanics in a physiologically realistic model of a human carotid arterial bifurcation, J. Biomech., 33, 975-984, 2000.

Appendices

Appendix I.

Python script used to identify the nodes on the microscale model.

```
import odbAccess
from abaqusConstants import INTEGRATION_POINT
from abaqusConstants import NODAL


odbPath = ‘
instanceName = '
sectionCategoryNames = ['shell general < SM_COLLAGEN > < elset = ASSEMBLY_PART-1-1_SH_COLLAGEN_WITH_ZMIN >', 'shell general < SM_ELASTIN > < elset = ASSEMBLY_PART-1-1_SH_ELASTIN_WITH_ZMIN >']
stepName = 'Step-1'

# Define points of interest (POI) origin and specimen dimensions...

# The values of specimenX and specimenY set the X and Y dimensions of your model.
specimenX = 646.0
specimenY = 484.0

# The values of originX and originY are the X and Y coordinates of the point from which the code will take measurements.
originX = 40.0
originY = 242.0

# The value of xAxisSpacing sets the distance between each POI in the X direction.
xAxisSpacing = 5.6
yAxisSpacing = 83.8


# ----------------------------------------------------------------------------------------------------
# No user seviceable parts inside!



print 'Opening odb file...'
myOdb = session.openOdb(odbPath)
session.viewports['Viewport: 1'].setValues(displayedObject=session.odbs[odbPath])
nodes = myOdb.rootAssembly.instances[instanceName].nodes
elements = myOdb.rootAssembly.instances[instanceName].elements

poiList = []
```

```
# Build list of POI X and Y coordinates...

print 'Building a list of point of interest (POI) X and Y coordinates...'
poiList.append((originX, originY))

for a in range(1, 6):
    poiX = originX + ((specimenX / xAxisSpacing) * a)
    poiY1 = originY + (specimenY / yAxisSpacing)
    poiY2 = originY - (specimenY / yAxisSpacing)
    poiList.append((poiX, poiY1))
    poiList.append((poiX, poiY2))

# Find nodes (in stipulated material) nearest to POI and build node label list...

print 'Calculating nodal distances to POIs (for nodes within the chosen material)...'
distances = []

for currentElement in elements:
    for currentSecCatName in sectionCategoryNames:
        if currentElement.sectionCategory.name == currentSecCatName:
            for currentConnectivity in currentElement.connectivity:
                nodeCoords = nodes[currentConnectivity - 1].coordinates
                tempTable = []
                tempTable.append(currentConnectivity)
                for i in poiList:
                    tempXDist = abs(nodeCoords[0] - i[0])
                    tempYDist = abs(nodeCoords[1] - i[1])
                    tempResultantDist = ((tempXDist**2)+(tempYDist**2))**0.5
                    tempTable.append(tempResultantDist)
                distances.append(tempTable)

# Get node label for POIs...
# First, find minimum values from each set of distances...
print 'Identifying nodes that lie closest to POIs...'

poi0Min = min(b for (a,b,c,d,e,f,g,h,i,j,k,l) in distances)
poi1Min = min(c for (a,b,c,d,e,f,g,h,i,j,k,l) in distances)
poi2Min = min(d for (a,b,c,d,e,f,g,h,i,j,k,l) in distances)
poi3Min = min(e for (a,b,c,d,e,f,g,h,i,j,k,l) in distances)
poi4Min = min(f for (a,b,c,d,e,f,g,h,i,j,k,l) in distances)
poi5Min = min(g for (a,b,c,d,e,f,g,h,i,j,k,l) in distances)
poi6Min = min(h for (a,b,c,d,e,f,g,h,i,j,k,l) in distances)
poi7Min = min(i for (a,b,c,d,e,f,g,h,i,j,k,l) in distances)
poi8Min = min(j for (a,b,c,d,e,f,g,h,i,j,k,l) in distances)
poi9Min = min(k for (a,b,c,d,e,f,g,h,i,j,k,l) in distances)
poi10Min = min(l for (a,b,c,d,e,f,g,h,i,j,k,l) in distances)

poiLabels = [0, 0, 0, 0, 0, 0, 0, 0, 0, 0, 0]
```

```
# Then, find the node labels that correspond to these minima...

for j, q in enumerate(distances):
    if q[1] == poi0Min:
      poiLabels[0] = q[0]
    if q[2] == poi1Min:
      poiLabels[1] = q[0]
    if q[3] == poi2Min:
      poiLabels[2] = q[0]
    if q[4] == poi3Min:
      poiLabels[3] = q[0]
    if q[5] == poi4Min:
      poiLabels[4] = q[0]
    if q[6] == poi5Min:
      poiLabels[5] = q[0]
    if q[7] == poi6Min:
      poiLabels[6] = q[0]
    if q[8] == poi7Min:
      poiLabels[7] = q[0]
    if q[9] == poi8Min:
      poiLabels[8] = q[0]
    if q[10] == poi9Min:
      poiLabels[9] = q[0]
    if q[11] == poi10Min:
      poiLabels[10] = q[0]

print 'Highlighting nodal POIs in the viewport...'
for a in poiLabels:
   highlight(nodes[a-1])


# Now, get start coordinates for each POI...

print 'Finding starting coordinates for each POI...'
initialXCoords = []
initialYCoords = []

for currentPOI in poiLabels:
   initialXCoords.append(nodes[currentPOI-1].coordinates[0])
   initialYCoords.append(nodes[currentPOI-1].coordinates[1])

# Get the nodal displacements at the end of the simulation...

allDispEnd = myOdb.steps[stepName].frames[-1].fieldOutputs['U']

# Now, get the coordinates of each POI at the end of the simulation...
print 'Finding coordinates of each POI at the end of the simulation...'
endXCoords = []
endYCoords = []
```

```
for i, currentPOI in enumerate(poiLabels):
    tempEndXCoord = initialXCoords[i] + allDispEnd.values[currentPOI-1].data[0]
    tempEndYCoord = initialYCoords[i] + allDispEnd.values[currentPOI-1].data[1]
    endXCoords.append(tempEndXCoord)
    endYCoords.append(tempEndYCoord)

# Calculate distances between the origin and each POI at the start and end of the
simulation...
print 'Calculating distances between the origin and each POI at the start and end of
the simulation...'
distancesStart = []
distancesStartX = []
distancesStartY = []
distancesEnd = []
distancesEndX = []
distancesEndY = []

for j, currentPOI in enumerate(poiLabels):
    tempXStartDistance = abs(initialXCoords[j] - originX)
    tempYStartDistance = abs(initialYCoords[j] - originY)
    tempStartDistance = ((tempXStartDistance**2)+(tempYStartDistance**2))**0.5
    distancesStart.append(tempStartDistance)
    distancesStartX.append(tempXStartDistance)
    distancesStartY.append(tempYStartDistance)
    tempXEndDistance = abs(endXCoords[j] - endXCoords[0])
    tempYEndDistance = abs(endYCoords[j] - endYCoords[0])
    tempEndDistance = ((tempXEndDistance**2)+(tempYEndDistance**2))**0.5
    distancesEnd.append(tempEndDistance)
    distancesEndX.append(tempXEndDistance)
    distancesEndY.append(tempYEndDistance)

print ' '
print  '-----------------------------------------------------------------------------------------------------
------------'
print 'At the start, the distances between the origin and points...'
print '0, 1, 2, 3, 4, 5, 6, 7, 8, 9, 10'
print '...are:'
print distancesStartX
print '...in the X direction and:'
print distancesStartY
print '...in the Y direction. The resultant distances are:'
print distancesStart
print ' '
print 'At the end, the distances between the origin and points...'
print '0, 1, 2, 3, 4, 5, 6, 7, 8, 9, 10'
print '...are:'
print distancesEndX
print '...in the X direction and:'
print distancesEndY
```

```
print '...in the Y direction. The resultant distances are:'
print distancesEnd
print ' '
print 'Where point 0 is the origin in both cases.'
print  '-------------------------------------------------------------------------------------------------------------
------------
```